FRACBOT: DESIGN OF WIRELESS UNDERGROUND SENSOR NETWORKS FOR MAPPING HYDRAULIC FRACTURES AND DETERMINING RESERVOIR PARAMETERS IN UNCONVENTIONAL SYSTEMS

A Thesis
Presented to
The Academic Faculty

by

Abdallah Awadh Alshehri

In Partial Fulfillment
of the Requirements for the Degree
Doctor of Philosophy in the
School of Electrical and Computer Engineering

Georgia Institute of Technology
May 2018

Copyright © 2018 by Abdallah Awadh Alshehri

FRACBOT: DESIGN OF WIRELESS UNDERGROUND SENSOR NETWORKS FOR MAPPING HYDRAULIC FRACTURES AND DETERMINING RESERVOIR PARAMETERS IN UNCONVENTIONAL SYSTEMS

Approved by:

Professor Ian F. Akyildiz, Advisor
School of Electrical and Computer Engineering
Georgia Institute of Technology

Professor Raghupathy Sivakumar
School of Electrical and Computer Engineering
Georgia Institute of Technology

Professor Gee-Kung Chang
School of Electrical and Computer Engineering
Georgia Institute of Technology

Professor Mehmet Can Vuran
Department of Computer Science and Engineering
University of Nebraska-Lincoln

Professor Geoffrey Li
School of Electrical and Computer Engineering
Georgia Institute of Technology

Date Approved: 06 April 2018

To my parents: Awadh and Norah,

They taught me discipline, hard work and sense of purpose, without which my studies would not have been accomplished.

To my family: Huda, Rseel and Jana,

for their endless love, support, and encouragement.

ACKNOWLEDGEMENTS

First and foremost, I would like to express my deepest gratitude to my advisor, Professor Ian F. Akyildiz for his encouragement, guidance, valuable advice and endless support throughout my Ph.D. journey. Without his encouragement, this work would not have been possible. Working with him has been a true privilege. He has been an enthusiastic advisor with a genuine concern for my well-being. He stimulated me to perform to the best of my ability and provided me with opportunities and exposure that I would never have had if I had not joined him. I have learned from him not only technically, but on a personal level. For that, I am extremely grateful.

I would like to thank my thesis committee, Professors Gee-Kung Chang, Raghupathy Sivakumar, Geoffrey Y. Li, and Mehmet Can Vuran for reading my thesis and offering their valuable comments on my research.

I thank all former and current members of the Broadband and Wireless Networking Laboratory for sharing this learning environment and experience. Without their help, my stay here would not have been nearly as enjoyable and easy as it was. I am especially thankful to Ozan Bicen, Ravikumar Balakrishnan, Elias Chavarria, David Gutierrez Estevez, Bige D. Unluturk, Chong Han, Ahyoung Lee, Youssef Chahibi, Shih-Chun Lin, Shuai Nie, Manoj Chandrasekaran and Ahan Kak for their friendship and support.

A special thanks goes to Dr. Carlos Martins and Shih-Chun Lin for their great discussions and professional collaboration. I enjoyed a large number of discussions with Dr. Carlos Martins on research and other general topics that enriched me in many ways.

I also gratefully acknowledge EXPEC ARC/Saudi Aramco (my employer) for

granting me a scholarship to pursue my doctoral degree. Without its generous support, this work would not have been possible.

Above all, I am forever genuinely thankful to my parents for their love and selflessness, for instilling in me the belief that anything is possible, and for working intensely during their entire life to provide my siblings and me everything without asking for anything in return.

Finally, I would like to express my sincerest gratitude to my family (Huda, Rseel, and Jana) who have provided consistent support and walked this long journey with me. I thank them for sharing both the joys and burdens of this journey as well as extending their unconditional love and support.

TABLE OF CONTENTS

DEDICATION . . . . . **iii**

ACKNOWLEDGEMENTS . . . . . **iv**

LIST OF TABLES . . . . . **xi**

LIST OF FIGURES . . . . . **xii**

SUMMARY . . . . . **xvi**

I INTRODUCTION **1**

1.1 Hydraulic Fractures 4

1.2 Wireless Underground Sensor Networks (WUSNs) 5

1.3 MI-Based Underground Communications 6

1.4 Research Objectives 7

1.4.1 MI-Based Environment-Aware Cross-layer Communication Protocol Design for WUSN in Hydraulic Fractures and Oil Reservoirs 8

1.4.2 MI-Based Localization for WUSN in Hydraulic Fractures and Oil Reservoirs 8

1.4.3 Optimal Energy Planning for Self-Contained WUSN in Hydraulic Fractures and Oil Reservoirs 9

1.4.4 MI-based FracBot Node Design for Monitoring Hydraulic Fractures and Oil Reservoirs 9

1.4.5 FracBot Testbed: Performance Evaluation 10

1.5 Organization of the Thesis 10

II MI-BASED ENVIRONMENT-AWARE CROSS-LAYER COMMUNICATION PROTOCOL DESIGN FOR WUSN IN HYDRAULIC FRACTURES AND OIL RESERVOIRS **11**

2.1 Motivation 11

2.2 Related Work 13

2.3 System Model 16

2.4 The Effects of Environment-Dependent Parameters on the MI-based Communication in the Oil Reservoir Environment 18
2.4.1 MI Channel Model 18
2.4.2 Modulation and FEC 20
2.4.3 MAC Protocol and Geographical Routing Algorithm 22
2.5 Environment-Aware Three-layer Protocol Stack 24
2.6 Environment-Aware Cross-layer Optimization Framework 25
2.7 Distributed Environment-Aware Protocol (DEAP) Design 29
2.8 Performance Evaluation 31
2.8.1 Link Transmissions 32
2.8.2 End-to-End Data Flow 35
2.9 Highlights 37
III MI-BASED LOCALIZATION FOR WUSN IN HYDRAULIC FRACTURES AND OIL RESERVOIRS 39
3.1 Motivation 39
3.2 Related Work 41
3.3 System Model 43
3.4 MI-Based Localization Framework 45
3.4.1 MI-Channel Model and Node-to-Node Distance Measurement 45
3.4.2 RMFS Measurements for Designing Localization in Underground Oil Reservoirs 46
3.4.3 Underground Localization: Error Function and SDP 47
3.5 Fast Initial Positioning from the Alternating Direction Augmented Lagrangian Method (ADM) 48
3.5.1 Underground Localization SDP Problem 49
3.5.2 Fast Initial Positioning Through ADM for Underground Localization 51
3.6 Fine-Grained Positioning from the Conjugate Gradient Algorithm (CGA) 53
3.6.1 Steepest Descent (SD) Method 54
3.6.2 CGA with Conjugate Direction (CD) 55

3.7 Evaluation of Performance in Oil Reservoirs . . . 57
3.7.1 2D Localization in the Oil Reservoir Fracture . . . 58
3.7.2 Impact of the Underground Environment . . . 63
3.8 Highlights . . . 64

IV OPTIMAL ENERGY PLANNING FOR SELF-CONTAINED WUSN IN HYDRAULIC FRACTURES AND OIL RESERVOIRS . . . 66

4.1 Motivation . . . 66
4.2 Related Work . . . 67
4.3 System Model . . . 69
4.3.1 Linear Network Topology in Underground Environments . . . 69
4.3.2 Energy Consumption and Energy Harvesting for Wireless Self-Contained Sensor Networks . . . 71
4.4 Influence of Magnetic-Inductive Channels on Communication Functionality . . . 71
4.4.1 Non-Flat Magnetic Inductive Fading Channels . . . 72
4.4.2 Magnetic Inductive-Based Modulation and Error Control Coding 74
4.4.3 Energy Consumption for MI Transmissions . . . 78
4.5 Optimal Energy Planning Framework for Wireless Self-Contained Sensor Networks . . . 78
4.6 Performance Evaluation . . . 81
4.7 Highlights . . . 84

V MI-BASED FRACBOT NODE DESIGN FOR MONITORING HYDRAULIC FRACTURES AND OIL RESERVOIRS . . . 85

5.1 Motivation . . . 86
5.2 Related work . . . 87
5.3 Hardware Design Roadmap . . . 89
5.3.1 Hardware Design Requirements . . . 90
5.3.2 Implementation Process . . . 94
5.4 FracBot Hardware Design . . . 96
5.4.1 FracBot microcontroller (MCU) . . . 98

5.4.2 FracBot USB communication 99
5.4.3 Dual NFC Communication 100
5.4.4 Energy-Harvesting Management Unit (EMU) 104
5.4.5 Temperature Sensor 108
5.5 NFC/MI Antenna Design used in FracBot 112
5.5.1 Planar PCB Antenna Design 112
5.5.2 NFC Antenna Equivalent Circuit 113
5.5.3 Transceiver and Receiver Resonance Frequency 114
5.6 FracBot Prototypes 116
5.6.1 FracBot Active Node 116
5.6.2 FracBot Passive Node 118
5.7 Highlights 120
VI FRACBOT TESTBED: PERFORMANCE EVALUATION . . . 122
6.1 NFC/MI Antenna Evaluation 122
6.2 FracBot Propagation Evaluation 125
6.2.1 Experimental Setup 125
6.2.2 Angular Analysis 127
6.3 FracBot Energy-Harvesting Performance 129
6.4 FracBot Underground-like Testbed 131
6.4.1 Modulation Effects 133
6.4.2 Transceiver and Transponder Matching 136
6.4.3 Communication Link Evaluation 137
6.5 Highlights 139
VII CONCLUSIONS 141
7.1 MI-Based Environment-Aware Cross-layer Communication Protocol Design for WUSN in Hydraulic Fractures and Oil Reservoirs 142
7.2 MI-Based Localization for WUSN in Hydraulic Fractures and Oil Reservoirs 143

7.3 Optimal Energy Planning for Self-Contained WUSN in Hydraulic Fractures and Oil Reservoirs 143

7.4 MI-based FracBot Node Design for Monitoring Hydraulic Fractures and Oil Reservoirs 144

7.5 FracBot Testbed: Performance Evaluation 145

REFERENCES **147**

VITA **155**

LIST OF TABLES

1 Transceiver and transponder antenna parameters. 114

2 Antennas characteristics and distances between the NFC transceiver and the receiver. 123

3 Current requirements of FracBot electronics. 130

4 Experimental performance of the ASK and OOK modulation. 138

LIST OF FIGURES

1 A typical oil reservoirs with a hydraulic fracture. 2

2 Protocol stack of the environment-aware cross-layer protocol design. . 13

3 Network topology of multi-hop transmission in WUSNs and a transformer model with the equivalent circuit of a coil pair i-j. 17

4 Frequency response of MI channels at various transmission ranges, working temperatures, and the alignment angles of transceiver coils. . 19

5 Simulated path loss of MI channels at various working temperatures. 20

6 Packet error rate (PER) vs. the SNR for typical underground modulation techniques and BCH(n, k, t) coding schemes. 22

7 Three layer protocol stack for WUSNs in oil reservoirs. 25

8 Pareto optimal front for two-objective optimizations with various transmission ranges. 28

9 Energy per bit for the centralized cross-layer solution, the cross-layer DEAP, and two fixed modulation/FEC combinations. 33

10 Transmitted power for the centralized cross-layer solution, the cross-layer DEAP, and two fixed modulation/FEC combinations. 33

11 Average bit rate for the centralized cross-layer solution, the cross-layer DEAP, and two fixed modulation/FEC combinations. 34

12 Normalized energy consumption for the cross-layer DEAP and the layered framework of protocols 1 and 2. 37

13 Normalized successfully received packet rate for the cross-layer DEAP and the layered framework of protocols 1 and 2. 37

14 MI-based localization system design. 41

15 Randomly-deployed WUSNs (FracBots) in oil reservoir. 44

16 Validation of the fast convergence of **Algorithm 3**. 58

17 Sixty sensors with nf=1 after fast initial positioning (ADM). 59

18 Sixty sensors with nf=1 after the entire localization (ADM+CGA). . 60

19 One hundred sensors with nf=1 after fast initial positioning (ADM). . 61

20 One hundred sensors with nf=1 after the entire localization (ADM+CGA). 61

21 Comparison of the proposed solution and the designated algorithm for 60 sensors in various transmission ranges in a low-noise regime. 62

22 Comparison of the proposed solution with the designated algorithm for 60 sensors in various transmission rages in a high-noise regime. 62

23 Impact of conductivity on the localization performance of the proposed solution in an oil reservoir environment. σ_0 is electrical conductivity at 20^oC. 63

24 Impact of VWC on the localization performance of the proposed solution in an oil reservoir environment. 64

25 Network topology of the MI-based sensor network inside an oil fractured reservoir. 67

26 Topology of the MI-based sensor network in underground environments. 70

27 Front-end and receiver architecture for MI communication. 72

28 Frequency response $H^{MI}(f)$ of MI channels in oil reservoirs. 74

29 The PSD of the modulated signal. 76

30 The comparison of frequency response $H^{MI}(f)$ and PSD. 76

31 Required power to transmit data from sensor to neighbor sensor. . . . 82

32 Energy received by sensors from the base station. 82

33 Packet error rate (PER) vs the SNR (dB) for BPSK and 16QAM modulation techniques and BCH(n,k,t) coding schemes. 83

34 Optimal transmission rate for BPSK and 16QAM modulation techniques and BCH(n,k,t) coding schemes. 84

35 Roadmap of the FracBot design. 90

36 Requirements of the FracBot design. 91

37 Interval mode flowchart. 92

38 Flowchart of a FracBot fabrication. 96

39 Block diagram of the FracBot architecture. 97

40 Active FracBot node. 98

41 Energy-saving clock control. 99

42 Software with USB interface. 100

43 USB controller diagram. 100

44 NFC transceiver. 101

45 NFC dual-interface memory. 102
46 Active tag for microcontroller communication. 103
47 I2C data transfer process. 103
48 Flow process of energy-harvesting. 105
49 Setup of the energy-harvesting process. 105
50 Schematic of an energy-harvesting circuit. 106
51 Integrated circuit voltage range. 107
52 Automatic temperature sensor thresholds. 108
53 Fixed threshold temperature alarm. 109
54 Temperature sensor TMP102. 109
55 Data format and the I2C data frame. 110
56 Multiple devices in the I2C bus. 111
57 Electrical model of the NFC transponder. 113
58 NFC antenna designs. 115
59 (a) Top layer of the PCB design, (b) the 3D PCB design, (c) the top layer board, and (d) the bottom layer board 117
60 Block diagram of the FracBot active node. 117
61 FracBot active node. 118
62 Block diagram of the FracBot passive node 119
63 (A) Top layer of the PCB design, (B) the botton layer of the PCB design, (C) the 3D top layer, and (D) the 3D botton layer. 119
64 FracBot passive node. 120
65 Antennas connection test 1. 124
66 Antennas connection test 2. 125
67 FracBot experimental setup. 126
68 FracBot experimental setup in the lab. 126
69 Power transfer and NFC transponder orientation. 127
70 Angular plots of received power (air). 128
71 Angular plots of received power (air, sand/stone). 129

72 Block diagram of energy transfer. 130
73 Block diagram of energy transfer. 131
74 Underground testbed of the FracBot. 132
75 Underground testbed of the FracBot with the spectrum analyzer. . . 133
76 Input data and ASK 10% and 100% (OOK) modulations. 134
77 Measured received power. 135
78 Received power analysis (air, sand and stone). 136
79 Frequencies responses. 137
80 FracBot node communication. 138
81 Underground signal strength between two FracBot nodes 139

SUMMARY

Wireless underground sensor networks (WUSNs) enable a wide variety of emerging applications that are not possible with current underground monitoring techniques, which require miniaturized wireless sensor systems for mapping hydraulic fractures, monitoring unconventional reservoirs and measuring other wellbore parameters. We call these devices FracBots (Fracture Robots), an extension of RFID (Radio Frequency IDentifcation) tags that realize WUSNs for mapping and characterization of hydraulic fractures in unconventional reservoirs.

The objective of this thesis is to design fully integrated magnetic induction (MI)-based FracBots (WUSNs) that enable reliable and efficient wireless communications in underground oil reservoirs for performing the in-situ monitoring of oil reservoirs. This is very crucial for determining the sweet spot of oil and natural gas reserves. To this end, we have contributed in four areas as follows: first, we develop a novel cross-layer communication framework for MI-based FracBot networks in dynamically changing underground environments. The framework combines a joint selection of modulation, channel coding, power control and a geographic forwarding paradigm. Second, we develop a novel MI-based localization framework that exploits the unique properties of MI-field to determine the locations of the randomly deployed FracBot nodes in oil reservoirs. Third, we develop an accurate energy framework of a linear FracBot network topology that generates feasible nodes' transmission rates and network topology while always guaranteeing sufficient energy. Then, we design, develop, and fabricate MI-based FracBot nodes. Finally, to validate the performance of our solutions in our produced prototype of FracBot nodes, we develop a physical MI-based WUSN testbed.

CHAPTER I

INTRODUCTION

Economies worldwide depend on a consistent supply of energy, about 87% which currently comes from fossil fuels. Reasonable projections indicate that despite rapid growth of renewable energy sources, fossil fuels will still provide around 80% of the world energy in 2030. A rapidly growing fraction of this energy is derived from unconventional reservoirs [1], in which the current achievable oil recovery rate, the ratio of recoverable oil to total oil in the reservoirs, is less than 60% despite the use of state-of-the-art extraction technologies [2]. Given tepid growth in new conventional fossil reserves, vital technical goals include increasing recovery factors beyond 60% for conventional reservoirs [3] and improving reservoir contact and extraction efficiency in unconventional reservoirs. These goals could be achieved given spatial and temporal information about pressure, temperature, and fluid composition throughout the reservoir.

Current reservoir [4] and wellbore monitoring systems [5] are not able to measure data deep inside oil reservoirs, and no existing technology is capable of providing in-situ monitoring of conventional reservoirs in real time [2],[6]. As a result, in-situ sensing techniques for collecting data throughout reservoirs have drawn considerable attention from researchers, most of whose efforts have been devoted to the development of small sensors that can withstand the severe conditions inherent in oil reservoirs [2]. Such sensors, or nodes have been successfully injected into oil reservoirs [7]. Figure 1 depicts a typical oil reservoirs that has undergone the process of hydraulic fracturing. Oil is extracted from a well-bore drilled into an oil reservoir at a depth of around 7,000 feet, and hydraulic fracturing is used to make a thin crack inside the

rock formation to access more oil and natural gas.

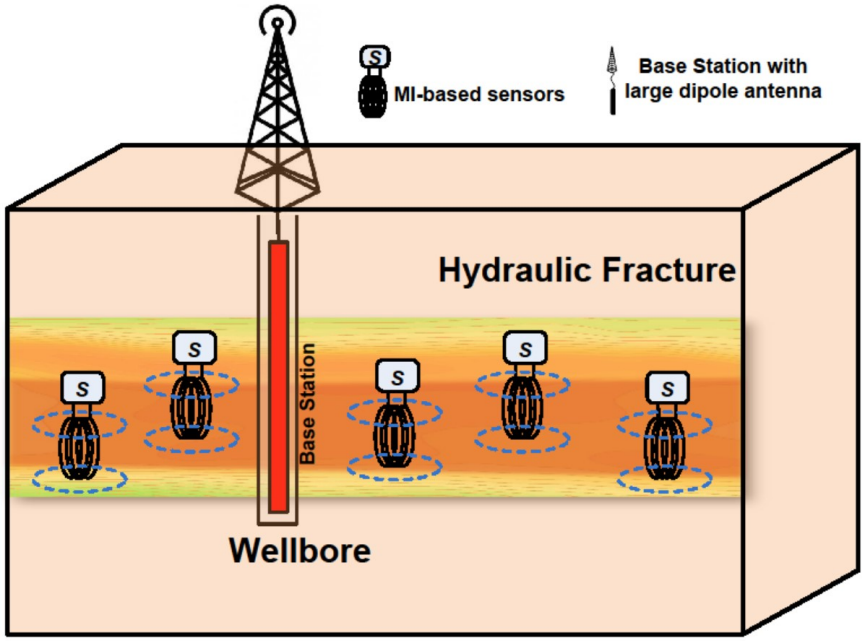

Figure 1: A typical oil reservoirs with a hydraulic fracture.

Wireless Underground Sensor Networks (WUSNs) are envisioned to provide monitoring capabilities and map topology in underground oil reservoirs. To overcome the environmental challenges presented by oil reservoirs, WUSNs based on the magnetic induction (MI) technique was proposed in [8]. As classical electromagnetic (EM) waves are unable to work properly in oil reservoirs, an alternative approach is the MI technique, which enables wireless communication in oil reservoirs and deals with the underground challenges. It transmits the data over the near magnetic field of antennas resulting in achieving constant channel conditions using small size antennas. In our case, the sensor nodes use an MI coil antenna to generate and receive wireless signals through magnetic coupling that can efficiently penetrate a high-loss oil reservoirs and realize the wireless communication [9]. The work in this thesis involves the development of miniaturized transponder systems for mapping hydraulic

fractures, monitoring unconventional reservoirs, and measuring other wellbore parameters. These devices, called FracBots (Fracture Robots), are envisioned as an extension of RFID (Radio Frequency IDentifcation) tags that realize wireless underground sensor networks (WUSNs) for mapping and characterization of hydraulic fractures in unconventional reservoirs. Accordingly, we propose a system model for FracBots in oil reservoirs, shown in Figure 1. The system architecture of the MI-based sensor network has two layers:

1. **FracBot (sensor) nodes** in the oil-fractured reservoir that are injected into the fracture during the hydraulic fracturing process. Since the fracture is very thin, the positions of the nodes are randomly distributed inside the fracture. Despite having no power source, the sensor nodes are wirelessly charged by the radiation of the base station inside the wellbore.

2. **A base station**, which consists of a large antenna at the wellbore, connected to an aboveground gateway.

The objective of this thesis is to design full integrated MI-based FracBots (WUSNs) to enable reliable and efficient wireless communications in underground oil reservoirs for in-situ monitoring of oil reservoirs. Such a capability is crucial to determining the sweet spot of oil and natural gas reserves. To this end, we have contributed in four areas as follows: First, we develop a novel cross-layer communication framework for MI-based networks in dynamically changing underground environments. The framework combines a joint selection of modulation, channel coding, power control and a geographic forwarding paradigm. Second, we develop a novel MI-based localization framework that exploits the unique properties of MI field to determine the locations of the randomly deployed FracBot nodes in oil reservoirs. Third, we develop an accurate energy framework of a linear FracBot (sensors) network topology that gives feasible

sensor transmission rates and a sensor network topology while consistently guaranteeing sufficient energy. Then, we design, develop and fabricate MI-based FracBot nodes. Finally, we develop a physical MI-based WUSN testbed to validate the performance of our solutions in our produced prototype of FracBot nodes.

1.1 Hydraulic Fractures

Hydraulic fracture (HF) technology is almost universally required to access tight unconventional oil and gas reservoirs. In the United States, an estimated 90% of natural gas wells use HF technology to produce as an economical rate. Hydraulic fracturing, frequently employed to improve reservoir contact and production rates in the oil and gas industry, has been used for over 60 years in more than one million wells and is commonly applied to wells drilled in low permeability reservoirs. Successful hydraulic fracturing is generally considered vital for economical production of natural gas from shale beds and other tight gas plays [10].

HF is formed by pumping a fluid into the wellbore at a rate sufficient to increase the pressure downhole to a value in excess of the fracture gradient of the formation rock. The pressure causes the formation to crack, allowing the fracturing fluid to enter and extend the crack further into the formation. To keep this fracture open after the injection stops, a solid proppant is added to the fracture fluid. The proppant, which is commonly sieved round sand or other porous material, is carried into the fracture. Such material must be higher in permeability than the surrounding formation, and the propped HF then becomes a high permeability conduit through which the formation fluids can flow to the well.

Although observing and optimizing fracture quality and reservoir contact is of vital importance, determining the size and the orientation of a completed HF is a difficult, expensive, inaccurate, and longstanding problem [11]. Accordingly, we have recognized that an improved means of ascertaining these features is sorely needed. Of

the many approaches available, microseismic and tiltmeter surveys have been the most successful but they are costly, inaccurate, and time consuming; more importantly, they unfortunately tell us nothing about the inner workings of the reservoir [12].

The distance at which rock faces are separated during HF is called the fracture width. Practical fracture widths range from about one millimeter to about one centimeter. The sands, or similar materials used to open HFs are, therefore, typically about one millimeter in diameter or less. Accordingly, we recognize the existence of significant physical constraints on mapping devices that could be deployed within the HF. For example, any transponders used for mapping HFs and reservoir parameters must be able to physically fit into, not just simply adjacent, to fracture, at a considerable depth. Thus, to ensure passage, it should be no more than about one millimeter in at least one dimension.

This arbitrary scaling on the transponder side would not generally be possible for tags that would be required to fit through open HFs, and thus, would face significant size limitations, especially in applications in which the form factor, in particular, is constrained. A complete mapping of HFs requires a transmission range on the order of 100 meters or so. Accordingly, we recognized the need for systems that provide transponders or tags that are sufficiently small for deployment through an open or opening HF and have a communication range with a node of up to 100 meters or more when deployed within an HF of a reservoir.

1.2 Wireless Underground Sensor Networks (WUSNs)

In response to the need for a system of mapping of HFs, we turn to wireless underground sensor networks (WUSNs), wireless sensor nodes operating below the ground surface. A wireless sensor node is a small wireless device that encompasses a microcontroller, a radio transceiver, an antenna, a power source, and one or more sensors. The node functions via a lightweight operating system that entails features such as

wireless communication, remote access, and sensing capabilities [13]. WUSNs are envisioned to provide real-time monitoring capabilities in challenging underground environments, including soil media, oil reservoirs, and underground mines and tunnels. WUSNs enable a wide variety of emerging applications not possible with current underground monitoring techniques. Compared to current underground sensor networks, which use wired communications methods for network deployment, WUSNs entail the timeliness of data, ease of deployment and data collection, concealment, reliability, and coverage density. Despite these advantages, the realization of WUSNs poses many challenges, the foremost of which is the realization of energy efficient and reliable communications that establish multiple hops underground and efficiently collect and disseminate data for seamless operation. The realization of WUSNs will benefit many emerging applications such as intelligent agriculture, underground pipelines and power grid monitoring, oil reservoir monitoring, concealed border patrol, earthquake and landslide forecasting, and underground mine disaster prevention and rescue [14].

1.3 MI-Based Underground Communications

Different from conventional EM-based communication, MI-based communication exhibits highly reliable and constant channel conditions with sufficiently large communication range in the underground environment. First, underground media such as soil, sand, water, and crude oil cause little variation in the attenuation rate of magnetic fields from that of air, since the magnetic permeability of each of these materials is similar. Second, the multi-path fading is negligible in underground MI systems because the communication range in these systems is within one wavelength. Third, transmission and reception are accomplished with the use of a small wire coil. Unlike the EM wave-based technique, MI-based communication has no cutoff frequency. Hence, a small coil antenna is sufficient for MI-based communication even for low

frequency signals. A study in [14] analyzed the channel capacity of MI communication from a pair of coil transceivers, and another in [15] thoroughly investigated near-field inductive communication systems with regard to channels created between two or more magnetically coupled coils. The authors of [16] proposed coil deployment algorithms for MI-based WUSNs. Considering wireless power transfer, a study in [17] presented a propagation model and MI link budget for wireless power transfer systems, and the MI technique employed in [18] efficiently transferred wireless energy over relatively long distances.

1.4 Research Objectives

In this thesis, we design miniaturized FracBots devices (Fracture Robots) for mapping hydraulic fractures, monitoring unconventional reservoirs and measuring other wellbore parameters. FracBots are based on WUSNs. In another word, we design full integrated MI-based WUSNs that enable the reliable monitoring of hydraulic fractures and unconventional reservoirs. When the FracBots are injected during hydraulic fracturing operations, autonomous localization algorithms can be used to create constellation maps of proppant beds as placed. To explore this concept, we develop a FracBot prototype platform and demonstrate three key functions. We begin by developing a novel cross-layer communication framework for MI-based FracBot networks in dynamically changing underground environments. The framework combines the joint selection of modulation, channel coding, power control, and a geographic forwarding paradigm. Second, we develop a novel MI-based localization framework that exploits the unique properties of the MI field to determine the locations of randomly deployed FracBot nodes. Third, we develop an accurate energy model framework for a linear FracBot network topology that estimates FracBot data transmission rates while respecting harvested energy constraints. Forth, we design, develop and fabricate MI-based FracBot nodes. Finally, we develop a physical MI-based WUSN testbed to

validate the performance of our solutions in MI-based FracBot nodes.

1.4.1 MI-Based Environment-Aware Cross-layer Communication Protocol Design for WUSN in Hydraulic Fractures and Oil Reservoirs

The techniques for the typical terrestrial wireless sensor networks are not directly applicable to WUSNs because of the significant differences between the communication media (e.g., between the soil and the air). So far, most of the work has focused on the physical layer, such as the design of antennas and analyses of the receiving signal. However, studies have not proposed any protocol solutions for MI-based WUSNs. Therefore, in this thesis, instead of taking the classical layered protocol approach (the seven-layer open systems interconnection model (OSI model)), we develop a fully distributed cross-layer protocol framework referred to as the distributed environment-aware protocol (DEAP), which includes a three-layer protocol stack and accounts for the interactions of various layer functionalities, and thus provides efficient resource utilization and achieves high system performance.

1.4.2 MI-Based Localization for WUSN in Hydraulic Fractures and Oil Reservoirs

Most applications of WUSNs such as mine and oil reservoirs monitoring are location dependent, requiring precise sensor positions. However, classical localization solutions, based on the propagation properties of electromagnetic waves, do not function well in underground environments because of their extremely short communication ranges, highly unreliable channel conditions, and large antenna sizes. In this thesis, we develop a MI-based localization that accurately and efficiently locates randomly-deployed sensors in underground environments by leveraging the multi-path fading free nature of MI signals.

1.4.3 Optimal Energy Planning for Self-Contained WUSN in Hydraulic Fractures and Oil Reservoirs

Wireless sensor nodes are a promising technology for collecting data from oil reservoirs in real time. The sensor nodes, however, are not sufficient for transmitting the required data within a power budget because of limitations caused by the very small size of the sensors and the environment. To overcome limitations caused by harsh environmental conditions and power constraints, we develop an accurate energy model framework of FracBot WUSN topology that affords feasible sensor transmission rates and FracBot topology while ensuring a sufficient amount of energy.

1.4.4 MI-based FracBot Node Design for Monitoring Hydraulic Fractures and Oil Reservoirs

The monitoring of hydraulic fractures and unconventional oil and gas reservoirs are crucial for determining the rich venue of oil and natural gas reserves. Although wireless sensor nodes are a promising technology for collecting data from hydraulic fractures and oil reservoirs in real time, such nodes are not commercially available for this use since they have yet to be designed for this special application that requires overcoming limitations caused by the small size requirements and the environment. To overcome limitations caused by harsh environmental conditions and energy constraints, we propose a novel prototype of MI-based wireless sensor node (FracBot) to be used as a platform for a new generation of WUSNs for monitoring hydraulic fractures and unconventional reservoirs, and measuring other wellbore parameters. We design and develop the hardware of the MI-based wireless sensors for short range communication using near-field communication (NFC) as a physical layer combined with an energy harvesting capability and ultra-low power requirements. We realize theses characteristics using cost-effective and commercial off-the-shelf components.

1.4.5 FracBot Testbed: Performance Evaluation

Despite the numerous theoretical studies in this area, few efforts have been devoted to developing and evaluating a sensor node (FracBot) for underground environments that confirms the theoretical outcomes. We evaluate our FracBot nods and network in a reservoir-like environment. We design the FracBot testbed, which includes different media such as air, water, sand, and stone. One of the main results is that the sand and stone media affects the performance of the FracBot which eventually degrade the MI signal propagation and reduce the transfer of energy. Thus, an evaluation of hardware will enable us to understand the challenges, improve the electronic sensitivity, and optimize the minimum resources necessary to miniaturize the FracBot hardware.

1.5 Organization of the Thesis

The remainder of this thesis is organized as follows. Chapter 2 presents the environment-aware, cross-layer communication protocol design in oil, and Chapter 3 explains the development of MI-based localization for FracBot networks in oil reservoirs. Chapter 4 explores optimal energy planning for wireless self-contained FracBot networks in oil reservoirs. Chapter 5 illustrates the design, development, and fabrication of the MI-based sensor nodes, and Chapter 6 presents the physical MI-based FracBot testbed and validates the performance and practical aspect of the proposed solutions. Finally, Chapter 7 summarizes the research results.

CHAPTER II

MI-BASED ENVIRONMENT-AWARE CROSS-LAYER COMMUNICATION PROTOCOL DESIGN FOR WUSN IN HYDRAULIC FRACTURES AND OIL RESERVOIRS

In this chapter, we introduce a distributed cross-layer framework for MI-based wireless underground sensor networks (WUSNs) in oil reservoir published in [19]. we develop a cross-layer resource allocation framework that accurately models every aspect of the layered network architecture, integrates different communication functionalities into a coherent framework, and provides distributed cross-layer solutions. The motivation for this work is provided in Section 2.1. Section 2.2 discusses the related work. Section 2.3 introduces the system model, and Section 2.4 covers the effects of environment- dependent parameters on MI-based communication in oil reservoir environments. Section 2.5 introduces an environment-aware three-layer protocol stack. Section 2.6 presents the environment-aware cross-layer optimization framework, and Section 2.7 presents the design of the distributed environment-aware protocol (DEAP). Section 2.8 evaluates our cross-layer communication solution, and Section 2.9 concludes.

2.1 Motivation

The techniques for typical terrestrial wireless sensor networks are not directly applicable to WUSNs because of the significant differences between the communication media (e.g., between the soil and the air). So far, while most studies have examined the physical layer such as the design of antennas and the analysis of receiving signals, no study has proposed protocol solutions for MI-based WUSNs. In this work,

instead of taking the classical layered protocol approach (i.e., the seven-layer Open Systems Interconnection (OSI) model, we develop a fully distributed cross-layer protocol framework called DEAP for MI-based WUSNs. Our solution satisfies the QoS requirements of diverse applications and achieves optimal energy consumption and high throughput efficiency with low computational complexity. As a result of these features, our solution is useful for practical implementations. We summarize our cross-layer solution framework as follows:

1. It evaluates critical information about the environment of underground oil reservoirs that affects the quality of transmission of MI-based communication.

2. It constitutes a three-layer protocol stack for WUSNs in underground oil reservoirs.

3. As a cross-layer framework, it jointly optimizes the communication functionalities of various layers.

4. It provides Distributed Environment-Aware Protocol (DEAP) design that solve the proposed cross-layer framework.

Figure 2 depicts the protocol stack for the environment-aware cross-layer protocol design and our four main contributions. To achieve efficient MI communication in the underground environment, our solution, based on a distributed optimization problem, jointly controls physical, MAC and routing functionalities. Therefore, we begin by examining the effects of temperature, electrical conductivity, magnetic permeability, and coil resistance on MI-based communication. Then we adopt several simple but effective modulation schemes such as BPSK, QPSK, and BFSK to reduce energy consumption while accounting for channel coding such as the multilevel cyclic BCH code. Moreover, we design and use a MAC protocol to simplify performance degradation caused by interference signals. In particular, our solution determines

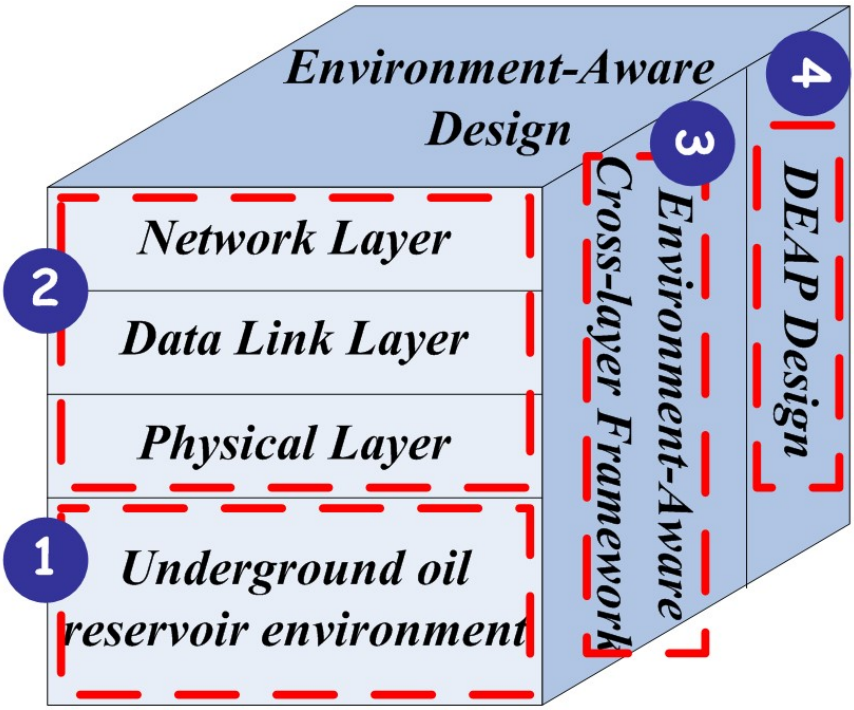

Figure 2: Protocol stack of the environment-aware cross-layer protocol design.

the optimal selection of modulation, FEC, and transmit power (physical functionalities), a DS-CDMA medium access control scheme with a power control constraint to access the bandwidth-limited MI channels (MAC functionality), and a geographical routing algorithm (routing functionality). Therefore, the proposed cross-layer framework captures all functionalities of each protocol layer. Finally, we develop a cross-layer DEAP solution to solve the optimization problem of the framework in a distributed manner. Capturing the underground MI channels for high utilization, it is environmentally aware, consumes minimal energy, and involves limited computation complexity in WUSNs.

2.2 Related Work

In the past decade, cross-layer protocol solutions have generally been recognized as suitable for the resource-efficient design of wireless sensor networks [20]. The literature

consists of numerous studies that have directly contributed to our knowledge of terrestrial wireless sensor networks. One integrated cross-layer study [21]characterized multiuser access interference (MAI) and network connectivity in wireless CDMA-based sensor networks. Another study [22] formulated cross-layer energy and delay optimization as a convex problem for synchronous small-scale sensor networks to quantify the tradeoff between delay and energy consumption. Furthermore, using an initiative concept, a study in [23] proposed a single cross-layer module that achieves congestion control, routing, and medium access control concurrently for terrestrial wireless sensor networks, and another study [24] developed a multimedia cross-layer protocol for underwater acoustic sensor networks in order to support differentiated services and to efficiently share the high-delay underwater medium. However, the challenges of wireless EM communication in underground environments prevent using the above solutions from the existing literature [25]. Regarding the networking aspects of MI communication, the authors of [26] examined the signal-to-noise ratio (SNR), connectivity, and bandwidth in 3D underwater MI channels. Then a paper [27] proposed multi-hop relay techniques to extend the range of near-field MI communication systems.

The authors of [28] provided a general description of WUSNs and identified a cross-layer, environmentally-aware protocol design as open research issues. In their study, they accounted for WUSNs that bury sensors at the subsurface of the soil, defined as the top several meters of the soil (i.e., the topsoil or subsoil region). By contrast, our solution aims at underground oil reservoirs that typically bury sensors in deep-soil regions at depths of around 7,000 ft. and discusses communications through soil via the propagation of electromagnetic (EM) waves rather than MI communications. Specifically, while the EM technique can operate in the 300-900 MHz frequency band, which accommodates a small size antenna for easy sensor development, the channel condition is greatly affected by the environmental state. The MI technique, however,

functions at a low frequency (around tens of MHz or lower), involves small coils as antennas, and stabilities the channel condition for high-quality transmission. In addition, it does not disclose the three-layer protocol stack for the MI communications of WUSNs. Specifically, the authors of [28] did not examine the communication protocol stack design for wireless communication (i.e., EM wave propagation) in underground environments.

A study in [29] presented a self-adaptive modulation method and system for WUSN. The study discloses that the self-adaptive modulation method consists of the following steps: detecting the water content of a current node, receiving the water content sent by an adjacent node, and determining a modulation and coding (AMC) mode used for sending a following data frame. According to the self-adaptive modulation method and system for the WUSN, by utilizing the relationship between the channel characteristics of the WUSN and the soil environment, the real-time AMC function of WUSN node equipment can be simply realized. However, this patent does not disclose MI communications, the three-layer protocol stack, or the cross-layer framework, for MI communications. Specifically, EM wave propagation is considered rather than MI communication in underground environments. The study discloses the AMC design, which belongs to the physical-layer communication functionality, with respect to Volumetric Water Content (VMC) as a single piece of environment information. Also, the authors of [29] did not discuss distributed environmental-aware design. However, our solution entails use of the three-layer protocol stack, which includes all physical and network-layer communication functionalities. It also investigates the fundamental impact factors from underground environments, such as temperature, electrical conductivity, and magnetic permeability, and also provides the impact of VMC in the designated cross-layer framework.

So far, most studies have explored the physical layer, such as the design of antennas, and the reception of signal analysis but the literature lacks studies that provide

protocol solutions for MI-based WUSNs. However, a study in [30] provided a general cross-layer protocol solution satisfies the QoS requirements of MI communication at operating frequency of 7 MHz for WUSNs and achieves optimal energy consumption and high throughput with low computational complexity. Our proposed environment-aware distributed cross-layer framework is designed for MI-based WUSNs in oil reservoir. It integrates different communication functionalities into a coherent cross-layer framework that can be used for oil reservoir environment and works at operating frequency of 13.56 MHz. Our framework is an extension of the cross-layer protocol solution presented in [30].

2.3 System Model

This section presents the system model presented in [19] for the MI-based communication over WUSNs in hydraulic fractures and oil reservoirs. The MI communication link is formed by the induction between the primary and secondary coils. In Figure 3, the paramters are: a[cm] (radius), number of turns N and r[m] (i.e., distance between the transmitter and the receiver). This MI transceiver can be modeled as two transformers as shown in Figure 3, where V_S (voltage) , Z_L (load impedance o the receiver), M (mutual induction), R (resistance), H (self induction of coil), and C (loaded capacitor). Furthermore, the equivalent circuit of such a model is obtained as $Z = R + j\omega H + 1/(j\omega C)$, $Z_{rflt} = \omega^2 M^2/(Z + Z_L)$, and $V_M = j\omega M i_t$. As shown in [25], the magnetic permeability of the medium is the environmental factor dominating the quality of the MI communication. Specifically, although the permeability of soil and water is similar to that of air (i.e., $\mu_0 = 4\pi \times 10^{-7}$[H/m]), such a factor and resistance will change with respect to variable temperatures at different underground depths. medium permeability also acts differently with regard to the composites of underground magnetic contents. The effects are characterized as

$$\mu = \mu_0(1+\chi) = \mu_0(1 + p_{para}\frac{\hat{c}}{T} + p_{ferro}\chi_{ferro}), \quad (1)$$

$$R = 2\pi a N R_0[1 + \alpha_{Cu}(T - T_0)], \quad (2)$$

where χ and χ_{ferro} are the magnetic susceptibilities of the medium and ferromagnetic contents, respectively, p_{para} and p_{ferro} are the ratio of paramagnetic and ferromagnetic composites, respectively, $\hat{c}$ is the constant, $\alpha_{Cu} = 3.9 \times 10^{-3}[/^{\circ}\text{K}]$ is the temperature coefficient of copper coil, $T[^{\circ}\text{K}]$ is the actual underground temperature, and $T_0[^{\circ}\text{K}]$ is the room temperature and $R_0[\Omega/\text{m}]$ is the corresponding resistance of a unit length of coil.

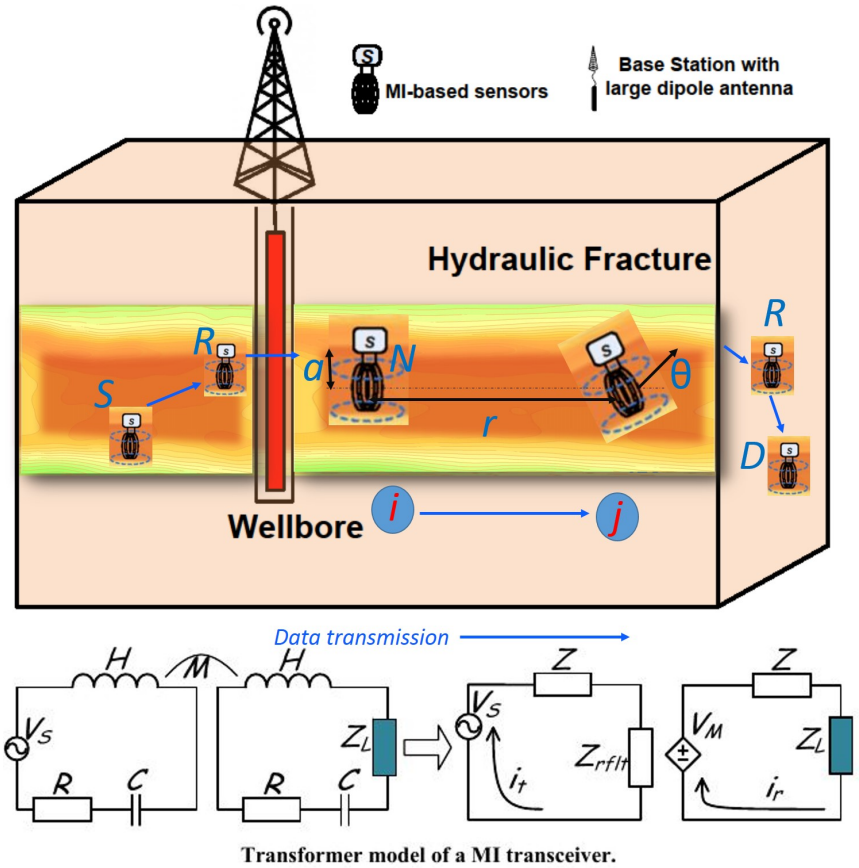

Figure 3: Network topology of multi-hop transmission in WUSNs and a transformer model with the equivalent circuit of a coil pair i-j.

2.4 The Effects of Environment-Dependent Parameters on the MI-based Communication in the Oil Reservoir Environment

In this section, we examine the MI channel model in terms of path loss and bandwidth, present possible modulation and FEC techniques suitable for the underground environment, and evaluate their performance. Then, we introduce the DS-CDMA MAC scheme and location-based routing functionalities.

2.4.1 MI Channel Model

To fit the environment-aware design to oil reservoirs, the operating temperature T and electrical conductivity α of medium are measured by a sensor node in the WUSNs. The temperature, which refers to that of a specific location where the sensor is positioned, can be used to characterize the communication quality of MI-based communication. Furthermore, self and mutual inductances, the loaded capacitance, and the receiver impedance are also analytically obtained by the following process. With the modeling of magnetic dipole for a coil, self and mutual induction is calculated via Stoke's theorem [31]: $H \simeq \mu\pi a N^2/2$ and $M(T,\sigma) = \mu\pi N^2 a^4 G(r,\sigma)\cos\theta/4r^3$, where σ[S/m] is the medium conductivity and $G(\cdot,\cdot)$ is the attenuation factor resulting from the skin depth effect. Such a loss factor largely destroys the transmission quality when encountering the salty water in the soil, as explained in [32]. The capacitor is then designed to neutralize the coil impedance Z at the angle frequency of the transmitted signal (i.e., $j\omega H + 1/(j\omega C) = 0$). In addition, to maximize the transmitted power efficiency, load impendence Z_L is designed to be the complex conjugate of the output impendence of receiver coil. Therefore, $C = 2/(\omega^2\mu\pi a N^2)$ and $Z_L = \bar{Z}$ are obtained. The path loss and the bandwidth can be calculated or evaluated based on T and α, μ and R. For example, according to circuit theory, with the coil model in Figure 3,

the path loss can be obtained as

$$L_{MI}(r, f_0, \theta, T, \sigma)\ [\text{dB}] = 10 \lg \frac{2(2R^2 + \omega_0^2 M^2)}{\omega_0^2 M^2} \approx 10 \lg \frac{4R^2}{\omega_0^2 M^2} \triangleq 10 \lg \frac{1}{\varepsilon\,(r, f_0, \theta, T, \sigma)}. \tag{3}$$

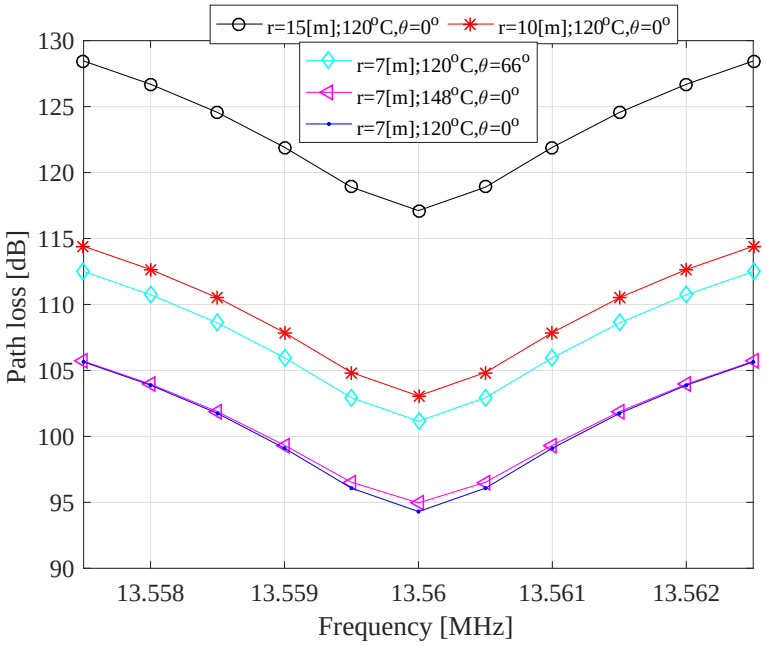

Figure 4: Frequency response of MI channels at various transmission ranges, working temperatures, and the alignment angles of transceiver coils.

To provide a satisfactory cross-layer design for practical oil reservoirs, our cross-layer framework is able to optimize the corresponding transmission parameters by capturing the unique impact of environment parameters, which can be shown in Figure 4 and Figure 5. Figure 4 shows the frequency response of MI channel under the oil reservoir environment. The figure shows that the 3-dB bandwidth is around 1 KHz at operating frequency of 13.56 MHz and that it is not affected by the transmission range and alignment angles. Figure 5 shows the path loss of a single transmitter-receiver pair with respect to the transmission distance at various temperatures. As the temperature rises, the path loss increases and thus degrades the quality of the link transmission. Our framework captures such environment-dependent bandwidth and path loss behavior because communication parameters adjust according to the

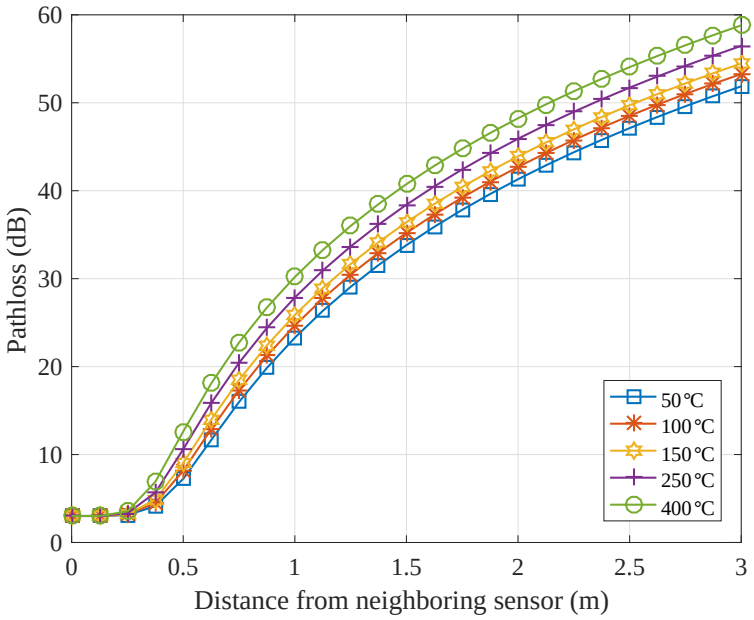

Figure 5: Simulated path loss of MI channels at various working temperatures.

changes in both the link data rate and the SINR value, which are functions of the environmental parameters of oil reservoirs.

2.4.2 Modulation and FEC

MI communications enjoy less channel variation than EM waves, as indicated in [8]. Because of undesired noise, mainly from the thermal vibration of circuit elements, additive white Gaussian noise (AWGN) is a suitable modeling. Thus, the modulation and channel coding functionalities are analyzed as follows. As a result of energy-limited WUSNs, more sophisticated modulation techniques entail high energy consumption. However, several simple and suitable modulation schemes, such as BPSK, BFSK, DBPSK, and 16-QAM, can be selected for the wireless underground communications. Given the communication link i-j, $m_{ij} \in \mathcal{M}$ denotes the adopted modulation technique and $\eta(m_{ij})$ denotes the corresponding modulation spectrum efficiency. As bit error rate (BER) $\Psi(T, \sigma)$ usually refers to the received SNR, $\Psi_{ij}^{m_{ij}}\left(P_{ij}\eta B_{MI}/R_{ij}L_{MI}N_0\right)$ can be obtained for the modulation technique m_{ij} over

link i-j, where N_0[W] represents thermal noise power and $R_{ij}(T,\sigma)$[bps] is the transmitted bit rate.

Regarding the channel coding schemes, while forward error correction (FEC) enhances link transmission reliability without additional re-transmission costs and overhead, automatic repeat request (ARQ) does. Furthermore, along with high energy efficiency, block codes are less complex than convolutional codes (CC). In particular, a multilevel cyclic BCH (Bose, Ray-Chaudhuri, Hocquenghem) code outperforms the most energy-efficient CC by almost 15% for an optimal packet size in wireless sensor networks as in [33]. Thus, this study examines the BCH code; however, we can extend our framework to support more energy-consuming schemes, such as Reed-Solomon codes, CCs, turbo codes ans different types of ARQ. For the link i-j, $c_{ij} \in \mathcal{C}$ denotes an adopted coding scheme with coding rate R_C^{ij}. As far as $BCH(n,k,t)$ code with rate $R_C = k/n$ is concerned, n denotes the block length, k denotes the payload length, and t denotes the correcting capability of bit error (i.e., $t < n$). Given the BER $\Psi(T,\sigma)$, the block error rate Ψ_B becomes

$$\Psi_B(T,\sigma) = \sum_{i=t+1}^{n} \left(\begin{array}{c} n \\ i \end{array} \right) \Psi^i (1-\Psi)^{n-i}. \tag{4}$$

Also, with L[bit] being the packet length, the packet error rate (PER) Φ is obtained as

$$\Phi(T,\sigma) = 1 - (1-\Psi_B)^{\lceil \frac{L}{k} \rceil}, \tag{5}$$

which can be approximated as $\lceil L/k \rceil \Psi_B$ when Ψ_B is small.

Figure 6 shows PER vs. SNR for various modulation techniques and different BCH(n,k,t) codes but no FEC scheme. The transmission range is set to 7m and the packet length to 100 Bytes. As suggested in the specification of soil temperature sensors in [34], we select a working temperature of 283°K. While BPSK achieves smaller BER for any given SNR among thw modulation techniques, it delivers the best PER

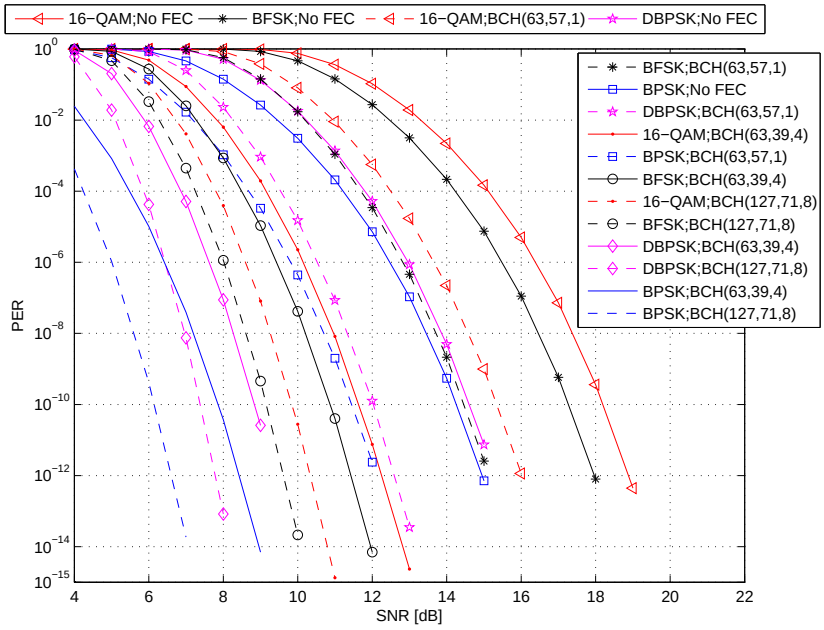

Figure 6: Packet error rate (PER) vs. the SNR for typical underground modulation techniques and BCH(n, k, t) coding schemes.

performance for every channel coding schemes. In addition, while consuming more energy, powerful coding schemes (i.e., with high error correcting capability t) maintain a lower PER for any given SNR. A tradeoff exists between energy consumption and transmission quality.

2.4.3 MAC Protocol and Geographical Routing Algorithm

Motivated by [24] in underwater acoustic sensor networks, our proposed MAC protocol, the DS-CDMA scheme compensates the drawbacks of multi-path effects and achieves high channel reuse as well as low number of packet retransmissions. Thus, it decreases the energy consumption and increases the network throughput. As chaotic codes [35] provide much higher granularity with less constraint in code properties than the pseudo-random sequences, a chaotic code with length l_{ij} [bit] $\in \mathcal{L} = [l_{min}, l_{max}]$ is adopted for transmissions over link i-j. Corresponding spreading factor g_{ij} is proportional to the code length (i.e., $g_{ij} = \nu l_{ij}$ with the proportional factor ν), and the transmission bit rate $R_{ij}(T, \sigma)$ becomes $\eta B_{MI}(T, \sigma)/l_{ij}$. To implement such a scheme

in WUSNs, the near-far effect and MAI [36] need to be minimized. In other words, the signals that arrive at the receiver should have approximately the same mean power; interference from simultaneous transmissions of different users, which should also be well controlled. are satisfied via power control design as follows.

It is assumed that r_{min}^{j} denotes the minimum received signal-to-interference-plus-noise ratio (SINR) of node j for successful transmissions and the aggregated interferences to receivers are Gaussian distributed. With regard to the transmitted power level P_{ij}, the lower bound should provide r_{min}^{j} at node j; however, the upper bound should concern both the maximum power P_i^{max}[W] and the interference to nodes $k \in \Xi_i^T$, where Ξ_i^T is the set of nodes whose ongoing communication is affected by node i's transmission, shown in Figure 3. Specifically,

$$\begin{aligned} \varepsilon_{ij}(T,\sigma) g_{ij} P_{ij} \geq r_{min}^{j} \left(I_j + N_0\right) \Rightarrow \\ P_{ij} \geq \frac{N I_j}{g_{ij} (r_{min}^{j})^{-1} \varepsilon_{ij}(T,\sigma)}, \end{aligned} \tag{6}$$

where $\varepsilon_{ij}(T,\sigma)$ is the MI channel gain of link i-j from (3) and NI_j summarizes the noise and MAI power at node j with I_j being the interference at j. Furthermore, at each node $k \in \Xi_i^T$, the following inequality should be satisfied:

$$\begin{aligned} (r_{min}^{k})^{-1} \varepsilon_{t_k k}(T,\sigma) g_{t_k k} P_{t_k k} - N_0 - \hat{I}_k \geq \varepsilon_{ik}(T,\sigma) P_{ij} \Rightarrow \\ \frac{(r_{min}^{k})^{-1} g_{t_k k} P_{t_k k} \varepsilon_{t_k k}(T,\sigma) - N_0 - \hat{I}_k}{\varepsilon_{ik}(T,\sigma)} = P_{ij}^{(k)}(T,\sigma) \geq P_{ij}, \end{aligned} \tag{7}$$

where $\hat{I}_k$ is the interference for the transmissions of t_k to k, except the one from node i, i.e., $\hat{I}_k = (\sum_{\beta \in \Xi_k^R / \{i\}} \sqrt{\varepsilon_{\beta k} P_{\beta r_\beta}})^2$. While there are $|\Xi_i^T|$ nodes for the set Ξ_i^T, the maximum power P_{ij} with respect to these SINR requirements becomes $\min_{k \in \Xi_i^T} P_{ij}^{(k)}(T,\sigma)$. The power constraint is then

$$\frac{N I_j}{g_{ij} (r_{min}^{j})^{-1} \varepsilon_{ij}(T,\sigma)} \leq P_{ij} \leq \min(\min_{k \in \Xi_i^T} P_{ij}^{(k)}(T,\sigma), P_i^{max}). \tag{8}$$

In our routing layer, we utilize geographical routing protocol [37, 38] because of its scalability feature and limited signaling overhead requirements. Addressing the distributed algorithm design, a source or relay node i will select its best next hop j^* with respect to the given objective function, such as E_{ij} and Q_{ij} in (9) or EaT_{ij} in (10), among the set of $S_i \cap F_i^D$. S_i is the neighbor set of node i, which includes the possible forwarder j and nodes with ongoing communication affected by i's transmissions (i.e., $S_i = \{j, \Xi_i^T\}$ following previous notation). F_i^D is the forwarding set, which consists of nodes closer to destination D than node i, i.e., $z \in F_i^D$ if and only if $r_{zD} < r_{iD}$. To expedite the per-node based decision, such geographical routing solution should map the end-to-end delay requirements into local delay requirements. Specifically, with an incoming packet to node i, the expected hop delay to node j (i.e., T_{ij}[s]) can be calculated as: $T_{ij} = \frac{T_{iD}}{N_{iD}^{(j)}} = \frac{T_{max}-(t_{now}-t_0)}{r_{iD}/(r_{iD}-r_{jD})}$, where T_{iD}[s] is the time-to-live of the arrival packet at node i, T_{max}[s] is the expected maximum end-to-end delay, t_{now} is the time when the packet arrived at node i, t_0 is the time that the packet was initially transmitted, and $N_{iD}^{(j)}$ is the expected number of hops needed from node i, via node j, to destination D. Also, the expected number of hops for the corresponding end-to-end path (i.e., from source, via link i-j, to destination D) is $N_{0i} + N_{iD}^{(j)}$, where N_{0i} is the number of hops that the packet traversed before it reached node i. While T_{max}, t_0, and N_{0i} can be stamped in the header of packets, r_{iD}[m] and thus $N_{iD}^{(j)}$ should be maintained via a distributed shortest-path algorithm or the underground localization mechanisms [39]. For example, as Bellman-Ford algorithm [40] is applied, $r_{iD}(t+1) = \min_{z \in S_i}(r_{iD}(t) + r_{iz})$. All the required operations and parameters are thus obtained for the proposed geographical protocol.

2.5 Environment-Aware Three-layer Protocol Stack

In this section, we present the main elements of the proposed protocol stack for oil reservoirs as follows:

1. The three-layer protocol stack.

2. Environment-aware functionalities of each protocol layer.

3. Communication constraints for transmission parameters (power control , reliability , average delay and delay variance constraints).

We design a three-layer protocol stack for WUSNs in oil reservoirs, as shown in Figure 7, rather than a conventional seven layers to save energy from protocol processing. For each layer, the essential functionalities are examined from the environment-aware perspective. The corresponding constraints of communication functions are also provided within this contribution.

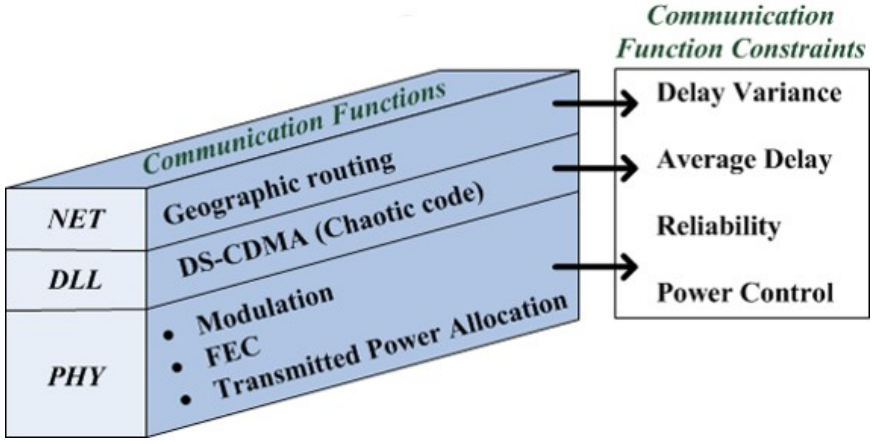

Figure 7: Three layer protocol stack for WUSNs in oil reservoirs.

2.6 Environment-Aware Cross-layer Optimization Framework

In this section, we integrate the communication functionalities mentioned above into a coherent mathematical framework and provide a unified foundation for cross-layer protocol design and control over WUSNs. The optimality of energy and throughput efficiency is reached based on application-dependent objective function. We summarize the main elements of the cross-layer framework as follows:

1. Adjust the corresponding transmission parameters regarding the environment-dependent parameters.

2. Multi-objective optimization for both optimal energy consumption and system throughput.

3. Application-driven objective optimization concurrently minimizes energy consumption and maximizes the system packet throughput with respect to the weight vector of the application.

This cross-layer framework enables the adjustment of transmission parameters with respect to four environment-dependent parameters, particularly to the measured temperature and the electrical conductivity. Moreover, it entails two-objective optimization with respect to the energy consumption and the network throughput, which are the two most critical factors for the energy-efficient and reliable communication. When confronting such multi-objective optimization, the Pareto optimal front provides the best solution sets that consist of non-dominated solutions, and thus gives the performance benchmarks. Furthermore, application-oriented WUSNs usually have their own purposes, such as sensing scalar data in harsh environments or monitoring objects with high data rate requirements accompanied by possible build-in energy harvesting. Thus, the application-driven objective optimization is proposed to jointly consider the energy savings and required throughput via the weighted sum method.

The optimality of energy and throughput efficiency is reached based on application-dependent objective function. In the following, we first deal with the two-objective optimizations (i.e., with respect to the energy consumption and the system throughput), which are the two most critical factors for the energy-efficient and reliable communication. While most of practical applications in WUSNs have their specific purposes, we jointly examine the energy and throughput issue via weighted sum methods.

With the proposed distributed functionalities over WUSNs, the energy consumption and the feasible throughput of link transmissions are our main concerns. Specifically, for link $i-j$, we aim to minimize the average energy per packet for successful arrival of a packet at the receiver and to maximize the average transmitted packet rate, characterized by the allowed link throughput under the finite link delay condition, expressed as

$$\begin{aligned} &\textbf{Minimize} \quad E_{ij} = L\left(P_{ij}/(R_{ij}(T,\sigma)R_C^{ij}) + 2E_{elec}^b\right); \\ &\textbf{Maximize} \quad Q_{ij}, \end{aligned} \tag{9}$$

where $P_{ij}/(R_{ij}(T,\sigma)R_C^{ij}) + 2E_{elec}^b$ accounts for the energy to transmit one bit from node i to node j. $P_{ij}/(R_{ij}(T,\sigma)R_C^{ij})$ characterizes the distance-dependent portion of consumed energy for bit transmission, while $E_{elec}^b = E_{elec}^{trans} = E_{elec}^{rec}$[J/bit] is for the distance-independent portion. E_{elec}^{trans} and E_{elec}^{rec} come from the needed energy per bit by the transmitter and receiver electronics (e.g., VCOs, PLLs, bias currents, etc.), respectively. When confronting such multi-objective optimizations, the Pareto optimal front [41] provides the best solution sets that consist of non-dominated solutions and thus provides the performance benchmarks. Figure 8 contains these optimal points for the transmission ranges between 1m to 15m and the packet length 20 Bytes. although (9) belongs to *min-max* type of optimization (i.e., considering minimizing the energy and maximizing the average packet rate concurrently), the Pareto fronts should trend from lower left to upper right, as verified in Figure 8. When the transmission range increases, so does the minimum feasible energy consumption. Moreover, in practice, the transmission range is usually in the middle distances (i.e., between 5m and 12m). Figure 8 shows that more possible Pareto points are available for such distances, so more transmission parameters can be optimized under the constraints for these suitable transmission ranges.

These applications provide the specific weight vector $\mathbf{w} = [w_1, w_2]^T$ with $w_1 > 0$ and $w_2 > 0$ for the energy savings and required throughput. In other words, the

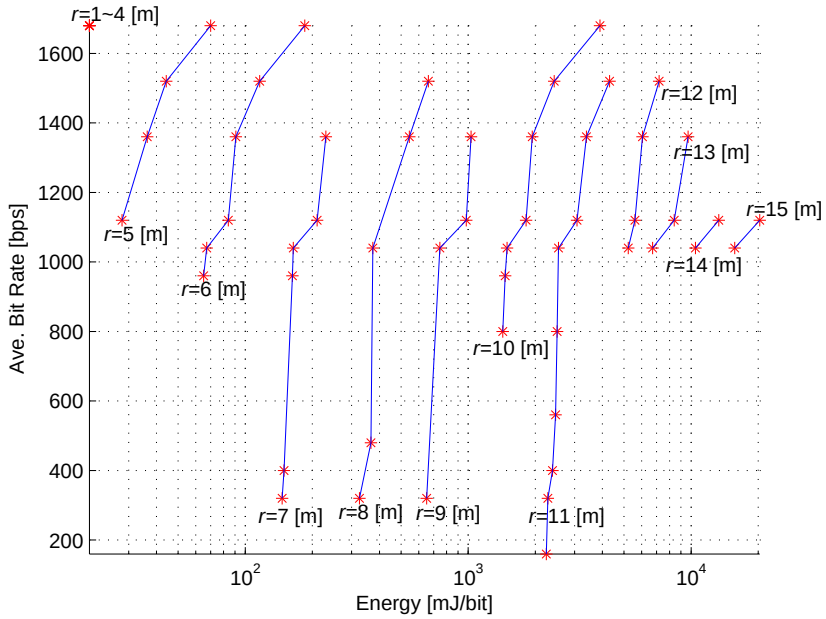

Figure 8: Pareto optimal front for two-objective optimizations with various transmission ranges.

previous two separate objective functions can be transformed into a single one (i.e., EaT for *Energy and Throughput*) via the vector and the entire optimization framework becomes

$$\begin{aligned}
\textbf{Find:} \quad & T,\ \sigma,\ j \in S_i \cap F_i^D,\ m_{ij} \in \mathcal{M},\ c_{ij} \in \mathcal{C}, \\
& P_{ij} \in [0, P_i^{max}],\ Q_{ij},\ l_{ij} \in \mathcal{L} \\
\textbf{Minimize} \quad & EaT_{ij}(T,\sigma) = \\
& w_1 L \left(P_{ij} / (R_{ij}(T,\sigma) R_C^{ij}) + 2E_{elec}^b \right) - w_2 Q_{ij} \\
\textbf{Subject to} \quad & power, link, average\ delay, dealy\ variance\ constraints.
\end{aligned} \tag{10}$$

The decision variables for node i are the operating temperature, the soil conductivity, the forwarder, the modulation technique, the channel coding scheme, the power level, the allowed link throughput, and the code length of DS-CDMA. Note that providing a satisfactory cross-layer design for practical underground settings requires that the designated protocol be environmentally aware. Specifically, it should be able to modify the corresponding transmission parameters with respect to the working

temperature and soil conductivity. our environmentally aware protocol yields such a capability, as explained in Section 2.7.

2.7 Distributed Environment-Aware Protocol (DEAP) Design

To empower practical applications in WUSNs, the functionalities of cross-layer framework should be distributively controlled and environmentally aware for the optimality. The main elements of DEAP as follows:

1. it senses two of the environment-dependent parameters (i.e., temperature and electrical conductivity).

2. it evaluates the relationship between chaotic code and link throughput.

3. it initiates a two-phase decision strategy.

4. it perfoms sensing and information exchange and a random access scheme for loss-tolerance.

We design DEAP so that it solves the application-driven objective optimization from the previous cross-layer framework. In particular, DEAP exploits the distributed power control via non-cooperative game theory to solve the near-far problem of the DS-CDMA scheme and evaluates the relationship between chaotic code length and link throughput. Optimal power is obtained when

$$p_i^* = \frac{B_{MI}(T,\sigma)}{a \ln 2} - \frac{N I_j \Gamma_i}{\varepsilon_{ij}(T,\sigma) g_{ij}}, \tag{11}$$

where $a = w_1/w_2$.

Also, we aim to comprehend the relationship between the link throughput and the code lengths of DS-CDMA. Specifically, from the optimization framework in Section 2.6, the explicit form of optimal throughput Q_{ij}^* can be obtained with respect to a specific length l_{ij} by Karush-Kuhn-Tucker (KKT) conditions [41]. Therefore,

the optimal link throughput Q_{ij}^*, regarding a specific DS-CDMA code length l_{ij} and channel coding scheme c_{ij} with rate R_C^{ij}, is

$$Q_{ij}^* = \begin{cases} \frac{R_{ij}(T,\sigma)R_C^{ij}}{L} - \frac{1}{\tau T_{ij}} & 0 \leq \tau \leq 0.5 \\ \frac{R_{ij}(T,\sigma)R_C^{ij}}{L} - \frac{1-A}{T_{ij}\sqrt{A}\left(1-\sqrt{A}\right)} & 0.5 < \tau < 1 \end{cases}, \tag{12}$$

where A equals to $\tau/(1-\tau)$.

It further utilizes a two-phase decision procedure to enable the favored geographical routing from its scalability and limited signaling overhead, which is highly suitable for oil reservoirs. Utilizing the distributed designs of cross-layer functionalities , we propose the distributed two-phase operation that follows the cross-layer framework in (10) as follows. Inherited from the per-node based geographical routing paradigm, the sender i (i.e., source or relay node) optimally decouples the cross-layer optimization (and thus routing decision) into two sub-problems and solves them sequentially as follows:

1. Minimize link metric EaT_{ij} with respect to power level P_{ij}, the allowed link throughput Q_{ij}, and the code length of DS-CDMA l_{ij} for each of its feasible next-hop neighbors and possible combinations of modulation and channel coding functionalities, i.e., $(j; m_{ij}; c_{ij})$.

2. Select the best next-hop j^* and the physical functionalities $(m_{ij}^*; c_{ij}^*)$ associated with the best link metric.

Rather than solving a complicated optimization problem for the best route to destination, a generic node i must sequentially deal with only two low-complexity subproblems without loss of optimality.

Algorithm 1 presents a space-search approach to solve the first sub-problem. It use Algorithm 2 to obtain three communication parameters (i.e., P_{ij}, Q_{ij}, and l_{ij}), via distributed power control, KKT optimality, and a golden section search [41].

Algorithm 1 Distributed Cross-layer Link Optimization

Require: i, j, r_{ij}, θ_{ij}

$EaT_{min} = \infty$ % Initialization
for $mod = 1 : |\mathcal{M}|$ **do** % Modulation cycle
  for $fec = 1 : |\mathcal{C}|$ **do** % FEC cycle
    Calculate r^j_{min} via tolerable end-to-end PER Φ^{e2e}_T
    $(EaT_{ij}, P, Q, l) \leftarrow$**Algorithm 2**$(r^j_{min}, NI_j, r_{ij}, \theta_{ij}, m_{ij}(mod), c_{ij}(fec))$
    if $EaT_{ij} < EaT_{min}$ **then**
      $EaT_{min} = EaT_{ij}$
      $(m, c, P, Q, l)^* = (m(mod), c(fec), P, Q, l)$
    end if
  end for
end for

Algorithm 2 Link Parameters

Require: r^j_{min}, NI_j, r, θ, m, c
Ensure: EaT^*, P^*, Q^*, l^*

Get $EaT(l)$ in (10) via global maximum, optimal link throughput $(r^j_{min}, NI_j, r, \theta, m, c)$
$l^* \leftarrow$**GoldenSection**$(EaT(l), K_l)$ % K_l:Reduction steps
Calculate P^*, Q^*, EaT^* by l^*, cross-layer optimization, global maximum, and optimal link throughput

2.8 Performance Evaluation

We compare the performance of the proposed DEAP in Section 2.7 with traditional layered protocol solutions (i.e., individual communication functionalities do not share information and operate in separate layers). Simulation results confirm that DEAP achieves remarkable energy savings as well as a high throughput gain in a distributed manner, favored by practical implementation in WUSNs. Simulation results show that DEAP outperforms the layered protocol solutions with 50% energy savings and a 6 dB throughput gain. Moreover, beyond the centralized cross-layer designs, our solution resorts to two-phase per-node-based decisions requiring only one-hop neighbor information and has low computation complexity. Thus, by establishing reliable and efficient transmissions in challenged underground environments, we have provided a

distributed cross-layer design for MI communication in WUSNs. In the following subsections, we first evaluate the performance of link transmissions and then examine the end-to-end communication.

2.8.1 Link Transmissions

Considering the interactions among physical layer functionalities (i.e., modulation techniques, channel coding schemes, and power control design), energy consumption per bit, transmit power, and average bit rate are evaluated with respect to various MI transmission ranges. A comparison for DEAP is carried out with two fixed modulation/FEC combinations, i.e., BPSK/No FEC and BFSK/BCH(63,57,1), and one cross-layer design following the framework that provides centralized power control by (8). The QoS requirements for the transmissions are set as follows: an expected hop delay 0.9 s, the outage delay probability of less than 0.8, and a maximal tolerable PER of 10^{-4} with a packet length of 20 Bytes. Also, the weight vector from application is set at $w_1 = 0.7$ for energy consumption and $w_2 = 0.3$ for link throughput, and the high interference scenario is 0.02 W noise in addition to MAI power level.

In Figures 9 and 10, the transmitted energy and power of fixed modulation/FEC combinations for a successfully decoded payload bit at the receiver are always higher than the cross-layer designs. Furthermore, regarding the cross-layer solutions, as centralized power control assumes more available network information (i.e., the transmitted power level of both one- and two-hop neighbors), it consumes less energy at a lower power level than the proposed distributed solution (i.e., DEAP). However, such assumption can only be achieved theoretically via a great deal of control signaling exchanges, which is impossible in practical energy-limited scenarios such as WUSNs.

DEAP, however, permits the only information required by the transmitter to become received noise plus the MAI power level at the receiver (i.e., information from one-hop neighbors). The energy it consumes is close to that of the centralized

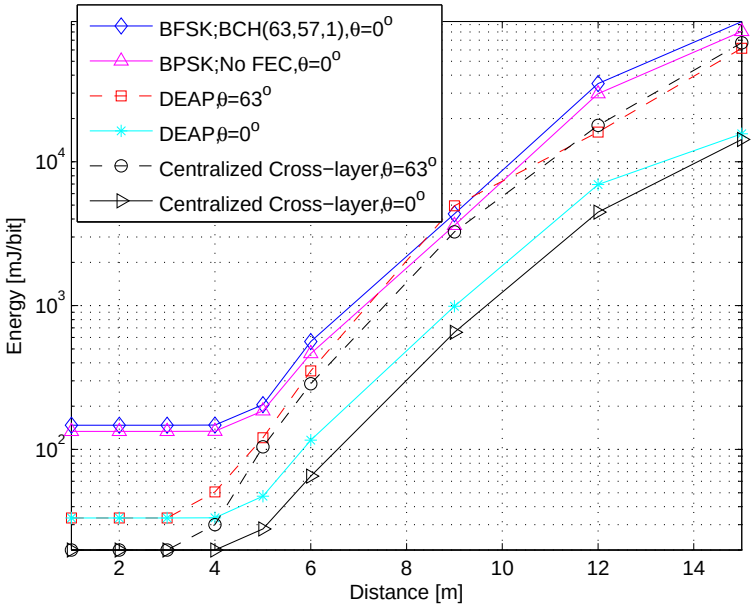

Figure 9: Energy per bit for the centralized cross-layer solution, the cross-layer DEAP, and two fixed modulation/FEC combinations.

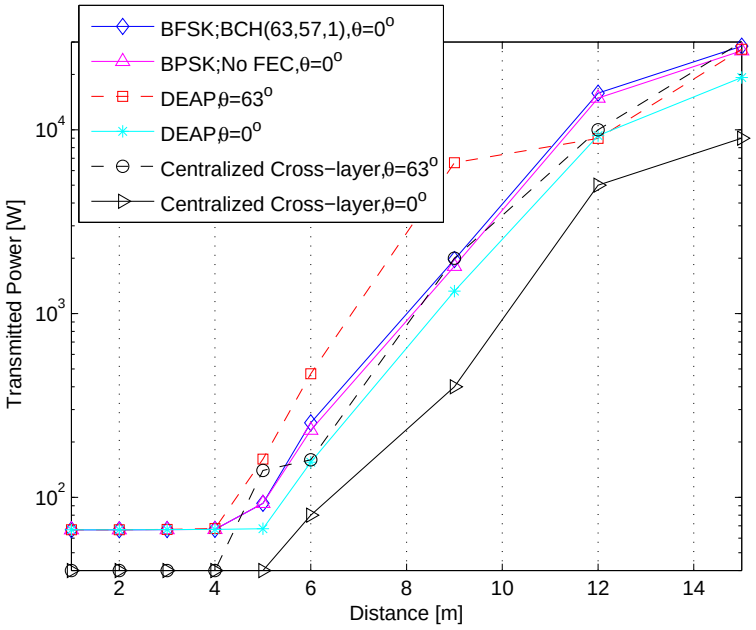

Figure 10: Transmitted power for the centralized cross-layer solution, the cross-layer DEAP, and two fixed modulation/FEC combinations.

design and attains the same level under long transmission distances. The impact of coil angle misalignment is also presented for the cross-layer design, but the layered

schemes cannot obtain the solution with practical applications. Under this setting, the consumed energy of DEAP and the centralized designs are almost the same under short transmission distances.

Figure 11 further provides the achievable average bit rates with respect to layered solutions (i.e., BFSK;BCH$(63, 57, 1)$ and BPSK;No FEC) and cross-layer solutions (i.e., Centralized Cross-layer and DEAP). The cross-layer design is favored because its bit rate is higher than that of the layered solution. The proposed DEAP also outperforms the centralized scheme for nearly all transmission distances and allows a much higher bit rate, especially under middle transmission ranges. After all, our distributed solution is not confined by the severe power constraints from two-hop neighbors as the centralized solution, which always considers the worst-case scenario. Instead, DEAP employs a non-cooperative game to distributively control the transmitted power of each sensor, thus enjoying higher throughput.

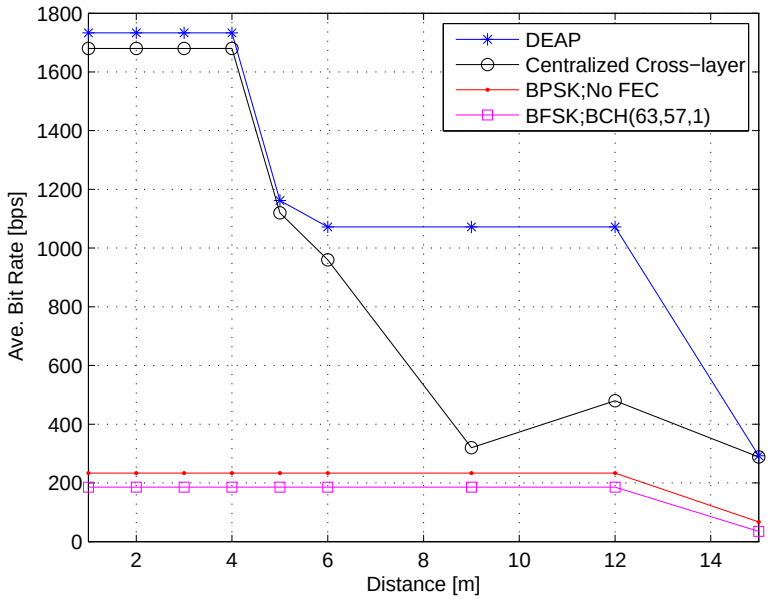

Figure 11: Average bit rate for the centralized cross-layer solution, the cross-layer DEAP, and two fixed modulation/FEC combinations.

To sum up, DEAP not only consumes nearly the same level of energy as the

centralized design but also attains remarkable link throughput over bandwidth-limited MI communication channels. As discussed previously, It also provides much lower computation complexity for great practicability in WUSNs.

2.8.2 End-to-End Data Flow

This section examines the interactions between MAC and routing functionalities via end-to-end energy and throughput performance. We build two layered protocol architectures (i.e., Protocols 1 and 2) for a comparison with our proposed design. The detail configurations follow:

- [**Protocol 1**] is built of Geographical Routing, DS-CDMA, Distributed Power Control, and MI Channel Model.

  This protocol configuration employs previously proposed distributed power control and a DS-CDMA (via chaotic code) scheme for physical and MAC layers, respectively. The routing algorithm reduces the distance from the transmitter to the destination by selecting the next closet node to the destination as the next hop.

- [**Protocol 2**] is built of TPL-Based Greedy Routing, DS-CDMA, Distributed Power Control and an MI Channel Model.

  This protocol configuration is similar to protocol 1 configuration, except that the routing decision is based on the channel quality of the transmitter with its neighbors. The channel quality is measured in terms of the transmitted power level (TPL) for successfully bit decoding at the receiver. The node that most strongly minimizes the required transmitted power is selected as the next hop.

While the above layered protocol 1 and protocol 2 apply previously proposed functionalities to some extent, they consider only their related layers without information sharing but with reasonable assumptions for the other layers. These architectures

along with our distributed design, are evaluated in a 3D underground cube with the volume $10 \times 10 \times 10$ m^3. A variable number of sensors (from 10 to 50) are uniformly deployed in such an area, and three source-destination pairs are randomly selected among them. To establish more practical and reasonable scenarios, we restrict the maximum transmission range of a transceiver pair to 12 m, suggested by the previous results, as it costs too much energy and gains little throughput under too long distances.

Figures 12 and 13 show normalized energy and a successfully received packet rate for end-to-end data flow. As the number of sensors increases, so does the number of routes that provide better end-to-end performance, leading to greater cooperative diversity. Such advantages are the result of less energy consumption and more achievable throughput in all three protocols. Specifically, without exchanging information among the variety of layer functionalities and adopting layered approach, protocol 1 selects the set of nodes that sequentially move closest to the destination, mainly concerning the geographical progression and providing the worst performance. As for protocol 2, it minimizes the required transmitted power along the multi-hop transportation, which trades more link transmissions and thus longer routes for better energy savings. Yielding the best energy and throughput performance concurrently, our schemes surpass both protocols with at least 50% energy savings and a 6 dB throughput gain, the result of jointly optimizing the communication functionalities of different layers, producing synergy that enhance end-to-end system performance. Because of its outstanding energy and spectral efficiencies accompanied by low computational complexity, the proposed DEAP strongly suits underground environments. Therefore, we introduce a new paradigm for reliable and efficient MI communication and offer a novel avenue towards distributed cross-layer design in WUSNs.

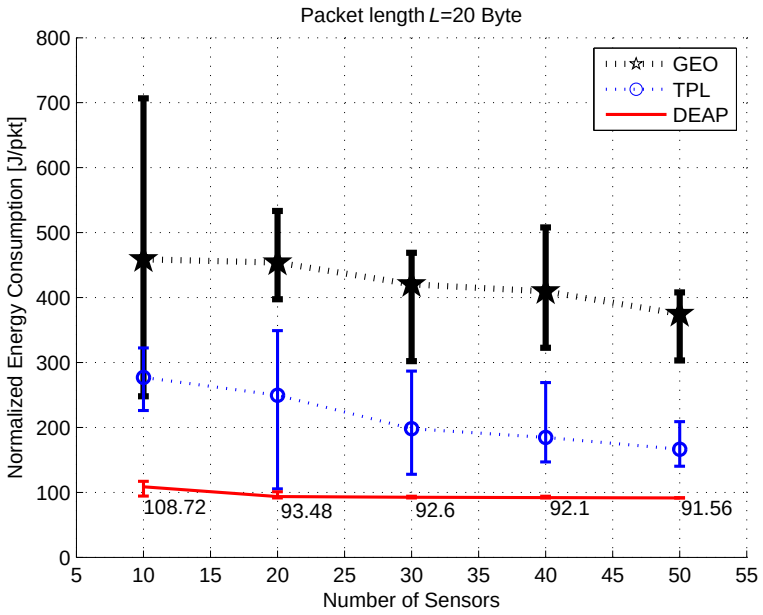

Figure 12: Normalized energy consumption for the cross-layer DEAP and the layered framework of protocols 1 and 2.

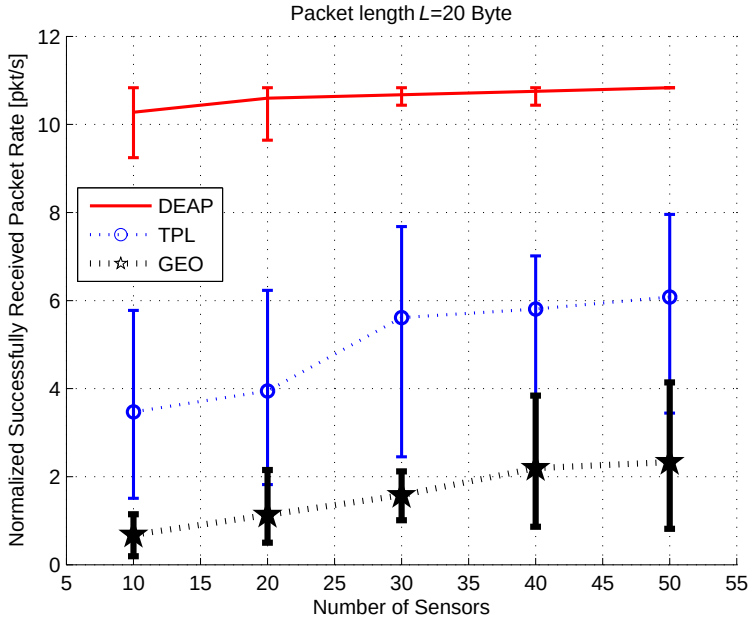

Figure 13: Normalized successfully received packet rate for the cross-layer DEAP and the layered framework of protocols 1 and 2.

2.9 Highlights

In this chapter, we developed the distributed environment-aware protocol (DEAP), a fully distributed cross-layer protocol framework for MI-based WUSNs. Satisfying the

QoS requirements of diverse applications it achieves optimal energy consumption and high throughput efficiency with low computational complexity. We address the interaction of key underground communication functionalities and a distributed cross-layer design and ensure that DEAP efficiently utilizes the bandwidth-limited MI channels in WUSNs. Its designated distributed power control enables the DS-CDMA mechanism via chaotic codes for reliable link transmissions with limited available network information. In addition, it guarantees statistical delay constraints and achieves optimal link throughput by solving the framework with respect to the given code length. Building on these results, we employ a two-phase decision strategy to sequentially tackle two sub-problems for optimal feasible energy savings and throughput gain with low computation complexity for great practicability. A performance evaluation confirms that the DEAP provides high system throughput and very low energy consumption within a guaranteed delay. Simulation results also confirm its remarkable energy savings and high throughput gain in a distributed manner, favored by practical implementation in WUSNs, and that it outperforms layered protocol solutions by 50% in energy savings and 6 dB in throughput gain.

These outstanding energy and spectral efficiencies accompanied with low computational complexity confirm that the proposed DEAP strongly suits underground environments. Therefore, we introduce a new paradigm for reliable and efficient MI communication and offer a novel avenue towards distributed cross-layer design in WUSNs.

CHAPTER III

MI-BASED LOCALIZATION FOR WUSN IN HYDRAULIC FRACTURES AND OIL RESERVOIRS

In this chapter, we introduce a MI-based localization for wireless underground sensor networks in hydraulic fractures and oil reservoirs. We develop an MI-based localization that accurately and efficiently locates randomly-deployed sensors in underground environments by leveraging the multi-path fading free nature of MI signals as published in [42, 43]. The motivation for this work is provided in Section 3.1, and related work is discussed in Section 3.2. The system model is introduced in Section 3.3, and the MI-based localization framework for WUSNs in oil reservoir environment is introduced in Section 3.4. Section 3.5 presents fast initial positioning from Alternating Direction Augmented Lagrangian Method (ADM), and Section 3.6 discusses fine-grained Positioning from Conjugate Gradient Algorithm (CGA). Section 3.7 evaluates our MI-based localization framework, and Section 3.8 concludes.

3.1 Motivation

Most applications of WUSNs, such as the monitoring of mine, hydraulic fracture, and oil reservoirs, are location dependent, so they require precise sensor positions. However, classical localization solutions based on the propagation properties of electromagnetic waves do not function well in underground environments because of the extremely short communication ranges, highly unreliable channel conditions, and large antenna sizes. Thus, we develop an MI-based localization strategy for WUSNs

in hydraulic fracture and oil reservoirs. We propose a novel MI-based localization solution, which utilizes the promising features of MI channel and the byproduct of MI-based communication, that is, received magnetic field strength (RMFS), to guarantee the accuracy, simplicity, and convenience of the localization strategy. Our solution jointly applies weighted maximum likelihood estimation (WMLE), semi-definite programming (SDP) relaxation, the alternating direction augmented Lagrangian method (ADM), and the conjugate gradient algorithm (CGA) with regards to an MI-based communication channel to achieve high positioning accuracy of the wireless sensor devices (FracBots) in oil reservoirs, while maintaining high computational efficiency. Using RMFS, we determine a set of distances from the measured respective RMFSs with respect to two anchors. Then, we process the set of distances through an ordered sequence of algorithms, namely ADM and CGA to generate the accurate localization of sensor nodes in underground oil reservoirs.

The main elements of our MI-based localization framework follow:

1. RMFS measurements for designing localization in underground oil reservoirs.
2. A localization framework for WUSNs in underground oil reservoirs.
3. Fast initial positioning by the aternating direction augmented lagrangian method (ADM).
4. Fine-grained positioning from the conjugate gradient algorithm (CGA).

Figure 14 shows the MI-based localization system design with our contributions. First, we examine MI-based communication to obtain the distance estimation from received magnetic field strengths (RMFSs) through the developed channel models. Second, we establish the localization framework as the problem formulation of joint weighted maximum likelihood estimation (WMLE) and semidefinite programming (SDP) relaxation for accurate sensor positioning from noisy distance estimations.

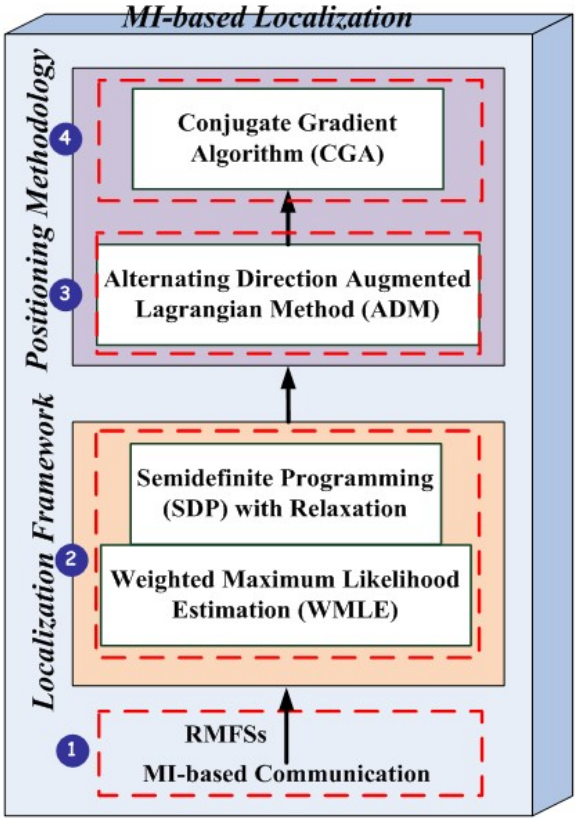

Figure 14: MI-based localization system design.

Third, we propose the efficient initial positioning from the fast algorithm, ADM, to provide rough but useful results of sensor locations, and then from the initial results, we add the fine-grained positioning from a powerful CGA to enhance localization accuracy in a time-efficient manner.

3.2 Related Work

The majority of the localization algorithms focus on terrestrial wireless sensor networks. One study [44] provides an overview of localization strategies with the performance evaluation of several existing localization systems and proposed three prominent approaches: multidimensional scaling (MDS), simulated annealing (SA), and semidefinite programming (SDP), respectively. Then a study in [45], building on

MDS approach, proposed a distributed weighted MDS (dwMDS) that allows a distributed implementation with minimal required communication, accounts for prior location information, and uses a weighted cost function that yields heavier weights for accurate pair-wise measurements. The authors of [46]introduce a collaborative localization approach that uses MDS as an initialization method in which maximum likelihood estimation further improves the initial results with its fast convergence. However, the drawback of MDS is that it is computationally complex and requires a large amount of information. In addition, the poor noise resistance of MDS also requires an additional design, limiting its practical use. To address the distance measurement errors in centralized SA-based algorithms, a study in [47] provided an, the analysis of flip ambiguities and the a robust localization approach. Unfortunately, the heuristic-based algorithms mentioned above introduce several critical issues such as the convergence rates, the feasibility to the optimal objective values, signaling exchange overhead, and others.

The authors of [48] employed a fast convex relaxation method for distributed localization implementation that largely depends on the computation capacity of network devices to locally capture the optimal gradient direction of the objective via information broadcasting, which is impossible for WUSNs, whose sensors capabilities and the number of anchors are often limited. Then a study in [49] applied the convex relaxation technique to transform the non-convex problem into SDP relaxation for localization with high noisy distance measurements. Instead of employing SDP, the authors of [50] proposed another convex relaxation technique, namely the sum of squares (SoS) method, which provides highly accurate localization performance at the cost of high computational complexity. Rather than focusing on convex relaxation, the author of [51] proposed a polynomial-time non-convex optimization for the initial node locations sufficient to recover true locations. The above localization solutions, unfortunately, suffer from poor convergence speed for large-scale networks

because they do not explore the inherited optimization structure, but simply adopt optimization packages (e.g., SeDuMi in [49]) for their cumbersome problem formulations. Thus, they cannot be deployed easily on a sensor with limited resources, especially WUSNs.

A fast algorithm, called alternating direction augmented Lagrangian method (ADM), has recently been used to provide a powerful leverage for the algorithm analysis resulted from convex relaxation. A study in [52] used ADM for a distributed localization implementation from edge-based convex programs in large-scale networks. However, the approach in this study depends primarily on the high computation capacity of network devices to locally solve a convex relaxation problem via optimization toolboxes, which is impossible for WUSNs, which often contain limited sensor capabilities. Moreover, because of one-step positioning by ADM, performance refinements are extremely difficult. In this case, to improve the localization accuracy, sensor nodes must have the capacity to execute computation-intensive software packages iteratively. This task, however,is impossible task because of size and computational limitations posed by the sensor processor.

3.3 System Model

In hydraulic fracture, it is assumed the FracBots are randomly-deployed and two anchors exist as reference points for localization. An MI communication link is formed by the induction between the primary and the secondary coils. Hence, the anchors are large dipole antennas inside the drilling well that communicate with the FracBots. Data from FracBots can be sent back to the anchors by multi-hop communication. The network model is abstracted mathematically as follows. Without loss of generality, WUSNs consist of N Fracbots (sensors) with random positions denoted by set $\{x_i \in \mathbb{R}^2 : 1 \leq i \leq N\}$ and two anchors with known positions denoted by set $\{a_k \in \mathbb{R}^2 : 1 \leq k \leq K\}$. These anchor locations provide reference points for

other sensors. In addition, through the establishment of channel models for MI-based communication, two types of information are available when designing localization systems. In particular, as shown in Figure 15, the channel models provide estimated distances among sensors, that is, $\hat{d}_{ij}$, $1 \leq i \leq N$ and $j \in NH_i$ where NH_i denote the neighbor set of sensor i, and between anchors and sensors, that is, $\hat{d}_{ik}$, $1 \leq i \leq N$ and $1 \leq k \leq K$, from the respective RMFS. Note that while anchors often support a more flexible design that enables communication in much larger transmission ranges, it is assumed that direct communication links between each anchor to every sensor exist. Therefore, the localization system aims to provide unknown sensor locations according to the given anchor locations and estimated distances. This system will be implemented in a local or remote computing control center, that connects to a small number of designated anchors.

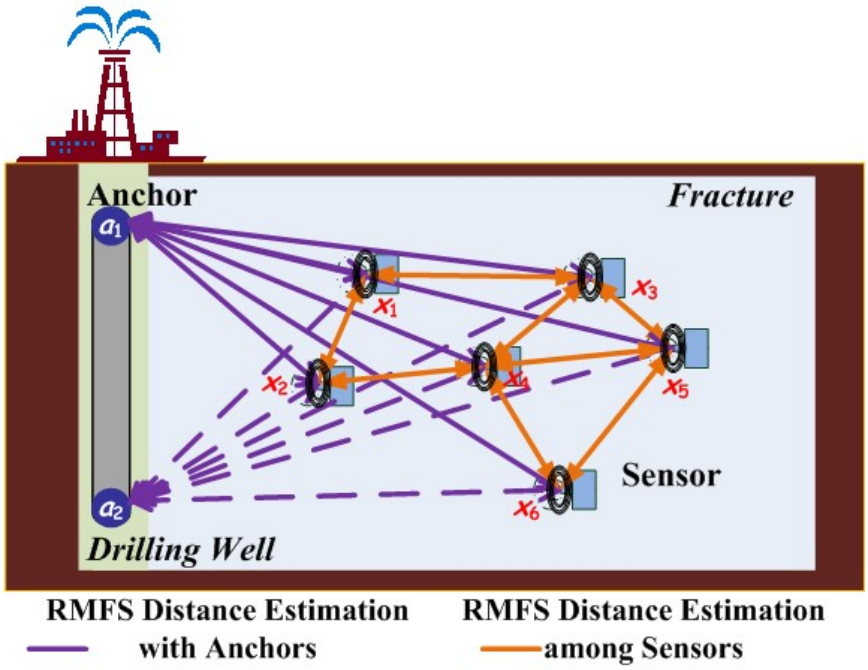

Figure 15: Randomly-deployed WUSNs (FracBots) in oil reservoir.

3.4 MI-Based Localization Framework

In this section, we first introduce MI channel modeling and then formulate the MI-based localization framework through a designated cost function and SDP relaxation. The entire framework of the proposed underground localization is illustrated in Figure 14.

3.4.1 MI-Channel Model and Node-to-Node Distance Measurement

Through MI communication, data information is carried by a time varying magnetic field generated by a modulated sinusoid current along an MI coil antenna at the transmitter. The receiver retrieves the information by demodulating the induced current along the receiving coil antenna. Since the magnetic field does not exhibit multi-path behavior, given the RMFS, the distance between the transmitter and the receiver can be uniquely estimated with regards to AWGN channels in MI-based communication. Specifically, a previous study [16] was able to apply transformer circuit models to accurately obtain the path loss of MI-based communication, thus providing required estimated distances for localization systems. From MI channels [16], we formulate

$$10^{\frac{P_r}{10}} = 10^{\frac{P_t - L_{MI}}{10}} + N, \tag{13}$$

where P_r [dBm] and P_t [dbm] are the received power and the transmission power, respectively, L_{MI} [dB] is the path loss in dB, N is a zero mean Gaussian distributed random variable with standard deviation ϕ that accounts for the background noise. Given the RMFS measurement, P_{ij}, between a transmitter i and a receiver j, a maximum likelihood estimation of the distance, d_{ij}, between the transmitter and the receiver can be determined based on parameters such as coil dimensions, coil orientations, and transmission medium conductivity.

Two major advantages of the MI-based distance estimation method over the conventional electromagnetic (EM)-based solution are summarized as follows:

1. **Resistant to the multi-path effect**: Since the magnetic field does not exhibit multi-path behavior, given the received MI signal strength, the distance between the receiver and the transmitter can be uniquely identified. Unlike the EM-based distance measurement, This measurement consists of a single value of the received EM signal strength that may correspond to multiple distance estimations.

2. **Insensitivity to environmental condition changes**: The RMFS is not affected by dynamic environmental parameters in underground environments such as humidity, temperature, and pressure. Therefore, the RMFS-based localization algorithm is high accurate regardless of how dramatically these environmental parameters change.

3.4.2 RMFS Measurements for Designing Localization in Underground Oil Reservoirs

The main elements used in RMFS measurements for designing localization in oil reservoirs are as follows:

1. Temperature, electrical permittivity and magnetic permeability.

2. Estimated distances from RMFS measurements via the channel model.

As MI-based communication enjoys unique multi-path and fading free propagation properties, we derive the distance estimations between two coils from RMFSs. In particular, as MI-based communication will be affected by few environmental parameters, the path-losses and thus RMFS measurements are a function of operating temperature T, the electrical permittivity of medium ϵ, and the magnetic permeability of medium μ. The distance between the transmitter and receiver coils can be uniquely identified from the RMFS measurements. We apply this estimation methodology to obtain the estimated distances between pair-wise sensors $\hat{d}_{ij}$ and between

sensors and anchors $\hat{d}_{ik}$. Transmission distance d can be uniquely estimated from the MI path loss model [16] as $\hat{d}$ in Eq. (14),

$$\hat{d} = \arg\left\{ d \left| (10^{\frac{P_t - \hat{\theta}_{ML}}{10}} - 1) = \frac{16 R_0^t(T) R_0^r(T) d^3}{\omega^2 \mu^2(T) N_t N_r a_t^3 a_r^3 G^2 \left(\sigma(T,\varepsilon), \omega, d\right)} \right.\right\}. \tag{14}$$

In short, the great novelty of the proposed MI-based localization approach stems from its use of the unique multi-path and fading free propagation properties of MI-based signals; as a result, it is an accurate, simple, and convenient localization algorithm.

3.4.3 Underground Localization: Error Function and SDP

Based on the RMFS-based distance estimation strategy, we formulate the localization framework via an error function and SDP relaxation, the purpose of which is to minimize errors between estimated and actual positions. In other words, we aim to find sensor positions that minimize the designated error function given the estimated distances in Eq. (14). Towards this end, we define the estimation errors in our localization system as

$$\begin{array}{rcl} \epsilon_{ij} & = & \|x_i - x_j\|^2 - \hat{d}_{ij}^2 \\ \epsilon_{ik} & = & \|x_i - a_k\|^2 - \hat{d}_{ik}^2 \end{array}, \tag{15}$$

where $\{x_i\}_{1 \le i \le N}$ is the set of sensor positions, $\{a_k\}_{1 \le k \le K}$ is the set of anchor positions, and $\hat{d}_{ij}$ ($\hat{d}_{ik}$) are estimated node-to-node distances, obtained from Eq. (14).

Given $X := [x_1, \ldots, x_N]$, we minimize error function $f(X)$ to estimate sensor positions (i.e., $\hat{X}$) as follows. Specifically, we have

$$\begin{array}{rcl} \hat{X} & = & \arg\min\limits_{X} f(X) \\ & := & \arg\min\limits_{X} \sum\limits_{\{(i,j):1 \le i \le N, j \in NH_i\}} (\|x_i - x_j\|^2 - \hat{d}_{ij}^2)^2 \\ & & + \sum\limits_{\{(i,k):1 \le i \le N, 1 \le k \le K\}} (\|x_i - a_k\|^2 - \hat{d}_{ik}^2)^2, \end{array} \tag{16}$$

where the first portion of $f(X)$ stems from the estimation mismatch among sensors and the second portion of $f(X)$ from the mismatch among sensors and anchors. Eq.

(16) implies that error function $f(X)$, seen as the L_2 norm of errors from a given estimate of X, is a fourth-degree polynomial function.

Based on the error function minimization in Eq. (16), we apply SDP relaxation to obtain the proposed underground localization framework:

$$\begin{aligned} \min \quad & \sum_{\{(i,j):1\leq i\leq N, j\in NH_i\}} \epsilon_{ij}^2 + \sum_{\{(i,k):1\leq i\leq N, 1\leq k\leq K\}} \epsilon_{ik}^2 \\ \text{s.t.} \quad & (0; e_i - e_j)^T Z (0; e_i - e_j) = \epsilon_{ij} + \hat{d}_{ij}^2 \quad \forall (i,j) \\ & (a_k; -e_i)^T Z (a_k; -e_i) = \epsilon_{ik} + \hat{d}_{ik}^2 \quad \forall (i,k) \\ & Z = \begin{pmatrix} I & X \\ X^T & Y \end{pmatrix} \succeq 0 \end{aligned} \tag{17}$$

where the relaxation indicates that the last equation relaxes from $Y = X^T X$ to $Y \succeq X^T X$, and I denotes the identity matrix. As a result of the SDP relaxation of $Y \succeq X^T X$, the non-convex optimization problem defined in Eq. (17) becomes a convex one, which is easier to solve. The high-rank property of SDP relaxation [53], nevertheless, lifts the obtained solution into a higher dimensional space, that is, higher than $\mathbb{R}^2$ in Eq. (17), resulting in smaller estimation errors which, in turn, necessitates the design of a rounding operation that obtains the solution with accurate dimensionality, (i.e., $\mathbb{R}^2$).

In the following sections, we first propose a fast convergent scheme for the problem in Eq. (17) through the ADM, discussed in Section 3.5, which has controllable computation complexity. Then we propose a time-efficient search algorithm through the CGA, explained in Section 3.6, which yields a highly accurate localization solution within the $\mathbb{R}^2$ for randomly-deployed sensors in WUSNs.

3.5 Fast Initial Positioning from the Alternating Direction Augmented Lagrangian Method (ADM)

This section presents the key steps of fast initial positioning from ADM:

1. Utilize the parameters given by the MI-based localization framework for the design of fast initial positioning.

2. Formulate primal and dual variables that enable the fast algorithm, ADM, for the joint WMLE and SDP relaxation problem.

3. Derive the updating rules of primal and dual variables to obtain initial sensor locations through a highly time-efficient manner.

When the number of constraints of the SDP problem approaches the order of unknown parameters, interior point methods [41], as conventional solutions to the SDP problem, become impractical with regard to both computation time and storage at each iteration. By contrast, ADM [54], a fast first-order method, requires much less computation and storage and could further take advantage of its problematic structure such as sparsity. Thus, it is more suitable and sometimes the only practical choice for solving large-scale SDPs. In the following, we first examine a specific SDP form of a localization problem. We then propose a fast initial positioning through ADM for the SDP problem. Finally, we analyze the convergence rate to verify the fast convergence of the proposed solution.

3.5.1 Underground Localization SDP Problem

To effectively utilize fast-convergent ADM for solving the localization SDP problem, we need to transform the original SDP in Eq. (17). Specifically, we first reformulate Eq. (17) into a matrix form as follows:

$$\begin{aligned} \min \quad & \epsilon^T \epsilon \\ \text{s.t.} \quad & \langle A_{ij}, Z \rangle = \epsilon_{ij} + \hat{d}_{ij}^2 \ \forall (i,j) \\ & \langle \bar{A}_{ik}, Z \rangle = \epsilon_{ik} + \hat{d}_{ik}^2 \ \forall (i,k) \\ & Z \succeq 0 \end{aligned} , \tag{18}$$

where $\epsilon := [\epsilon_{ij}]^T$ denotes the error vector with transpose operation T, and

$$\begin{aligned} A_{ij} &:= \begin{pmatrix} 0 \\ e_i - e_j \end{pmatrix} \begin{pmatrix} 0 & e_i - e_j \end{pmatrix}, \\ \bar{A}_{ik} &:= \begin{pmatrix} a_k \\ -e_i \end{pmatrix} \begin{pmatrix} a_k & -e_i \end{pmatrix} \end{aligned} \tag{19}$$

denote two auxiliary matrices with respect to the constraints presented in Eq. (17). Like the interpretation of the original SDP, in Eq. (18), that of the objective function aims to minimize mismatch errors from location estimation, and the constraint functions indicate two causes of estimation mismatch as well as SDP relaxation. Furthermore, we combine the constraints of A_{ij} and $\bar{A}_{ik}$ in Eq. (18) into a single constraint as follows:

$$\begin{aligned} A(Z) &:= [\langle A_{ij}, Z\rangle, \langle \bar{A}_{ik}, Z\rangle]^T \\ &= [\epsilon_{ij} + \hat{d}_{ij}^2, \epsilon_{ik} + \hat{d}_{ik}^2]^T := b(\epsilon) \end{aligned} \tag{20}$$

where $A(Z)$ is the linear map of Z. Finally, we formulate the underground localization problem as a specific SDP that can be further solved by ADM [54] shown in Section 3.6, as follows:

$$\begin{aligned} \min \quad & \epsilon^T \epsilon \\ \text{s.t.} \quad & A(Z) = b(\epsilon) \ \cdot \\ & Z \succeq 0 \end{aligned} \tag{21}$$

To optimize sensor localization, we assume the following for the for localization problem throughout this work: that optimal solution exists for localization in Eq. (17); that is, matrices $\{A_{ij}, \bar{A}_{ik}\}_{i,j,k}$ have full row rank and the Slater condition [53] holds for Eq. (21).

3.5.2 Fast Initial Positioning Through ADM for Underground Localization

To solve the problem in Eq. (21), we exploit the widely-adopted ADM framework [54] for solving SDP problems. However, the framework in [54] cannot be directly applied to our special underground localization formulation (i.e., a specific SDP problem in Eq. (21)) without a further detailed examination and derivations. Specifically, first while the analysis in [54] works on the dual problem of the standard SDP, the considered objective function in [54] is linear. However, ours is nonlinear (quadratic) and thus complicates the primal iteration of ϵ as indicated by Eq. (23). Second, the constraint related to the semi-definiteness condition [54] differs from ours. More specifically, in [54], a semi-definite matrix is added to the output of the adjoint operator of linear map A^* (i.e., addition operations), where $A^*(y) := \sum_i(\sum_j y_i^j A_{ij} + \sum_k y_i^k \bar{A}_{ik})$ from Eq. (20). In our work, however, the semi-definite matrix Z is the input of linear map A (i.e., functional operations), which entails involved iterations of primal Z and dual Λ as in Eqs. (24) and (25), respectively. In the following, we present a rigorous and fast-convergent positioning algorithm based on ADM [54] with the specific SDP formulation in Eq. (21).

First, the transformation from the SDP formulation in Eq. (21) to an augmented Lagrangian function, which is standard [54, 55] can be derived as $L_\mu(Z, \epsilon, \Lambda) = \epsilon^T\epsilon + \langle \Lambda, A(Z) - b(\epsilon)\rangle + \frac{1}{2\mu}\|A(Z) - b(\epsilon)\|_F^2$ where $\mu > 0$ is related to the penalty parameter and Λ is the dual variable. Next, ADM works with L_μ to yield the updating rules of primal and dual variables. Specifically, we solve the problem of $\min_{\epsilon, Z\succeq 0} L_\mu(Z, \epsilon, \Lambda)$ on the m^{th} iteration for Z^{m+1} and ϵ^{m+1}, starting from dual $\Lambda^0 = \mathbf{0}$. We then update the dual variable Λ_{m+1} by $\Lambda^{m+1} = \Lambda^m + \frac{A(Z^{m+1}) - b(\epsilon^{m+1})}{\mu}$. Moreover, inspired by [55], to avoid the time-consuming operation of jointly minimizing L_μ with primal Z and ϵ, we minimize the augmented Lagrangian function L_μ for Z and ϵ iteratively. Specifically,

the updating rules for primal and dual variables are

$$\epsilon^{m+1} := \arg\min_{\epsilon} L_\mu(Z^m, \epsilon, \Lambda^m); \tag{22a}$$

$$Z^{m+1} := \arg\min_{Z\succeq 0} L_\mu(Z, \epsilon^{m+1}, \Lambda^m); \tag{22b}$$

$$\Lambda^{m+1} := \Lambda^m + \frac{1}{\mu}[A(Z^{m+1}) - b(\epsilon^{m+1})]. \tag{22c}$$

Note that as similar convergence results and numerical performance can be yielded through any order [54, 55], the order of above Eqs. (22a)-(22c) is not relevant. Upon this stage, the proposed SDP relaxation in Eq. (17) is completely solved by the time-efficient updating approach of Eqs. (22a)-(22c).

To further ease the computational complexity of the updating rules [55], we exploit several mathematical operations for primal variables ϵ and Z. More specifically, we apply (i) first-order optimality [41] to Eq. (22a) for an explicit solution and (ii) eigenvalue decomposition to ease the minimization problem in Eq. (22b). First, we derive the optimality condition for ϵ^{m+1} in Eq. (22a) as $\nabla_\epsilon L_\mu(Z^m, \epsilon^{m+1}, \Lambda^m) = 2\epsilon^{m+1} - \Lambda^m - \frac{1}{\mu}\left[A(Z^m) - b(\epsilon^{m+1})\right] = 0$. Thus, we obtain the updating rule of primal variable $\epsilon^{m+1} = \epsilon(Z^m, \Lambda^m)$ as

$$\epsilon(Z, \Lambda) = -(2\mu + 1)^{-1}[D - A(Z) - \mu\Lambda] \tag{23}$$

where $b(\epsilon) = \epsilon + D$ from Eq. (20). As mentioned, Eq. (23) is re-derived because of the nonlinear objective function of our specific SDP formulation in Eq. (21).

Next, regarding Z^{m+1} in Eq. (22b), we rearrange the terms of $L_\mu(Z, \epsilon^{m+1}, \Lambda^m)$ and verify that Eq. (22b) is equivalent to $\min_Z \|A(Z) - V^{m+1}\|_F^2, Z \succeq 0$ where $V^{m+1} := V(\epsilon^{m+1}, \Lambda^m)$ and $V(\epsilon, \Lambda) := b(\epsilon) - \mu\Lambda$. Note that the equivalent problem here differs from that in [55] because of the differences in their semi-definiteness conditions. Also, if we assume that $U^{m+1} = (A^*A)^{-1}A^*(V^{m+1})$ with adjoint operator A^*, and that A^*A is invertible. By the eigenvalue decomposition, we thus obtain the explicit solution of the updating rule of primal variable Z^{m+1} as

$$Z^{m+1} = U_\dagger^{m+1} = P_\dagger \Sigma_+ P_\dagger^T \tag{24}$$

where $P\Sigma P^T$ is the spectral decomposition of matrix U^{m+1} with nonnegative Σ_+ and negative Σ_- eigenvalues. Moreover, we can reexamine the updating rule in Eq. (22c) as follows:

$$\Lambda^{m+1} = \frac{A(Z^{m+1}) - V^{m+1}}{\mu}. \tag{25}$$

which implies that $A^*(\Lambda^{m+1}) = \frac{1}{\mu}(A^*A)(Z^{m+1} - U^{m+1}) = \frac{1}{\mu}(A^*A)(U_\ddagger^{m+1})$, where $U_\ddagger^{m+1} := -P_\ddagger \Sigma_- P_\ddagger^T$ and it can be solved in polynomial-time from a simple linear matrix inequality (LMI).

Specifically, while the generic work in [55] has a direct implication, our LMI involves both linear mapping and an adjoint operator.

With the above accomplishments, we yield the proposed ADM in **Algorithm 3**.

Algorithm 3 ADM-Based Fast Initial Positioning

Input$(A_{ij}, \bar{A}_{ik})$, $(\hat{d}_{ij}^2, \hat{d}_{ik}^2)$, $1 \le i \le N, j \in NH_i, 1 \le k \le K$
Output $x_i, 1 \le i \le N$
Initialize primal $Z^0 \succeq 0$ and dual $\Lambda^0 \succeq 0$

for $m = 0, 1, \ldots$ **do**
Calculate ϵ^{m+1} from Eq. (23)
Calculate V^{m+1}, U^{m+1}, eigenvalue decomposition of U^{m+1}, and Z^{m+1} from Eq. (24)
Calculated Λ^{m+1} from Eq. (25)
end

Furthermore, we present the solid convergence analysis of this algorithm. which yields the global linear convergence. That is, Algorithm 3 can converge to the optimal solutions at rate O(1/m), where m is the number of applied iterations.

3.6 Fine-Grained Positioning from the Conjugate Gradient Algorithm (CGA)

This section presents the key steps of fine-grained positioning from CGA as follows:

1. Refine the initial location results from ADM through the design of fine-grained positioning.

2. Formulate the optimal criterion of the best estimated locations by examining the gradient of the WMLE objective function.

3. Derive the updating iterations with the construction of conjugate directions for efficient optimal point searching, called CGA, which provide final accurate location estimations.

After solving SDP relaxation from the proposed ADM, the solution obtained from SDP relaxation has a high-rank property. For example, in a 2D reservoir fracture, the high-rank optimal solution from the proposed ADM should be translated into a 2D location solution without losing optimality. In other words, from the results of fast initial positioning, we can fine-tune the sensor positioning to further increase the location accuracy. This approach is easily realized through the design of a searching algorithm for the optimal location solution in the correct dimensionality. In the following, we begin by examining the straightforward method, steepest descent (SD), which utilizes the gradient of the objective function to search the minimum. Then, we apply a more sophisticated search approach based on the conjugate gradient algorithm, which exploits the conjugate direction (CD) to outperform the conventional SD method [41].

3.6.1 Steepest Descent (SD) Method

We first reformulate the objective function in Eq. (16) of the localization problem as

$$\begin{aligned} f(X) = &\sum [\hat{d}_{ij}^2 - (x_i - x_j)^T (x_i - x_j)]^2 \\ &+ \sum [\hat{d}_{ik}^2 - (x_i - a_k)^T (x_i - a_k)]^2. \end{aligned} \tag{26}$$

Then we define ∇f as $\nabla f(X) = [Df_{x_1}, \ldots, Df_{x_n}]^T$ where $Df_{x_i} = [\frac{\partial f}{\partial x_i^1}, \frac{\partial f}{\partial x_i^2}]$ for 2D cases. Note that, ∇f is the decent direction of the objective function in Eq. (26).

The SD method [41] provides that given $X^{(0)}$, the search iteration follows

$$\begin{aligned} X^{(m+1)} &= X^{(m)} - \alpha_m \nabla f(X^{(m)}) \\ \alpha_m &= \arg\min_{\alpha \geq 0} f\left(X^{(m)} - \alpha \nabla f(X^{(m)})\right) \end{aligned} \tag{27}$$

where α_m is the step size of the $(m+1)^{th}$ iteration. In other words, it performs an exact line-search to determine the step size that minimize $f(X^{(m+1)})$ along the $\nabla f(X^{(m)})$ direction. Hence, it obtains the optimal step size α_m of the $(m+1)^{th}$ iteration by the following equation:

$$\left.\frac{df\left(X^{(m)} - \alpha \nabla f(X^{(m)})\right)}{d\alpha}\right|_{\alpha=\alpha_m} = 0. \tag{28}$$

As suggested by [49], α_m can be further obtained from Eqs. (26) and (28) by

$$rcl4c_1^2\alpha_m^3 + 6c_1c_2\alpha_m^2 + 2(c_2^2 + 2c_1c_3)\alpha_m + 2c_2c_3 = 0, \tag{29}$$

where $c_1 = -\sum_i Df_{x_i^{(m)}} Df_{x_i^{(m)}}^T$, $c_2 = -2\sum(x_i^{(m)} - x_j^{(m)})Df_{x_i^{(m)}} - 2\sum(x_i^{(m)} - a_k)Df_{x_i^{(m)}}$, and $c_3 = \sum[\hat{d}_{ij}^2 - (x_i^{(m)} - x_j^{(m)})^T(x_i^{(m)} - x_j^{(m)})] \sum[\hat{d}_{ik}^2 - (x_i^{(m)} - a_k)^T(x_i^{(m)} - a_k)]$. Note that the derived equation for α_m in Eq. (29) is a third order polynomial, so the analytical solution of the roots exists. Also, a widely-used Armijo rule [56] can alternatively serve as a close approximation of the step size.

Through the above gradient-based search, we are able to round the high-dimensional (rank) solution from the proposed ADM to the desired dimensionality of the sensor location. In the following, we introduce a more sophisticated search that achieves optimal points much faster than the steepest descent method and avoids possibly becoming stuck in local optima.

3.6.2 CGA with Conjugate Direction (CD)

The basic concept of the conjugate gradient algorithm [41] is to minimize the objective function (e.g., $f(X)$ in Eq. (26)), along with the corresponding conjugate direction (CD) of each iteration (e.g., $d^{(0)}$ and $d^{(m+1)}$, $m \geq 0$ in Eq. (31)), instead of adhering

to the gradient direction, as it does in the steepest descent method. Specifically, rather than adopting Eq. (27) in each iteration, the CGA provides that given $X^{(0)}$, the search iteration follows

$$X^{(m+1)} = X^{(m)} + \alpha_m d^{(m)} \tag{30}$$

where $d^{(0)} = -\nabla f(X^{(0)})$ determines the gradient direction for the first iteration and the step size α_m is determined by $\alpha_m = \arg\min_{\alpha \geq 0} \Phi_m(\alpha)$ where $\Phi_m(\cdot)$ is defined as $\Phi_m(\alpha) := f(X^{(m)} + \alpha d^{(m)})$. If CGA does not approach the minimum point after the current iteration, it constructs the next CD $d^{(m+1)}$ from the current direction $d^{(m)}$ by

$$d^{(m+1)} = -\nabla f(X^{(m+1)}) + \beta_m d^{(m)} \tag{31}$$

where β_m is obtained via the conjugate concept by Fletcher-Reeves [41] as $\beta_m = \frac{\|\nabla f(X^{(m+1)})\|^2}{\|\nabla f(X^{(m)})\|^2}$. In other words, the parameter sets of $(\alpha_m, \beta_m)_{m \geq 0}$ are obtained as

$$\begin{aligned} \alpha_m &= \arg\min_{\alpha \geq 0} f(X^{(m)} + \alpha d^{(m)}); \\ \beta_0 &= \frac{\sum_i Df_{x_i^{(1)}} Df_{x_i^{(1)}}^T (e_i - \alpha_0 F_i)^T (e_i - \alpha_0 F_i)}{\sum_i Df_{x_i^{(0)}} Df_{x_i^{(0)}}^T}; \\ \beta_m &= \frac{\nabla f(X^{(m+1)})^T \nabla f(X^{(m+1)})}{\nabla f(X^{(m)})^T \nabla f(X^{(m)})}, \end{aligned} \tag{32}$$

where $e_i = [\mathbf{0}^{1\times 2}, \ldots, \mathbf{0}^{1\times 2}, \mathbf{1}^{1\times 2}, \mathbf{0}^{1\times 2}, \ldots, \mathbf{0}^{1\times 2}]^T$ and

$F_i = [D_{x_i^{(m)}} Df_{x_1^{(m)}}, \ldots, D_{x_i^{(m)}} Df_{x_i^{(m)}}, \ldots, D_{x_i^{(m)}} Df_{x_n^{(m)}}]^T$.

Finally, **Algorithm 4** proposes the CGA for fine-grained positioning. To this end, we completely solve the underground localization with randomly-deployed sensors through the successive execution of the proposed ADM in **Algorithm 3** and the CGA in **Algorithm 4**.

Algorithm 4 CGA (Fine-Grained Positioning)

Input $f(\cdot)$ from Eq. (26), $X^{(0)} := [x_1^T, \ldots, x_N^T]^T$ from **Algorithm 3**
Output X^* % Sensor location
Set $m = 0$; **compute** $d^{(0)} = -\nabla f(X^{(0)})$

while $\nabla f(X^{(m)}) \neq \mathbf{0}$ **do**
Compute α_m according to Eq. (32)
Compute $X^{(m+1)}$ according to Eq. (30)
Compute β_m according to Eq. (32)
Compute $d^{(m+1)}$ according to Eq. (31)
Set $m = m + 1$
end
Set $X^* = X^{(m)}$

3.7 Evaluation of Performance in Oil Reservoirs

We evaluate the proposed MI-based localization solution, that is, **Algorithm 3**: ADM and **Algorithm 4**: CGA, in a practical scenario of 2D oil reservoirs. Simulation results confirm that our solution achieves great positioning accuracy and functions well even under severe environment impact in terms of volumetric water content, favored by the practical implementation in randomly-deployed WUSNs. Figure 16 shows the performance evaluation of the proposed Algorithm 3 and the corresponding theoretical analysis. We simulate the algorithm within a 2D oil reservoir fracture under 10% channel estimation errors. There are 60 randomly distributed sensors with a transmission range of 3.2 m; and two fixed anchors in which each transmission range covers the entire sensor area. The figure shows that the rapid convergence rate of rules follows our analytical derivation of O(1/m), validating the convergence analysis. The proposed ADM provides satisfactory values after 100 iterations which serves as a desired stopping point.

In the following, we first evaluate two proposed successive algorithms in the 2D setting for oil reservoir fractures. Then we examine the impact of the underground environment on localization performance.

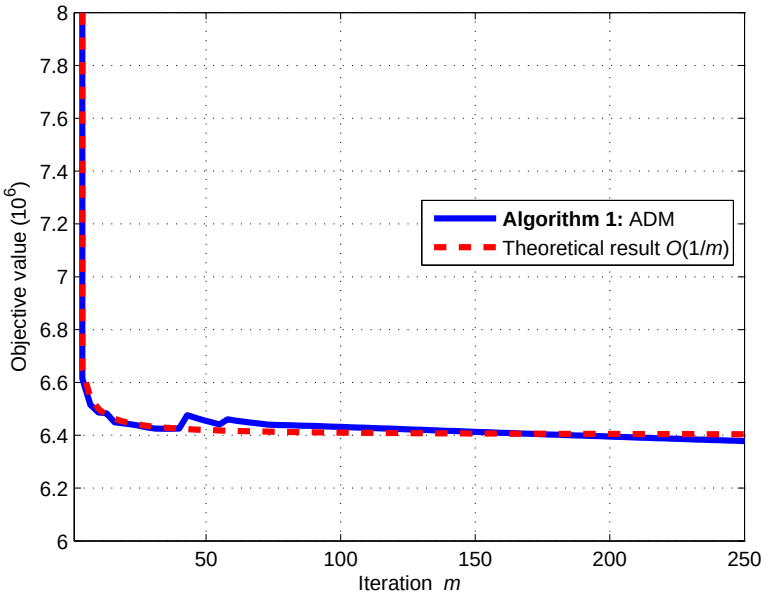

Figure 16: Validation of the fast convergence of **Algorithm 3**.

3.7.1 2D Localization in the Oil Reservoir Fracture

As shown in Figure 15, two anchors are assumed to be inside a single drilling well, and sensors are randomly spread in an 8×8 [m^2] area. Each anchor has a direct communication link to every sensor within its larger transmission range; we set the transmission range R of each sensor at 3.2 [m]. The parameters of coil antennas are set to fit in the thin fracture width (around 3-4 [cm]) at 1 [cm] coil radius, 10 turns, and $R_0 = 0.01$ [ω/m]. Moreover, we set the operating frequency at 7 [MHz] and several environmental parameters for the realistic oil reservoir at: 145 [°C], 30% sand particles, 20% clay particle, 1.5 [grams/cm^3] bulk density, 2.66 [grams/cm^3] solid soil particle density, 30% paramagnetic composites, and 10% ferromagnetic composites. In addition, to characterize the noise level from the estimation errors, we define the noise factor (nf) as $\hat{d}_{ij} = d_{ij}(1 + N(0,1) \times \text{nf})$, which is a given number between $[0, 1]$ to control the amount of noise variance. Moreover, to characterize the positioning accuracy by measuring the estimation mismatch, we define the root-mean-square

distance (RMSD) metric as

$$\text{RMSD} = \frac{1}{\sqrt{N}} \left(\sum_{i=1}^{N} \|x_i - \hat{x}_i\|^2 \right)^{1/2} \tag{33}$$

where x is the actual sensor location and $\hat{x}$ is that obtained from the localization algorithm.

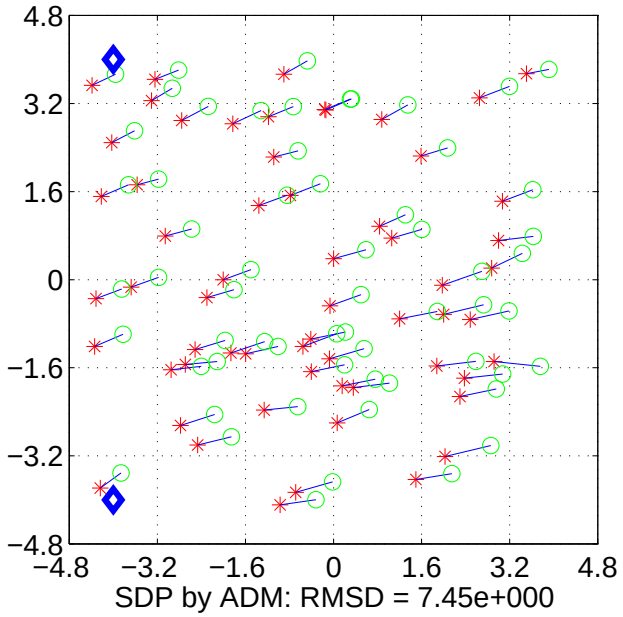

Figure 17: Sixty sensors with nf=1 after fast initial positioning (ADM).

Figures 17 and 18 show the localization results of 60 unknown sensor locations under high noise level (nf=1) after fast initial positioning (ADM) and after the entire localization (ADM+CGA), respectively. Blue diamonds at $[-4, 4]$ and $[-4, -4]$ represent two anchors, green circles refer to the original locations of unknown sensors and red asterisks refer to their estimated positions.

In Figure 17, although the estimated positions deviate only slightly from the actual locations after initial positioning by **Algorithm 3**, this step does not require a long processing time (i.e., only a few iterations) to obtain useful results. Figure 18 presents more accurate locations further obtained by executing fine-grained positioning by **Algorithm 4**, which reduces the estimation errors in RMSD and enhances

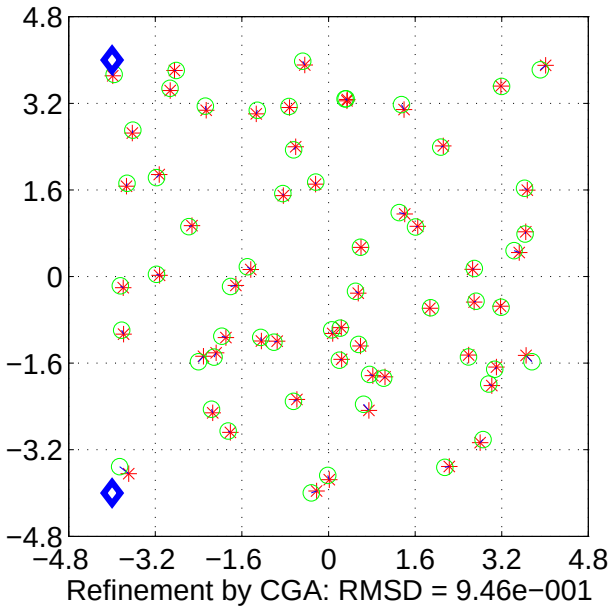

Figure 18: Sixty sensors with nf=1 after the entire localization (ADM+CGA).

localization accuracy with the fast search algorithm.

Figures 19 and 20 exhibit similar outcomes for the larger sample size of 100 unknown sensor locations. Figure 19 shows initial positioning that provides rough locations with fast processing time, and Figure 20 illustrates fine-grained positioning that further enhances the performance via a powerful and time-efficient search. Therefore, the above detailed evaluation confirms that the proposed localization algorithm performs well at high noise levels and is indifferent to network sizes through the fast and accurate operations of two successive positionings.

Next, we compare the proposed solution (i.e., ADM+CGA) to the benchmark scheme, which combines a conventional SDP solver and the steepest decent method (i.e., OPT+SD). Figure 21 shows a performance comparison with 60 sensors in a low-noise regime. The estimation error is calculated as a percentage of the sensor's transmission ranges of a sensor. For both 1.6 [m] and 3.2 [m] transmission ranges, the proposed solution produces a lower estimation error than the benchmark under all

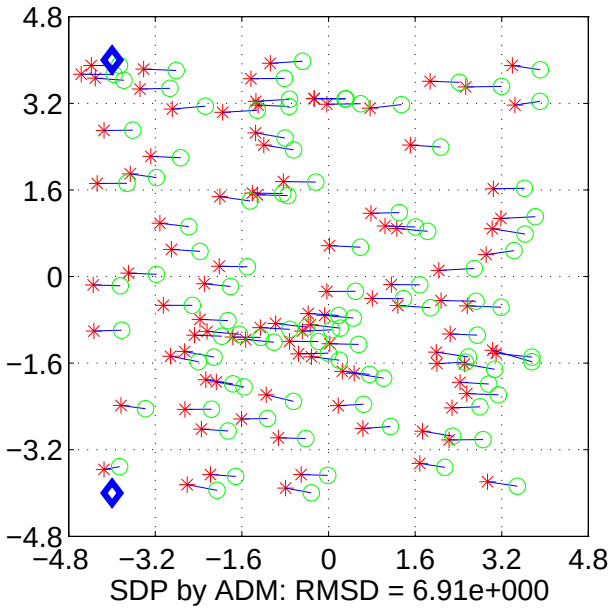

Figure 19: One hundred sensors with nf=1 after fast initial positioning (ADM).

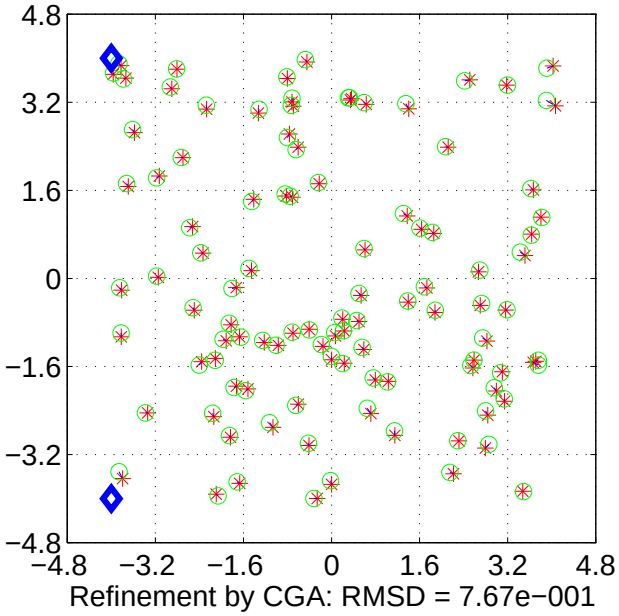

Figure 20: One hundred sensors with nf=1 after the entire localization (ADM+CGA).

evaluated noise factors. Two solutions exhibit similar performance under a very low-noise (nf=0.05) regime. Furthermore, Figure 22 shows the corresponding results in a high-noise regime. The proposed solution outperforms the benchmark and maintains

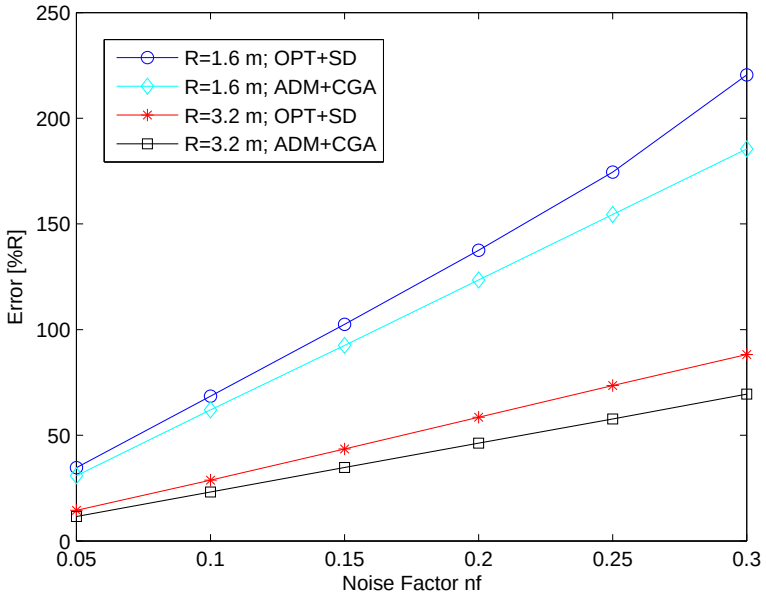

Figure 21: Comparison of the proposed solution and the designated algorithm for 60 sensors in various transmission ranges in a low-noise regime.

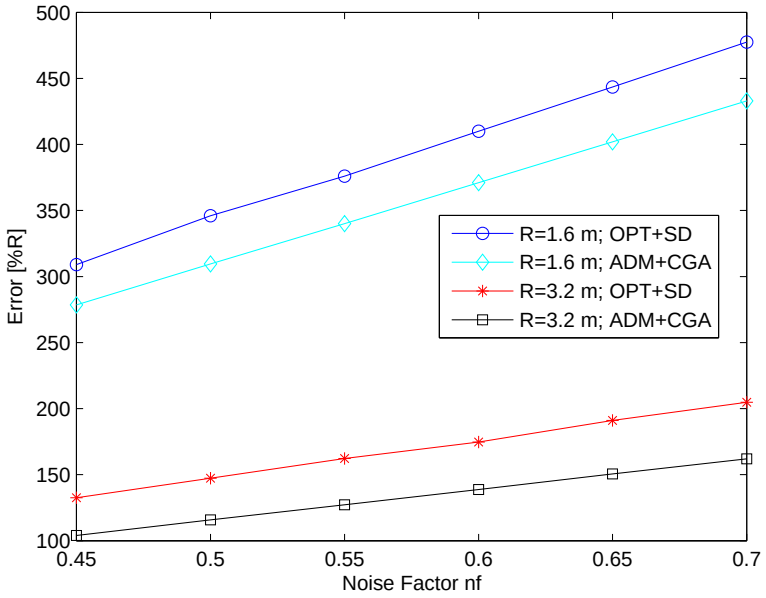

Figure 22: Comparison of the proposed solution with the designated algorithm for 60 sensors in various transmission rages in a high-noise regime.

noticeable performance improvement along the various noise factors. In summary, these results verify the superior design of the proposed algorithm, which performs

accurate and time-efficient localization in randomly-deployed WUSNs.

3.7.2 Impact of the Underground Environment

Although MI-based communication is adopted because of its suitability to underground environments, the water content in the surrounding areas greatly affects its quality. In particular, if more electrolytes are in the environments, they will significantly degrade the induction-based communication and thus MI-based localization. To illustrate this phenomenon, we randomly deploy 60 sensors, each of which can tolerate a maximum path loss of 120 [dB], in an oil reservoir. Figure 23 illustrates the negative impact of the electrical conductivity stemming from the various water contents. The salty water causes substantial signal conductivity, impairs the signal induction, and thus yields the worst RMSD values.

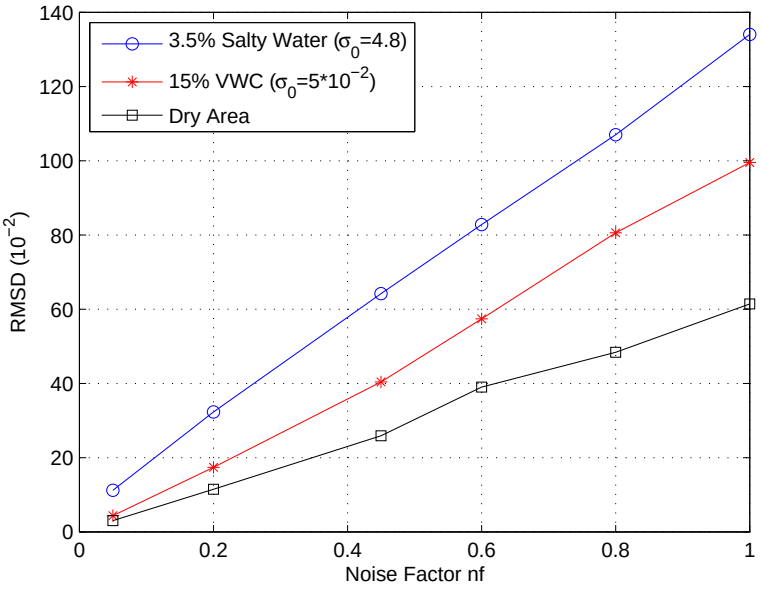

Figure 23: Impact of conductivity on the localization performance of the proposed solution in an oil reservoir environment. σ_0 is electrical conductivity at 20^oC.

Unlike the impact of the water content, the effect of the noise level is extremely low, that is, nf=0.05. In this scenario, the localization result of 15% volumetric water content (VWC) can approach that in dry areas. However, as noise increases, the

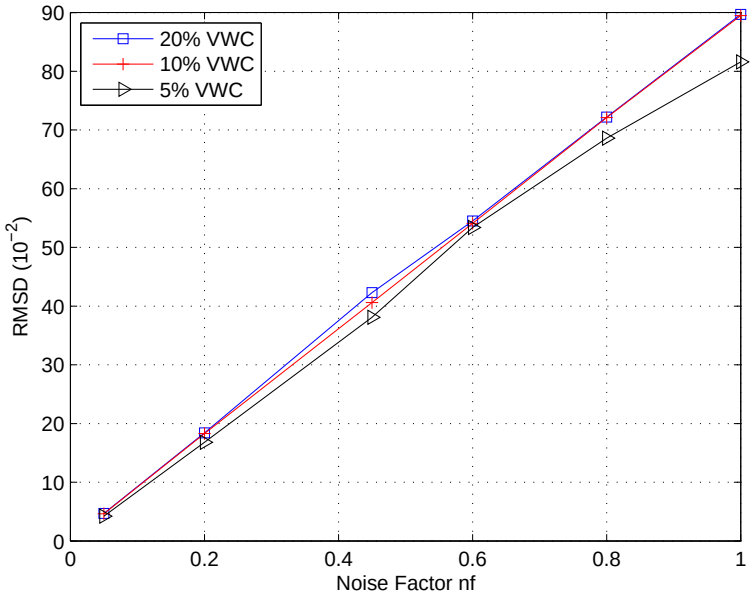

Figure 24: Impact of VWC on the localization performance of the proposed solution in an oil reservoir environment.

performance difference between the wet and dry areas also increases. In addition, focusing on normal water content with conductivity $\sigma_0 = 5 \times 10^{-2}$, Figure 24 shows the impact of different volumes of water content on localization. The results show that when the VWC increases, the performance difference is not obvious until it reaches very high noise levels. In fact, larger VWC triggers more signal conductivity than induction and damages communication and thus localization performance.

3.8 Highlights

In this chapter, we developed a novel MI-based localization algorithm that takes advantage of the promising features of the MI channel. Our solution jointly applies WMLE (weighted maximum likelihood estimation), SDP (semi-definite programming) relaxation, ADM (alternating direction augmented Lagrangian method), and CGA (conjugate gradient algorithm) with regards to the MI-based communication channel to achieve high positioning accuracy of wireless sensor devices (FracBots) in oil reservoirs while maintaining high computational efficiency. The fundamental

challenge for localization in randomly-deployed WUSNs is addressed by exploiting RMFS measurements from MI-based communication and fast, accurate successive positioning algorithms. Leveraging the multi-path and fading free nature of MI-based communication, RMFS from AWGN channel modeling serves as location-dependent information for the localization algorithm designs. Moreover, the fast ADM provides useful initial positioning within a few iterations, and the powerful CGA refines the initial results into highly accurate node positions. A performance evaluation confirmed that the proposed localization algorithm by guaranteeing considerable positioning accuracy represents a novel paradigm for localization in randomly-deployed WUSNs.

CHAPTER IV

OPTIMAL ENERGY PLANNING FOR SELF-CONTAINED WUSN IN HYDRAULIC FRACTURES AND OIL RESERVOIRS

In this chapter, we propose optimal energy planning for wireless underground sensor networks in hydraulic fractures and oil reservoirs. We develop an accurate energy model framework of a linear sensor network topology that gives feasible sensor transmission rates and network topology while guaranteeing sufficient energy as published in [57]. The motivation for this work is provided in Section 4.1. Section 4.2 discusses related work, Section 4.3 introduces the system model, and Section 4.4 examines the influence of magnetic-inductive channels on communication functionality. Section 4.5 introduces an optimal energy planning framework for wireless self-contained sensor networks, Section 4.6 presents an evaluation of our optimal energy planning framework, and Section 4.7 concludes.

4.1 Motivation

Wireless sensor nodes are a promising technology for collecting data in real time from underground environments. Such nodes, however, are not sufficient for transmitting the required data within a power budget because of limitations of their very small size and the environment. To overcome limitations caused by harsh environmental conditions and power constraints, we propose an accurate energy model framework of a linear sensor network topology, illustrated in Figure 25 that gives feasible sensor transmission rates and network topology while consistently guaranteeing sufficient energy. Since magnetic induction communication channels are employed, we begin

by examining the non-flat MI fading channels to obtain the accurate received signal qualities. Then we design MI-based modulation and error control coding schemes and evaluate the energy consumption for MI transmissions to determine the optimal rate of sensor transmissions and the number of sensors while satisfying the sensor packet error rate and energy constraints. We confirm the accuracy of our model via theoretical and simulation evaluations.

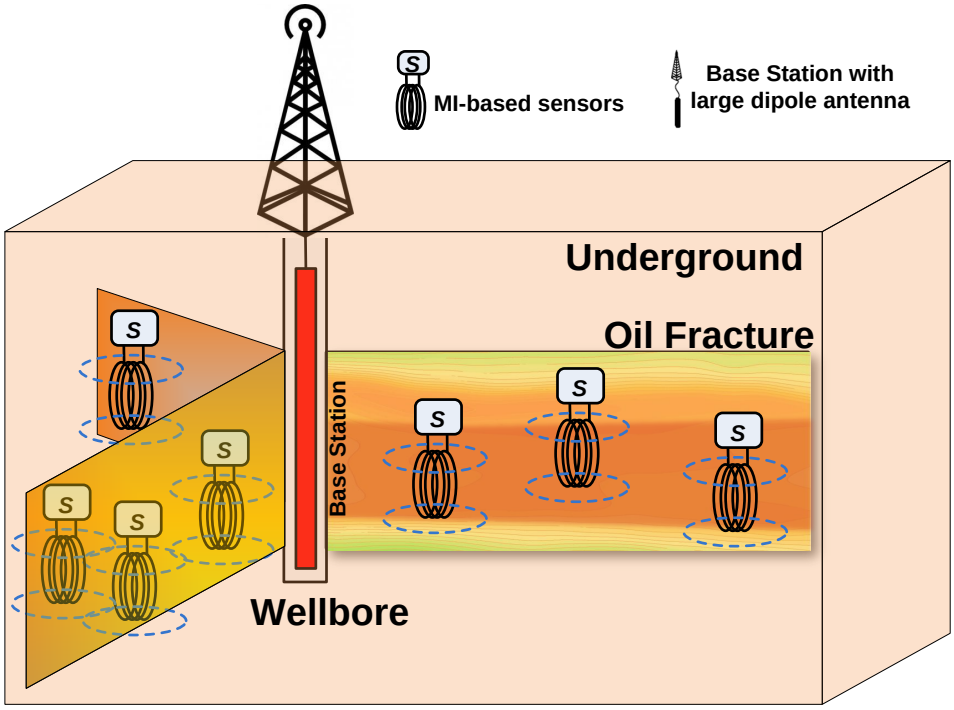

Figure 25: Network topology of the MI-based sensor network inside an oil fractured reservoir.

4.2 Related Work

Energy-constrained wireless sensor networks are typically powered by batteries that have limited operation time. Although replacing or recharging the batteries can prolong the lifetime of the network to a certain extent, it either incurs high costs or it is virtually impossible (e.g., for sensors embedded in building structures or underground sensors such as those in oil reservoirs). A more convenient alternative is to

harvest energy from the environment. The available common sources of energy are solar, wind and radio-frequency (RF) signals. For example, EM carries energy in the form of electric and magnetic fields that can be converted into energy, stored at the receiving front-end, and used to power the nodes of the WSN. The ability to transfer energy via contact-less RF ensures that the sensor nodes remain operational for a long time without the need of costly battery replacement efforts. Hence, this area of research has been the focus of several studies [58] and [59]. For example, one study [58] first proposed a capacity-energy function that characterizes the fundamental tradeoff in simultaneous information and energy transfer. For the single-antenna or SISO (single-input single-output) AWGN (additive white Gaussian noise) channel with amplitude-constrained inputs, the study showed the existence of nontrivial tradeoffs between maximizing the information rate and power transfer by optimizing the input distribution. Another study [59] extended the work in [58] to frequency-selective single antenna AWGN channels with an average power constraint by showing that a non-trivial tradeoff exists between frequency domain power allocation for maximal information and energy transfer.

RF energy harvesting (RFH) has emerged as a promising technology that has emerged for alleviating the node energy and network lifetime bottlenecks of wireless sensor networks (WSNs) is RF energy harvesting (RFH), in which the RF radiation pattern can simultaneously carry information and energy. These features have been exploited in multi-hop energy transfer (MHET) and combined with data transfer over the same RF signal (referred to as "simultaneous wireless information and power transfer," or SWIPT), without requiring critical alignment of the nodes [60].

The authors of [16] proposed coil deployment algorithms for MI-based WUSNs. Considering wireless power transfer, a study in [17] presented a propagation model and MI link budget for wireless power transfer systems. Then a paper [18] employed

the MI technique that efficiently transferred wireless energy over relatively long distances. For synchronous small-scale sensor networks, another paper formulated a cross-layer energy and delay optimization method [22] as a convex problem to quantify the tradeoff between delay and energy consumption.

4.3 System Model

In this section, we explain the system model for an underground wireless sensor network and the energy consumption and harvesting model of the entire sensor network system. Figure 25 illustrates the system architecture of the MI-based sensor network, which has two layers:

1. **FracBot (sensor)** that are injected into the fracture during the hydraulic fracturing process. Since the fracture is very thin, their positions are randomly distributed and linear inside the fracture. The wireless sensor nodes have no power source, but they are wirelessly charged by radiation from the base station inside the wellbore.

2. **A base station** that consists of a large antenna at the wellbore connected to a gateway located.

4.3.1 Linear Network Topology in Underground Environments

The characteristics of oil reservoirs and hydraulic fractures determine the network topology. Fractures, which average 0.01 m wide and 1 m high, can reach up to 100 m long. Based on the fractures characteristics, the positions of the sensors are random, static, and linear inside the fracture. Thus, we assume a static linear topology for the wireless sensor network inside the fracture as illustrated in Figure 26, which shows that energy is transferred and harvested in a one-hop energy fashion while data are transmitted in a multi-hop fashion.

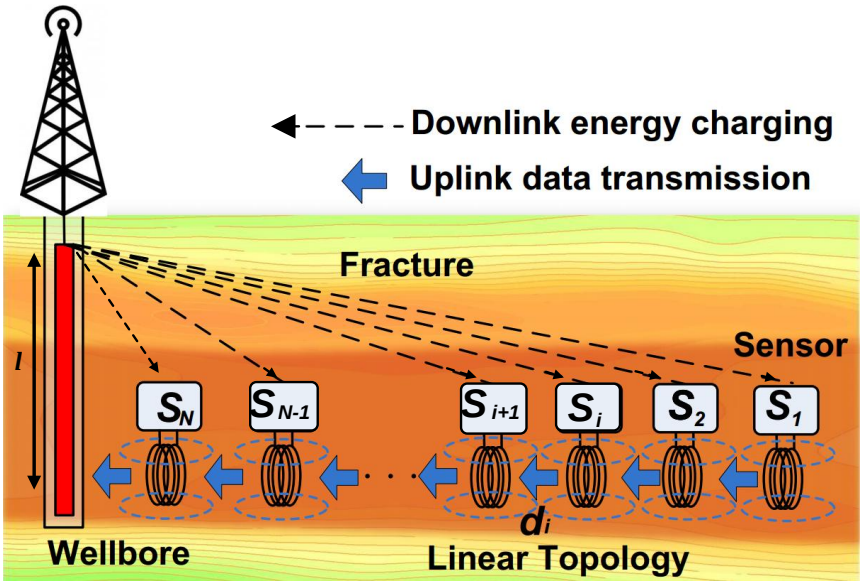

Figure 26: Topology of the MI-based sensor network in underground environments.

According to the system architecture described previously, we propose a three-stage operational structure as follows:

1. A one-hop radiative energy charging stage in which the base station radiates energy into a fracture and communicates with the sensor nodes. The base station is located at the wellbore and equipped with an ultra-high transmission power antenna that allows for the use of a MHz frequency to radiate EM signals and transfer energy through the reservoir medium to the MI sensor nodes distributed in the fractured reservoir.

2. A multi-hop MI-communications stage in which the sensor nodes use the MI communication mechanism to transmit the sensed data to the nearest neighboring node, and by consecutive relaying, the multi-hop transmission route is used to transmit the data back to the base station. The sensor nodes have no self-power source but instead, harvest energy from the EM radiation generated by the base station. It should be noted that the sensor nodes will not operate until they collect sufficient energy.

3. A backbone communications stage in which the base station receives the sensed data from the sensor nodes in the fractures and then forwards the data through an above-ground gateway.

4.3.2 Energy Consumption and Energy Harvesting for Wireless Self-Contained Sensor Networks

The downlink energy charge operates in a one-hope fashion to charge the entire sensor network. Because the fracture is extremely narrow, the size of the sensor nodes is extremely small, which limits the battery capacity. Consequently, a small battery cannot store enough power for the sensors to perform communication and sensing functionalities. As a result, the battery is replaced by an ultra-capacitor to store the harvested energy for the sensor operations. Accordingly, it is crucial to employ an accurate energy charging and consumption model since the capacity to transmit sensed data depends on the amount of harvested energy. From the channel models obtained in [8], the base station antenna generates an EM field in the MHz frequency range to transfer energy and transmits data to the sensor nodes in the fracture. As the EM field is influenced by inhomogeneous environment, and various fluids such as crude oil and proppants inside the fracture (and materials outside the fracture are soil and rock), the liquids and materials affect the path loss of the downlink channels. Hence, a balance between transferred and consumed energy is mandatory, enabling the entire sensors network to perform all sensing activities and rely on data to the base station.

4.4 Influence of Magnetic-Inductive Channels on Communication Functionality

To support reliable MI transmissions in underground, the peculiarity of MI communication channels (i.e., non-flat fading in the frequency response) should be investigated in detail. In this section, we first examine the non-flat MI fading channels to obtain

accurate received signal quality. Based on these, we design MI-based modulation and error control coding schemes and evaluate the energy consumption for MI transmissions.

4.4.1 Non-Flat Magnetic Inductive Fading Channels

As magnetic induction serves as a feasible solution for underground communication [8], a careful examination of its peculiar channel response is needed. First, Figure 27 illustrates the coil antennas used as the front-ends for MI transmissions among sensors, and the near-magnetic field of coils employed to disseminate information.

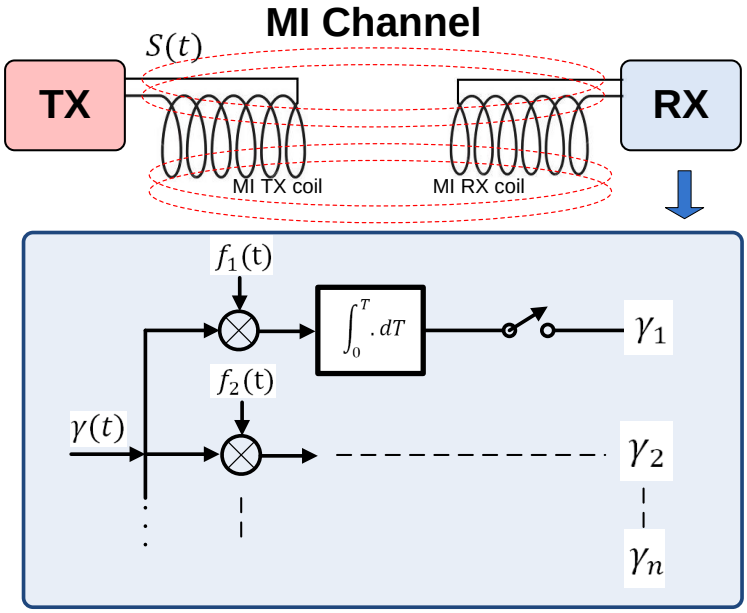

Figure 27: Front-end and receiver architecture for MI communication.

Our previous work [8] shows that MI communication encounters fewer channel variations than EM waves, which produce undesired noise, mainly from the thermal vibration of the circuit elements. Therefore, this make additive white gaussian noise (AWGN) to be applicable as an accurate assumption for the channel. Specifically,

the received MI signal can be formulated as

$$r(t) = s(t) * h(t) + n(t) \tag{34}$$

where $s(t)$ denotes transmitted signals from a sensor transmitter, $h(t)$ denotes the impulse response of the MI channel, and $n(t)$ represents environmental noise. Second, through the matched filter design for the MI receiver architecture, shown in Figure 27, the received MI symbols are calculated as

$$\begin{aligned} r_k &= \int_0^T [s(t) * h(t)] f_k(t) dt + \int_0^T n(t) f_k(t) dt \\ &\triangleq s_k + n_k, \ 1 \leq k \leq n \end{aligned} \tag{35}$$

where n_k is a Gaussian random variable with a zero mean and $N_0/2$ variance, and f_k corresponds to the kth operating frequency, implying that the mean and the variance of received MI symbol r_k are

$$E[r_k] = s_k \tag{36}$$

$$\delta_{r_k}^2 = \delta_{n_k}^2 = \frac{1}{2} N_0 \tag{37}$$

respectively. These values will be used to calculate the energy consumption of MI transmissions in later sections. In addition, with the aid of the transformer model for MI-based transceivers in general underground settings from our previous study, we are able to accurately characterize the channel response $H^{MI}(f)$ for MI-based transmissions in specific oil reservoirs.

Figure 28 shows the frequency response and the 3-dB bandwidth of MI channels in oil reservoirs. Specifically, through precise parameter settings for oil reservoirs, the results indicate that the transmission bandwidth of this MI system is still around 1 KHz (similar to the case in general underground environments) with a 10 MHz

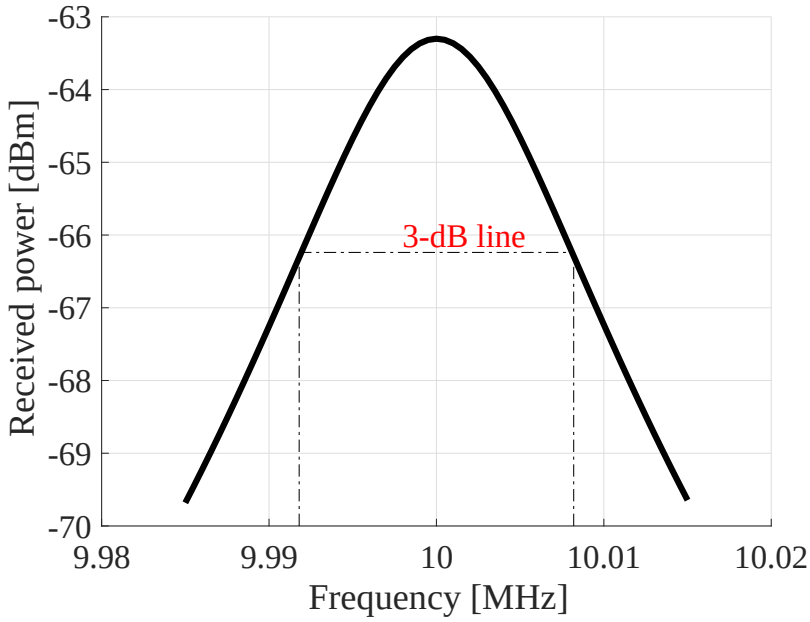

Figure 28: Frequency response $H^{MI}(f)$ of MI channels in oil reservoirs.

operating frequency. The 1 KHz transmission bandwidth is sufficient for the specific applications of oil reservoir sensing and monitoring. Moreover, in this bandwidth, the MI channel response lies non-flat, which significantly affects the received signal quality and the design of the communication functionalities. In the following, we account for this effect in the modulation and error coding scheme.

4.4.2 Magnetic Inductive-Based Modulation and Error Control Coding

As complicated modulation techniques consume more energy, they are not recommended for energy-constraint underground sensor networks. To this end, we select two simple but suitable modulation schemes, BPSK and 16-QAM, for our specific application to oil reservoirs. Moreover, because of the non-flat MI channel response, we jointly consider the power spectral density (PSD) of modulated signals and the channel response, when evaluating received signal strengths and bit error rates (BERs). The details are given as follows.

If we assume the adoption of the rectangular shaping pulse for MI-based transmissions, the PSD for PSK and QAM modulations can be obtained as follows:

$$PSD_{PSK}(f) = A^2 T_s \delta_r^2 (\frac{sin(\pi f)T_s}{\pi f T_s})^2 \tag{38}$$

$$PSD_{QAM}(f) = A^2 T_s \delta_r^2 (\frac{sin(\pi f)T_s}{\pi f T_s})^2 \tag{39}$$

where T_s denotes the symbol duration, A and δ_r^2 denotes the magnitude and the variance of MI signals, respectively. Let E_b^{MI} and E_s^{MI} be the received energy of one bit and one symbol over MI channels, respectively. This implies that $E_b^{MI} = E_s^{MI}/\log_2 M$ for MQAM modulation. Hence, given E_s as the energy of transmitted signal $s(t)$, we obtain the received energy under modulation scheme x as

$$E_s^{MI} = E_s \frac{\int^{BW} PSD_x(f) H^{MI}(f) df}{\int^{BW} PSD_x(f) df}. \tag{40}$$

implying that in order to capture the non-flat fading effect, the equivalent energy loss resulting from MI transmissions has a more complicated form (i.e., through the integration over the product of the signal PSD and the channel response). Figures 29 and 30 present a case study for 16-QAM modulated MI signals. The results indicate that as the feasible transmission bandwidth is small (i.e., around 1 KHz) for MI communication, the signal PSD can be considered a constant in this bandwidth, which will be true for most widely-used modulation schemes.

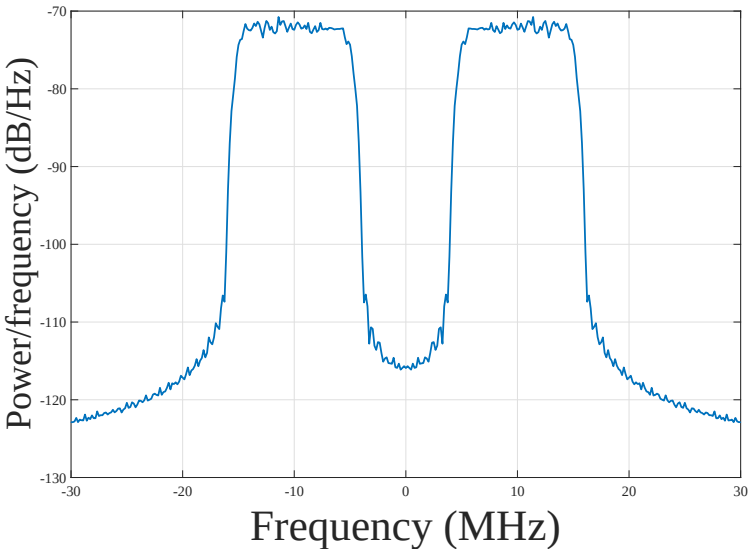

Figure 29: The PSD of the modulated signal.

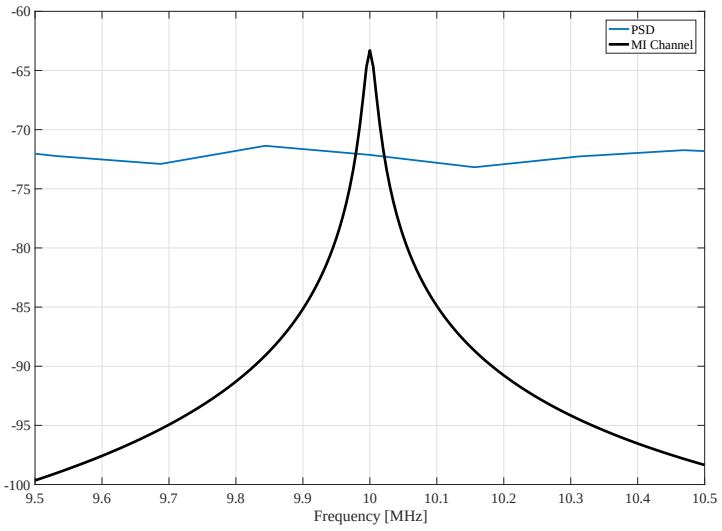

Figure 30: The comparison of frequency response $H^{MI}(f)$ and PSD.

Hence, the energy calculation in Eq. (40) will be greatly simplified. Finally, with the above accomplishments, we can obtain the BER for BPSK and MQAM modulated MI signals, respectively, as

$$\xi^{PSK} \cong Q\left(\sqrt{\frac{2E_b^{MI}}{N_0}}\right) \tag{41}$$

$$\xi^{MQAM} \cong \frac{4}{\log_2 M}(1-\frac{1}{\sqrt{M}})Q\left(\sqrt{\frac{3\log_2 M}{M-1}\times\frac{E_b^{MI}}{N_0}}\right). \tag{42}$$

We further consider the MI-based channel coding as follows. Specifically, the automatic repeat request (ARQ) requires timeouts and acknowledgements, which represent significant overhead for energy-limited underground sensor networks. Hence, we select forward error correction (FEC) to enhance link transmission reliability. In particular, multilevel cyclic BCH (Bose, Ray-Chaudhuri, Hocquenghem) codes are preferable to convolutional codes because of their energy-efficiency [33]. To this end, we adopt BCH codes $BCH(n,k,t)$ with rate $R^C = k/n$ in our work, where n denotes the block length, k the payload length, and t the correcting capability of the bit error (i.e., $t < n$). Specifically, given the BER ξ from Eq.(41), Eq.(42) and L[bit] as the packet length, the packet error rate (PER) Φ_i for the data transmissions between sensors x_i and x_{i+1} is obtained as

$$\Phi_i(d_i) = 1 - [1 - \sum_{j=t+1}^{n} \begin{pmatrix} n \\ j \end{pmatrix} \xi_i^j (1-\xi_i)^{n-j}]^{\lceil \frac{L}{k} \rceil}. \tag{43}$$

where d_i denotes the distance between sensors x_i and x_{i+1}. This PER can be further approximated as

$$\Phi_i(d_i) \approx \lceil \frac{L}{k} \rceil \sum_{j=t+1}^{n} \begin{pmatrix} n \\ j \end{pmatrix} \xi_i^j (1-\xi_i)^{n-j}. \tag{44}$$

As a result, to establish reliable MI communication, we formulate the end-to-end (i.e., from a sensor to the BS in the wellbore) PER constraint as follows: for sensor $x_i, i \in N$ with i hops to the BS in the linear topology,

$$1 - (1 - \Phi_i(d_i))^i \leq \Phi_T^{e2e}, \tag{45}$$

where Φ_T^{e2e} is a given tolerable maximum end-to-end PER, implying that the end-to-end PER should be no greater than the given tolerable value. Upon this stage, we have completed the study of the non-flat fading effect in modulation and channel coding designs.

4.4.3 Energy Consumption for MI Transmissions

Based on the energy modeling in Eq. (40), we are able to characterize the energy consumption from uplink data transmissions. Specifically, the energy consumption per bit for sensor $x_i, i \in N$ with MQAM can be modeled as follows:

$$\frac{E_s}{\log_2 M} + 2E_b^{elec}, \tag{46}$$

where E_b^{elec} is from the required energy per bit by the transmitter and receiver electronics (e.g., PLLs and bias current), which will be incorporated in our energy planning framework in Section 4.5.

4.5 Optimal Energy Planning Framework for Wireless Self-Contained Sensor Networks

From the detailed examination of MI channels and physical-layer communication functionality, we propose an accurate energy planning framework that facilitates self-contained sensor networks in oil reservoirs. Specifically, this framework generates feasible sensors' transmission rates and network topology while guaranteeing sufficient energy for all sensors. That is, we formulate the optimization problem of optimal energy planning as follows:

$$\max_{\{\lambda_i\},N} \quad \sum_{i=1}^{N} \lambda_i \tag{47a}$$

$$\text{s.t.} \quad 1-(1-\Phi_i(d_i))^i \le \Phi_T^{e2e},\ \forall i \in N; \tag{47b}$$

$$\sum_{j=1}^{i} \lambda_j R_j^C (E_b^{MI}(d_j) + 2E_b^{elec}) \le E_i^h,\ \forall i \in N \tag{47c}$$

where E_i^h and λ_i denote harvested energy (from a stable energy source of the BS) and the transmission rate of sensor x_i, respectively. The objective function in Eq. (47a) yields the total transmission rate for all N sensors. The constraint in Eq. (47b) stems from the consideration of reliable MI transmissions for all sensors (i.e., applying Eq. (45) for all $x_i, i \in N$.) Also, the constraint in Eq. (47c) implies that the energy consumed by sensor data transmissions should be no greater than the energy harvested by that sensor. Therefore, this optimization problem will determine the optimal sensor transmission rate and the optimal number of sensors while satisfying sensor PER and energy constraints at the same time.

To characterize the energy harvesting (i.e., $E_i^h, \forall i \in N$) from the BS in the wellbore, we adopt the recent results from the energy transfer model in [61]. Specifically, given d as the distance from the BS to a specific sensor, the corresponding path loss for this downlink channel can be formulated as

$$L_{DL}(d) \approx -10 \lg \left\{ \frac{A_1 + A_2 d^2}{d^4} e^{-A_3 d} \right\}, \tag{48}$$

where

$$A_1 = \frac{N^2 w^2 \mu_2^2 l^2 r^4 k_2^2 sin^2\theta}{64 R_c R_i k_1^2}, \tag{49}$$

$$A_2 = \frac{N^2 w^2 \mu_2^2 l^2 r^4 k_2^2 sin^2\theta}{64 R_c R_i}, \tag{50}$$

are the parameters related to the environments (i.e., the fracture) and coil antenna designs, and

$$A_3 = 2/\delta, \tag{51}$$

which characterizes the skin-depth effect for underground transmissions. The model parameters are: k_1, the wavenumber inside the fracture; k_2, the wavenumber

outside the fracture; μ_2, the effective permeability of the soil and rocks outside the fracture; w, the angular frequency; l, the length of the base station antenna; R_i, the input resistance of the base station antenna and d, the distance between the base station and the oil mole. R_c is the resistance of the coil (antenna of oil mole); r, the radius of the coil; N, the number of turns of the coil and θ, the angle of the coil positions. Moreover, with this path-loss formulation and the linear network topology in Figure 26, we formulate the harvest energy by sensor x_i as follows:

$$E_i^h = T_i^c \eta_i P_{TX} L_{DL} \left(\sqrt{l^2 + (\sum_{i=1}^{n} d_j)^2} \right), \tag{52}$$

where T_i^c and η_i denote the charging time and the energy conversion rate of sensor x_i, and P_{TX} the transmitted power of the BS. As a result, the formulated energy planning problem in Eq. (47) can be easily solved by commercial software solvers through an exhaustive search.

Working on the network planning problem of a large number of sensors, system architects often do not require precise values, but rough and meaningful results for the sensor transmission rate and network topology. Towards this end, we simplify the formulation in Eq. (47) with the consideration of $\lambda_i = \lambda, d_i = d, R_i^C = R^C, \forall i \in N$ as

$$\begin{aligned} \max_{\lambda, N} \quad & N\lambda \\ \text{s.t.} \quad & 1 - (1 - \Phi(d))^N \leq \Phi_T^{e2e}; && \text{(53a)} \\ & i\lambda R^C (E_b^{MI}(d) + 2E_b^{elec}) \leq E_i^h, \ \forall i \in N. && \text{(53b)} \end{aligned}$$

This problem can then be solved time-efficiently by the proposed Algorithm 5.

Algorithm 5 Fast Optimal Energy Planning.

set $N = 1$
repeat
  calculate
  $\lambda^N = \min_{i \leq N} E_i^h / [iR^C(E_b^{MI}(d) + 2E_b^{elec})]$
  set $N := N + 1$
until $N > \log_{(1-\Phi(d))}(1 - \Phi_T^{e2e})$
$N^* = \arg\max_i i\lambda^i$ and $\lambda^* = \lambda^{N^*}$ =0

4.6 Performance Evaluation

In this section we numerically evaluate the wireless energy charging and energy consumption models and discuss the effect of the BER and PER. It also shows PERs for 16QAM and BPSK modulation techniques and for different BCH codes. We set the parameters as follows: a transmission bandwidth of 1kHz, a packet size of 100 bytes, and an operating frequency of 10 MHz.

Figure 31 shows the minimum amount of transmission power required to enable inter-sensor communication via the MI channel in oil reservoirs. As the distance between the two sensor nodes increases, the required transmission power also increases dramatically as a result of the complicated transmission medium.

Figure 32 shows the harvested energy as a function of the distance between the base station and the sensor nodes in the oil fracture after a charging time of one hour. The wireless energy charging model shows that the power received by the sensor nodes overcomes the oil fracture conductivity constraints. For example, at a 25 m distance from the base station, the harvested energy is around -10 dBmJ, which is sufficient for charging the ultra-low power MI-based sensor nodes.

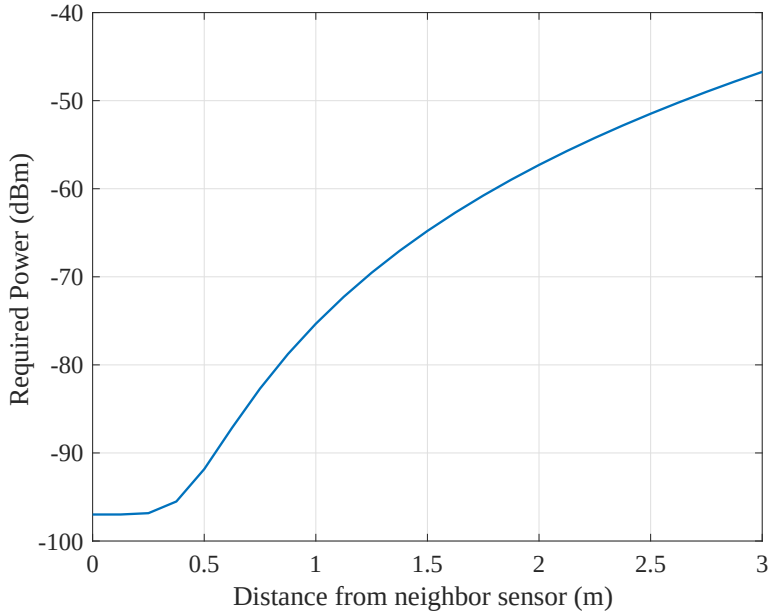

Figure 31: Required power to transmit data from sensor to neighbor sensor.

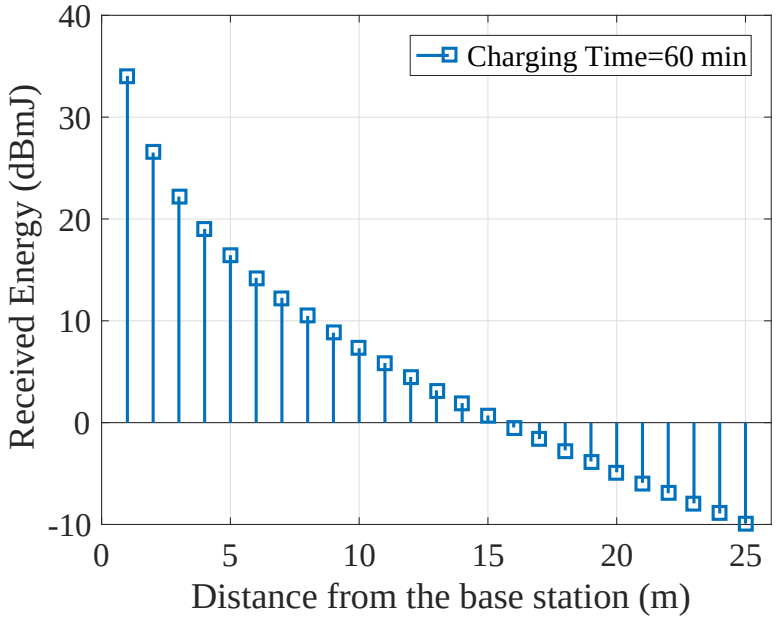

Figure 32: Energy received by sensors from the base station.

Figure 33 shows the PER versus the SNR for 16QAM and BPSK modulation

techniques and for different BCH(n, k, t) codes and no FEC scheme. We set the transmission range at 2 m, the packet length at 100 Bytes, and the working temperature at 283°K. While BPSK achieves a smaller BER for any given SNR among modulation techniques, it results in the best PER performance for every channel coding scheme. In addition, while consuming more energy, the powerful coding schemes (i.e., with high error correcting capability) maintain a lower PER for any given SNR. A tradeoff exists between energy consumption and transmission quality. Figure 34 shows the optimal total transmission rate of the entire network with respect to the various modulation and coding schemes. The total charging time is set at one hour. The results imply that BPSK can result in higher transmission rates than 16QAM, regardless of the channel coding scheme. In addition, the investigated modulation and coding scheme can achieve an average of 8 Kbps per sensor.

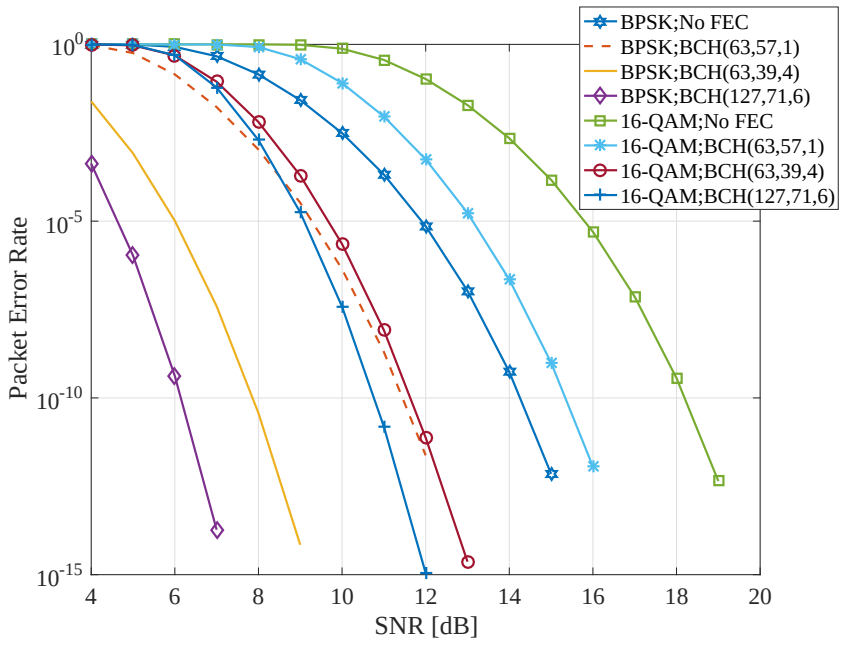

Figure 33: Packet error rate (PER) vs the SNR (dB) for BPSK and 16QAM modulation techniques and BCH(n,k,t) coding schemes.

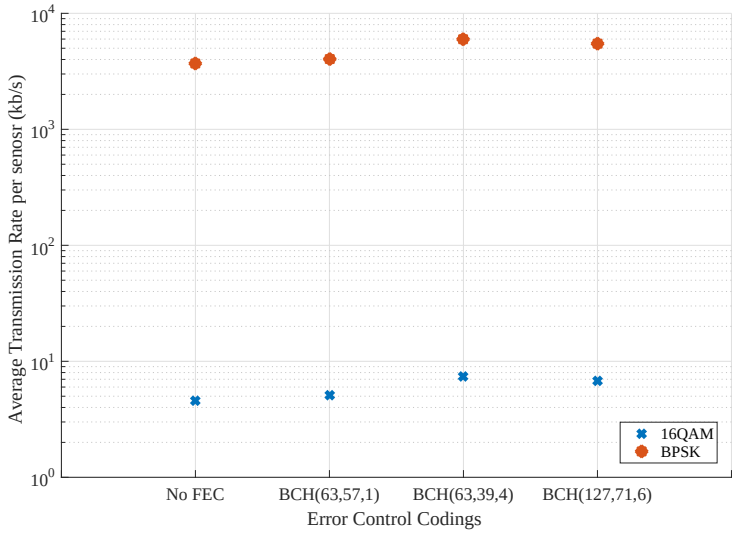

Figure 34: Optimal transmission rate for BPSK and 16QAM modulation techniques and BCH(n,k,t) coding schemes.

4.7 Highlights

This chapter proposed an optimal energy planning approach of a linear oil sensor network topology that ensures an accurate energy model that provides optimal sensor transmission rates and optimal sensor network planning. We show how the inhomogeneous environment strongly affects the downlink and uplink channels inside oil reservoirs. Since magnetic induction communication channels are employed, we examine the non-flat fading nature of MI communications to obtain accurate received signal quality for reliable MI communications inside oil reservoirs. Then, we design MI-based modulation and error control coding schemes and evaluate the energy consumption for MI transmissions to determine an optimal sensor transmission rate and number of sensors while satisfying the sensor PER and energy constraints. We also evaluate modulation and error control coding for transmitting data between nodes. We obtain the optimal total transmissions rate of the entire network and number of sensors while satisfing the PER and energy constraints of sensors.

CHAPTER V

MI-BASED FRACBOT NODE DESIGN FOR MONITORING HYDRAULIC FRACTURES AND OIL RESERVOIRS

In this chapter, we design a novel prototype of an MI-based wireless sensor node (FracBot) to be used as a platform for a new generation of WUSNs for monitoring hydraulic fractures and unconventional reservoirs as well as measuring other wellbore parameters as published in [62]. We develop an MI-based wireless sensor node to demonstrate the feasibility and capability of using MI-based communication in underground environments. In particular, we design and implement a sensor device that can be used to collect information such as temperature, pressure, chemical composition and other variables in underground environments. The design and development is based on short range communication using near field communication (NFC) as a physical layer combined with an energy harvesting capability and ultra-low power requirements. This node design is not restricted to oil and gas exploration; it also presents high potential for use in applications in intelligent agriculture, pipeline fault diagnosis, mine disaster rescue, concealed border patrol, underground city infrastructure monitoring, and underwater applications.

Section 5.1 provides the motivation for this work and Section 5.2 discusses the related work. Section 5.3 presents the hardware design roadmap. Section 5.4 demonstrates the FracBot hardware design. Section 5.5 presents the NFC/MI antennas design used in FracBot. Section 5.6 discusses FracBot prototypes and Section 5.7 concludes.

5.1 Motivation

The optimal development of oil and gas fields is significant and necessitates real-time information such as pressure, temperature, and fluid composition. The need to assess the rich venues of oil and natural gas reserves demands the design and the development of a new technology for monitoring hydraulic fractures and unconventional oil and gas reservoirs. Such a technology must be capable of monitoring oil reservoirs in real time so that we can extract more oil to satisfy global energy demand. A promising technology for collecting data from hydraulic fractures and oil reservoirs in real time is the wireless sensor nodes. As such nodes, however, have not yet been designed for this special application, they are not commercially available in the market. The design of these nodes must overcome limitations caused by small size requirements, and harsh environmental conditions, and energy constraints. Thus, this work proposes a novel prototype of an MI-based wireless sensor node (FracBot) that can be used as a platform for a new generation of WUSNs for monitoring hydraulic fractures and unconventional reservoirs as well as measuring other wellbore parameters. We design and develop the hardware of the MI-based wireless sensor for short range communication using near field communication (NFC) as a physical layer combined with an energy harvesting capability and ultra-low power requirements. Although NFC/MI techniques have been considered unconventional approaches to overcoming the key challenge of inter-node communication for WUSNs in underground environment, we have used cost-effective and commercial off-the-shelf components to relize a design incorporates these characteristics. We confirm the performance of our design via theoretical and experimental evaluation. The FracBot can operate perpetually with minimum energy radiated conditions. It can also establish a communication link and transmit data in reservoir-like environments, including air, water, sand, and stone media. The development of hardware and antennas allows us to understand the challenges, improve electronic sensitivity, and optimize the minimum resources

necessary to miniaturize the FracBot hardware.

5.2 Related work

Existing reservoir [4] and wellbore monitoring systems [5] are incapable of measuring data inside oil reservoirs, and no current technology is able to deliver the in-situ monitoring of conventional reservoirs in real time [3],[6]. In addition, although the accessibility of tight unconventional oil and gas reservoirs depends on hydraulic fracture technology, no reliable method of characterizing a fracture and providing specific information about fracture size, shape, and orientation is currently available [63]. Despite the availability of information-gathering approaches such as microseismic and tiltmeter surveys, they provide no vital data about the inner workings of reservoirs and are typically inaccurate, costly, and time consuming [64].

In response to the above need, both industry and the academic community have devoted a great deal of effort to the design and development of in-situ sensing systems for gathering vital data from hydraulic fractures and reservoirs. Most recent efforts, however, have been dedicated to the development of very small and well-suited sensors that can withstand the severe oil reservoir environment [2]. The key challenge to realizing WUSNs is the development of wireless communication in underground oil reservoir environments. Most existing wireless communication systems use a dipole antenna to propagate electromagnetic (EM) waves, which is not appropriate for underground environments owing to high material absorption loss. An MI technique can provide an alternative solution to realizing WUSNs in underground environments and address their current problems including high path loss, difficulty launching wireless signals, and short system lifetime [65].

MI techniques have been investigated as an alternative solution to the main challenge of inter-node communication in the underground environment [8]. Instead of using a large dipole antenna, sensor nodes use an MI coil antenna to transmit and

receive wireless signals through magnetic coupling. The near magnetic field of MI coil antennas can efficiently penetrate a high-loss oil reservoir channel and establish constant channel conditions, enabling wireless communication and energy harvesting inside hydraulic fractures and oil reservoir media [61]. In addition, the lack of an external source of energy to power and operate FracBot nodes and the extremely small size of nodes that prevents them from accommodating battery space create major challenges that must be overcome with regard to oil reservoir media. Once the FracBots are injected into the fracture or the oil reservoirs, they cannot be replaced. Therefore, the only way to power the sensor node is by harvested energy from power radiated by the base station installed in the wellbore. This concern was well addressed in Chapter 4 and published in [57].

Near-field communication (NFC) is a wireless short-range interaction that enables simple half-duplex communication between inductive coupled systems via magnetic field induction when they are within a few centimeters of one another. NFC enables communication between transmitting and receiving antennas when they are coupled via magnetic field induction at 13.56 MHz (the ISM band). Accordingly, NFC occurs in the MI near field not as the electromagnetic (EM) far-field communication that occurs through radiation power in far field zone. It is a simple version of long-range EM wireless communication such as Bluetooth and WiFi. NFC technology, a subset of the RFID technology for contactless short-range communications, was established by Sony and Philips in 2004 [66]. NFC systems have numerous advantages such as low propagation delay, high efficiency, and low cost, as well as a strong capability to penetrate non-magnetic materials (e.g., water and, concrete). In addition, it has unique features such as no multipath fading and and strong immunity to interference with other RF systems operating out of near-field systems ranges [67]. NFC technologies have been originally employed in many applications such as underwater communication, underground communication, contactless information transmission,

health monitoring, wireless powered biomedical applications, and real-time localization [8, 68, 69].

To evaluate the performance of the NFC link, researchers have extensively studied the link budget and propagation and generated a number of models [70]. One study [71] proposed a near-field propagation model equivalent to the Friis transmission law. Other studies [8], [70], [72] have analyzed NFC propagation characteristics such as bandwidth, capacity channel, path loss, the bit error rates for different applications such as wireless underground sensor networks and underwater communication. In addition, according to Shannon law, the crucial-key performance of any communication link depends on both the bandwidth and received power. Thus, the optimal link capacity entails a trade-off between the bandwidth and received power [73].

For underground oil reservoir environment, NFC/MI techniques have been considered unconventional methods of overcoming the key challenge of inter-node communication for WUSNs in the underground environment [8]. As an alternative to using big traditional antennas in RF technologies with an electrical length of $\lambda/4$ which is not applicable in an oil reservoir environment, sensor nodes exploit a compact MI coil antenna to communicate through magnetic coupling between the transmitter and receiver antennas. According to the characteristics of NFC, the MI field generated by NFC coil antennas can penetrate a high-loss oil reservoir media and launch a constant MI channel that enables wireless MI communication and energy harvesting inside a hydraulic fracture and the oil reservoir environment.

5.3 Hardware Design Roadmap

This section describes the design requirements and implementation processes of the FracBot node platform. The system is made up of a hardware platform and a software stack for drivers and interfacing.

The hardware design roadmap outlined in Figure 35, shows the steps of design once

the idea and requirements are specified. Component selection is an extensive process, requiring choices from a multitude of available products, and it dictates how the remaining steps proceed. Prototyping and software development is more constrained, involving the development of a prototype working sensor node and related software. Once the prototype design has been made, it is implemented in a schematic diagram and then as a printed circuit board. Then, the firmware and software are implemented. After this stage, a completed circuit has been made and the last step is testing and verification.

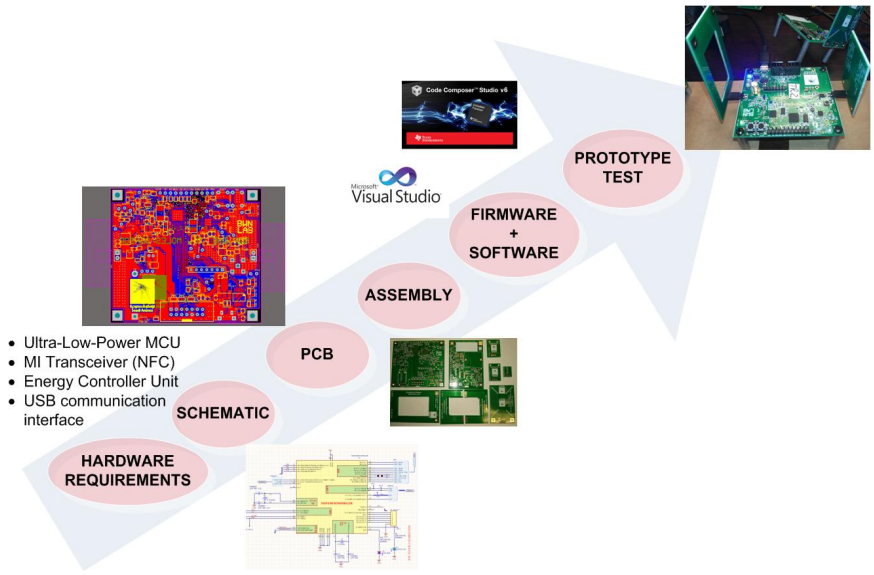

Figure 35: Roadmap of the FracBot design.

5.3.1 Hardware Design Requirements

The main part of *WUSN* is the sensor node; especially in applications of underground hydraulic fracture and reservoirs monitoring. Thus, efficient node design requires restricted characteristics that sustain operations in harsh environments with high path loss, high temperature and pressure, and limited energy. In addition, the very small size needs to optimize every component based on their requirements as it can save development time, board space, and cost. Figure 36 shows the main requirements of the design. The main characteristics of our design are a long operating time, ultra-low

power, a processing function, an efficient communication layer, and energy-harvesting and sensing capabilities. The simultaneous implementation of all five features enables the node to run in a perpetual powered status. In the following subsections, we explain the details of each feature.

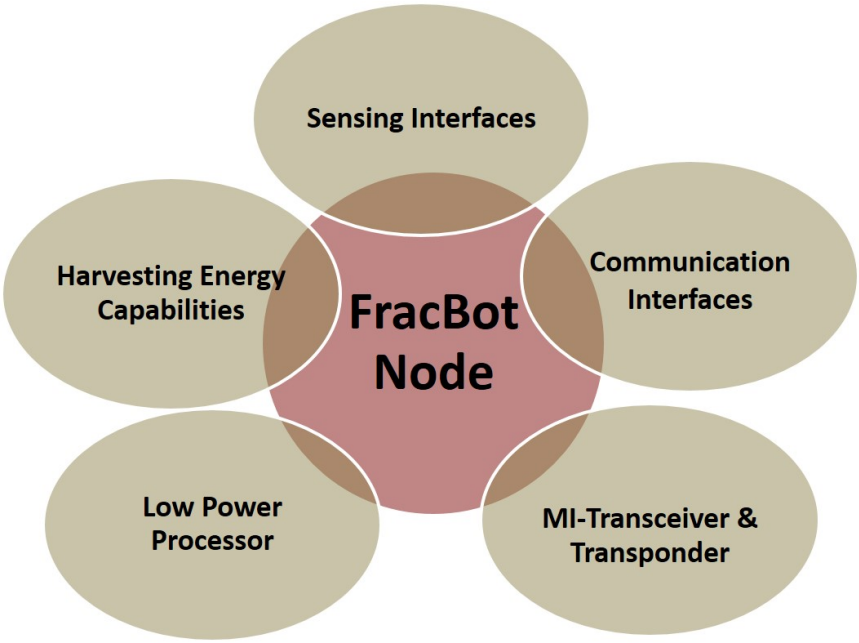

Figure 36: Requirements of the FracBot design.

5.3.1.1 ***Long operating period and ultra-low power electronics***

One of the main challenges in WUSN is energy management. The limited energy provided by a battery or an energy harvesting circuit is due the reduced size of sensors constrained by this application. Therefore, the electronic design must be highly efficient and capable of dramatically reducing power consumption. Thus, our sensor design is composed of ultra-low power electronic chips that enable a switch between the active mode and the deep sleep mode (ultra-low power). This feature reduces sensor power consumption by 98% [74]. Figure 37 shows the flowchart of tasks executed by the energy management unit (EMU), which functions independently of the sensor processing unit. Once the harvesting circuit collects the minimum

energy requirements in the battery or the super-capacitor to operate the node, the EMU will continuously indicate the energy levels, allowing the sensor to execute data acquisition, update the near-field communication (NFC) memory, and transmit the readings to the next node.

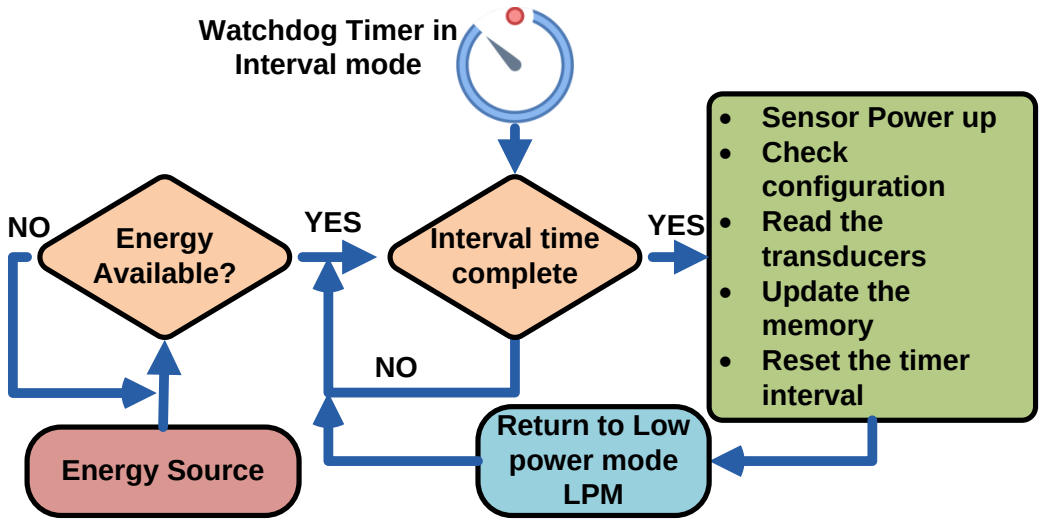

Figure 37: Interval mode flowchart.

5.3.1.2 ***Processing and microcontroller***

The most important feature of the FracBot is the processing function, which is represented by a microcontroller. It must have low voltage and power, advanced low power modes, and multi-peripheral interface support.

5.3.1.3 ***Efficient communication layer***

Reliable communication for underground environments was demonstrated using the MI technique, which overcomes the problems caused by environmental conditions [8]. The RFID technology uses the MI technique to provide magnetic coupling and data transmission. In 2004, with the advent of the NFC, nodes were able to perform bidirectional communication and energy transfer through magnetic induction coupling. Commercial off-the-shelf chips operate in 13.56 *MHz* for short distance via

half-duplex communication. The magnetic field generated through the NFC coil antenna can penetrate the high path loss media and establish the MI constant channel condition.

The FracBot needs to have a high efficiency transceiver that allows two-way communication between nodes in order to distribute information such as routing sensor data to a base station. The transceiver must also work in NFC and feature received signal strength indication (RSSI) as well as enable multi-transponders interfaces; the transponder, however, can only receive the data and feature dual connection interface with the memory and an antenna . The choice of a transceiver and a transponder have a considerable impact on power consumption as the transceiver, when idle or sending/ receiving data, will generally consume more power than any other component.

5.3.1.4 ***Energy-harvesting capability***

The data acquisition capacity depends directly on the energy available in the node. Traditionally, wireless sensor nodes are powered from batteries however batteries, which have a limited operating lifetime and need to be replaced regularly. In our applications, once nodes are injected into the hydraulic fracture, they cannot be replaced or reached, and because of their extremely small size, nodes are not able to accommodate even a tiny battery. In addition, the high temperatures of underground environments undermine the safe operation of chemical batteries, such as lithium, lithium ion, and lithium polimery. Thus, powering sensors after placement into the reservoir creates sizable barrier to their continuous operation. Therefore, the only option for provide sufficient power to sensors inside underground environment (i.e., soil, hydraulic fracture, or reservoirs) to harvest available energy from power radiated by the base station. The energy-harvesting process for this specific application is an energy management unit that harvests surplus power stemming from NFC communication. To support this feature, however, sensors must include special

energy-harvesting components.

5.3.1.5 ***Sensing capability***

FracBot nodes must consist of a sensing function. The sensor integrated with the FracBot must be accurate and consume very low power. Power consumption can be affected by minimal sleep and sensing currents and low turn on and off times as well as the time it takes for sensor to be ready to accurately sense and generate a reading.

5.3.2 Implementation Process

We need to follow a well-organized process to meet the design requirements to produce the FracBot prototype illustrated in Figure 38. The implementations procedures are:

- **Components selection:**

  Each component has to be carefully selected to ensure that it is suitable for the FracBot node and that it raises no compatibility issues. The selection is based on its design requirements listed earlier and its availability in the market.

- **Schematic drawing:**

  Circuit schematics represents a circuit in a simplified graphical manner that uses icons as components and lines between specific points on icons as traces. It does not describe in detail the physical aspects of the circuit. It illustrates only components spaces and interconnections.

- **PCB design:**

  The PCB board is designed using the free software EAGLE PCB, which creates the routing and generate GERBER files to start production. The board consists of two layers with thickness of 1.6mm and made of FR-4 material. The trace/spacing resolution is 6 mils (0.152mm), which can be reduced to 2 mils (0.05mm) for miniaturization process.

- **Components assembly:**

  After PCB is fabricated, the components are soldered to the PCB in their position denoted in the schematic drawing. Then, the board will be dried and inspected for any extra soldering that can make any short circuit. Finally, the board is connected to the power supply to activate it.

- **Firmware and software coding:**

  The firmware is coded for the microcontroller using Code Composer Studio (CCS). The purpose of this code is to operate and manage the microcontroller and eventually the entire FracBot node. To debug and demonstrate that the hardware performs as required, software that interfaces with the microcontroller is developed using Visual Studio.

- **Testing and verification:**

  This is the final stage of the process. All functions of a node are tested to ensure that they are working properly and deliver the potential tasks. To access the microcontroller and debug the firmware, the software is used for communication with the node through a USB connection.

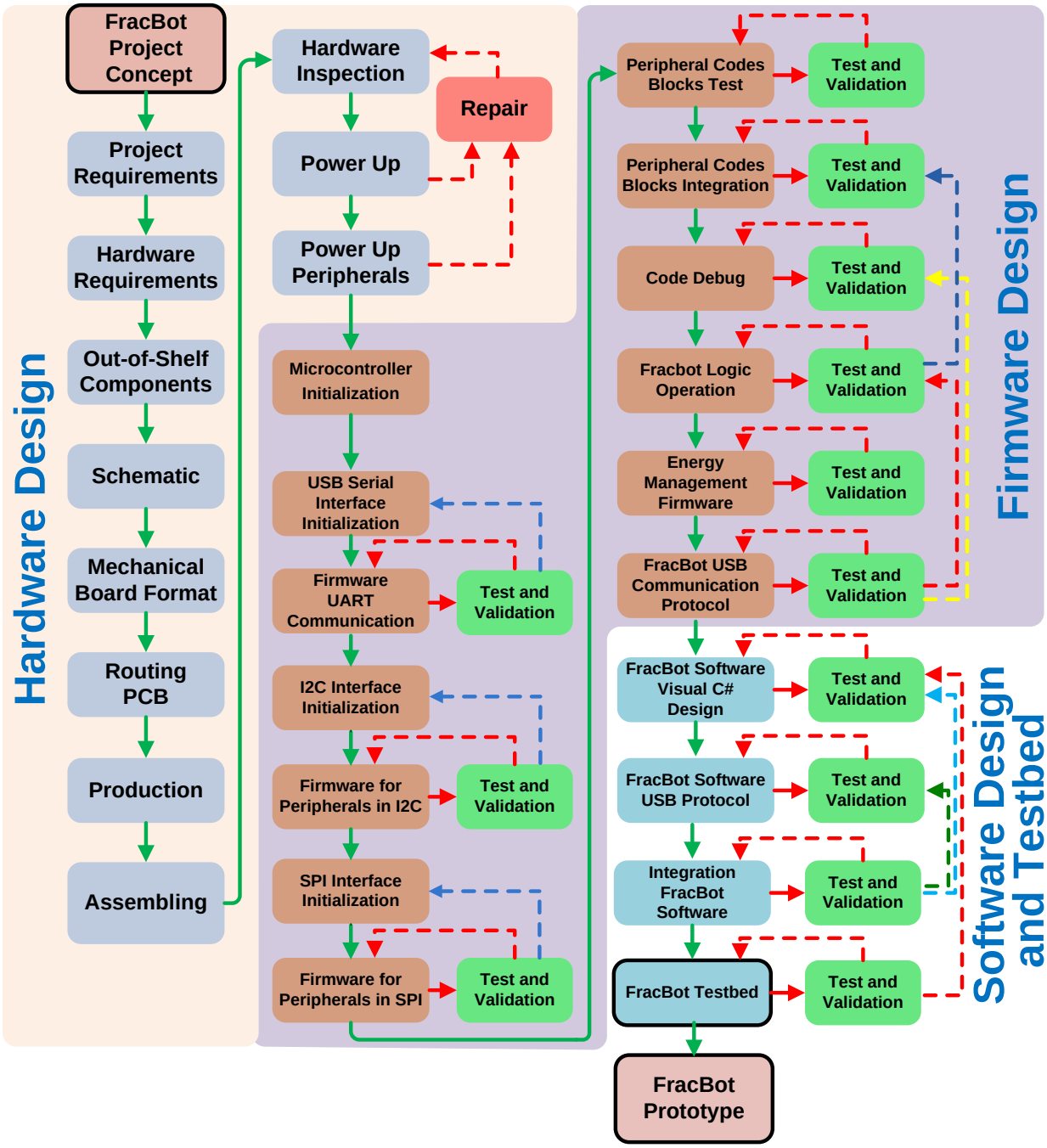

Figure 38: Flowchart of a FracBot fabrication.

5.4 FracBot Hardware Design

In this section, we discuss our design of the new cost-effective sensor using commercial off-the-shelf components. This design is the first one developed to work in hydraulic

fractures and oil reservoirs. Such nodes are currently not available in the market since they need to be designed specifically for this application to overcome limitations caused by the small size requirement and the environment. Accordingly, we design the sensor node to be a platform for a new generation of WUSNs that serve various purposes, provide flexibility, and allow for experimentation. This design is highly unique with regard to its highly unique communication layer, size, and energy source, features that overcome limitations caused by harsh environmental conditions and energy constraints. That is, the node is capable of collecting data from the harsh subsurface environments of water/gas/oil reservoirs and hydraulic fracture in real time. To realize such a design, we had to carefully follow the fabrication process to satisfy its requirements: a long operation time , ultra-low power, efficient communication layer and harvesting energy. It should be noted that in such a small platform, optimizing each component based on its requirements is critical, for it can save development and implementation time, board space, and cost. In addition, as we follow the fabrication process, the freedom to make changes in the components or add functions diminishes.

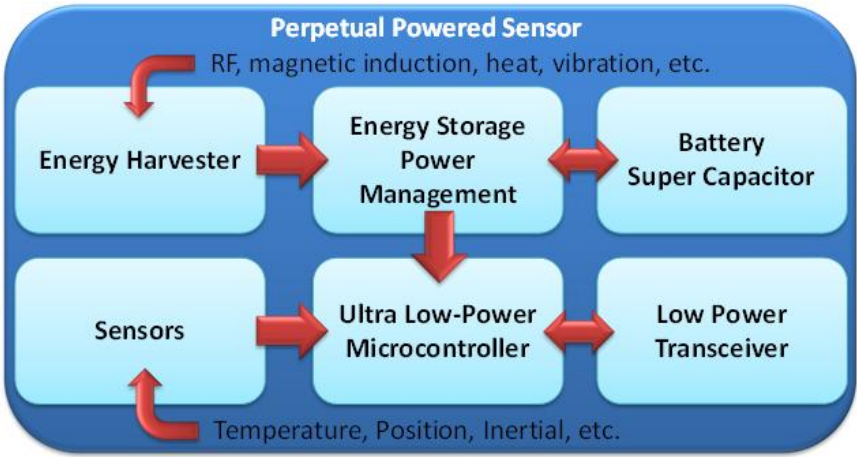

Figure 39: Block diagram of the FracBot architecture.

Figure 39 presents a functional diagram of the active FracBot hardware design

using ultra-low-power electronic and harvesting energy features associated with dual the NFC interface. Figure 40 illustrates the active FracBot prototype, which consists of a microcontroller, USB communication, an EMU, a temperature sensor, a dual NFC transceiver (active and passive interfaces), and a supercapacitor. The details of each components are explained in the following subsections.

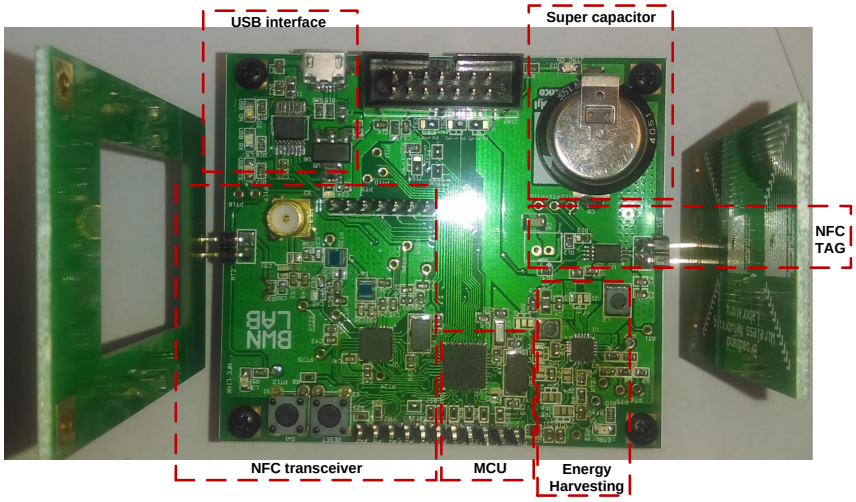

Figure 40: Active FracBot node.

5.4.1 FracBot microcontroller (MCU)

The microcontroller is the brain of a sensor node and oversees the operation of the node such as data processing, controlling all node components and communicating with other nodes. Almost every microcontroller family available in the market is unique: Some may be designed for speed and others for power efficiency. It is a matter of selecting the right microcontroller for the application. The microcontroller MSP430FR5969 is a holistic ultra-low-power system architecture for low energy budgets. The enhanced features of MCU enable energy optimization through a low power mode (LPM). The advanced timer features allow MCU operation with minimal energy requirements during the sleep mode with an automatic wake-up system using the watchdog timer (WDT).

In sensor applications, the MCU harvests 400 nA @ 32 KHz during LPM and 400 μA @ 4 MHz during the active mode. The WDT can generate a long interval time of a minute. This feature allows the EMU to store energy efficiently. In addition, during the LPM, the EMU transfers 99.99% of the harvested energy to a rechargeable battery or supercapacitor.

Figure 41 depicts the clock control in the microcontroller. The processing clock (CPU) is generated by a 1 MHz digitally controlled oscillator (DCO) turns off when the microcontroller goes into the low pwer mode, but the 32.768 KHz low-frequency clock remains online and generates a new *wake up* event every eight seconds. The microcontroller reduces energy consumption to less than $1\mu A$ during the sleep mode interval [75].

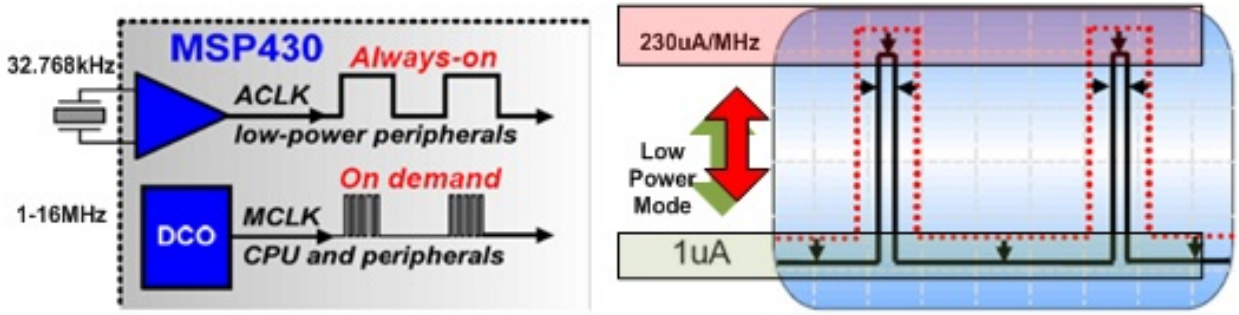

Figure 41: Energy-saving clock control.

5.4.2 FracBot USB communication

The chip FT230X is the communication interface between the computer and the sensor. The interface accesses the node readings and configuration parameters using the MCU UART interface, which is connected to the FT230X. Figure 42 shows the design of the software that connects, controls, and debugs the sensor. Moreover, the interface can also access the node in real time. During prototype development, the interface provides highly efficient way of debugging, controlling, and validating the node features. The FT230X is a full-speed USB IC bridge to UART interface,

which has a high throughput of 3 MBits/s, with low power consumption (8mA). The FT230X, which is compatible with Windows, Linux and Android, allows communication between the electronic device/sensor and software interfaces [76]. A diagram of the controller appears in Figure 43.

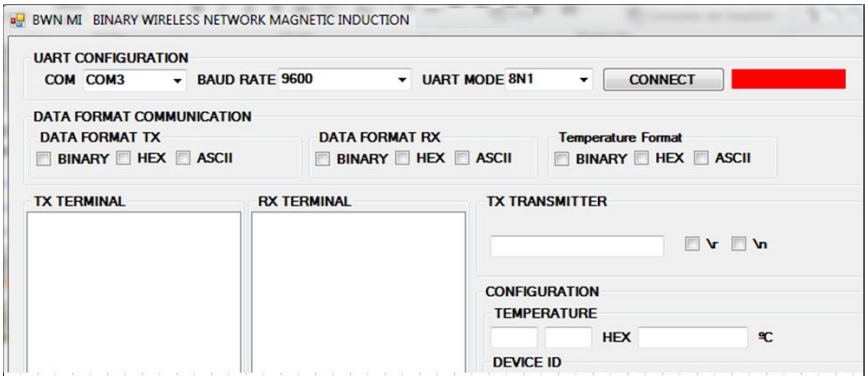

Figure 42: Software with USB interface.

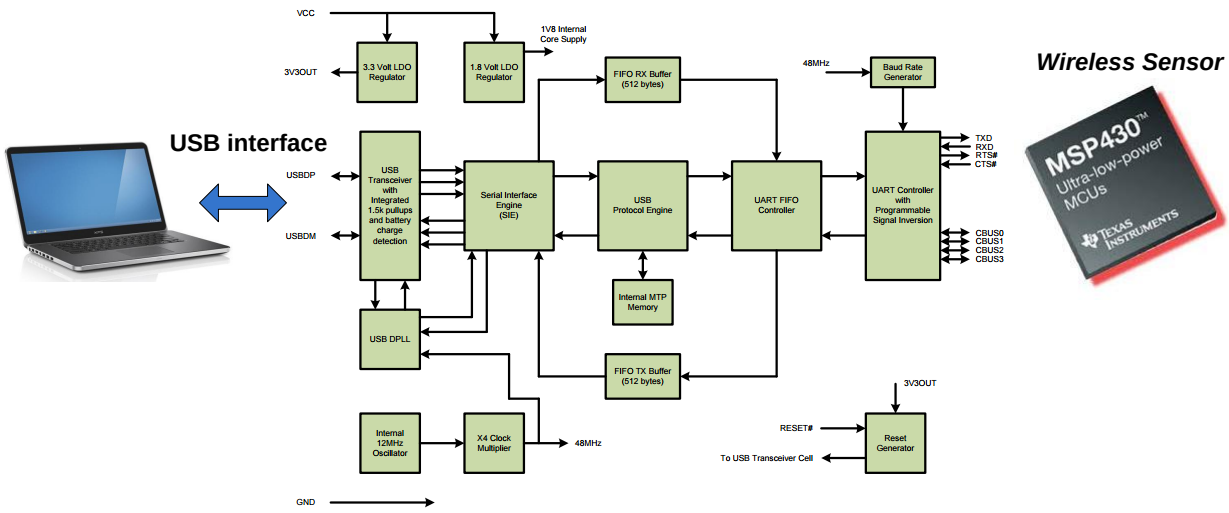

Figure 43: USB controller diagram.

5.4.3 Dual NFC Communication

The Dual NFC Communication consists of two interfaces which are transceiver and transponder. They are explained in the following subsections.

5.4.3.1 *Transceiver Interface*

The FracBot design is composed of dual NFC interfaces, a transceiver and a transponder. The NFC transceiver enables access from one FracBot to a neighboring FracBot and updates the temperature readings. The FracBot works as a MESH network, allowing node to collect the surrounding sensing data of neighboring nodes and to store all temperature readings and sensor parameters in an active tag. The NFC transceiver, TRF7970A, provides output Power of +20 dBm (100 mW) and has an important feature, a received signal strength indicator (RSSI), which enables the communication, detection, and position estimation of the FracBots.

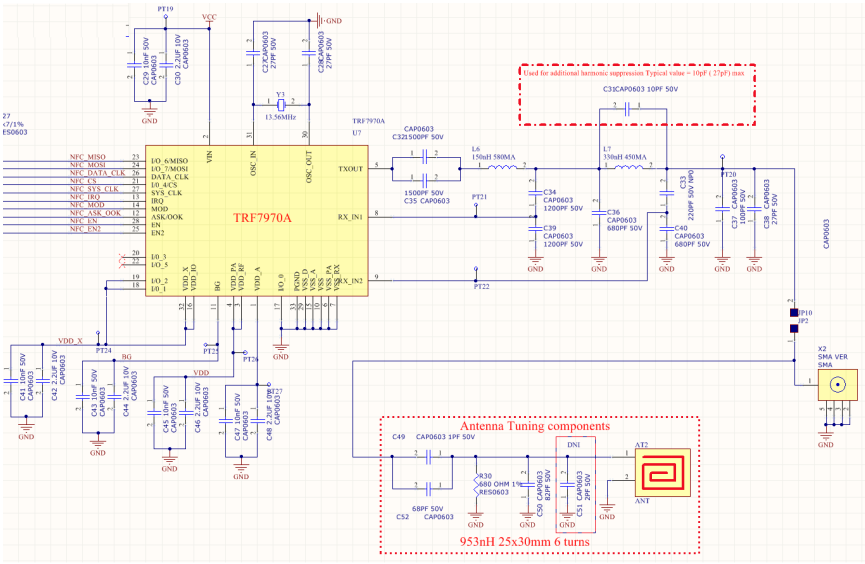

Figure 44: NFC transceiver.

Figure 44 shows an electronic schematic of the transceiver. In this application, the EMU configuration limits the voltage to 3.0 volts, which limits the transceiver maximum power output to +20 dBm.

5.4.3.2 *Transponder Interface*

The transponder is based on a dual-interface memory chip that can be accessed by I2C and through the NFC interface, shown in Figure 45. The chip allows the transceiver

to read, write, and store data in the memory.

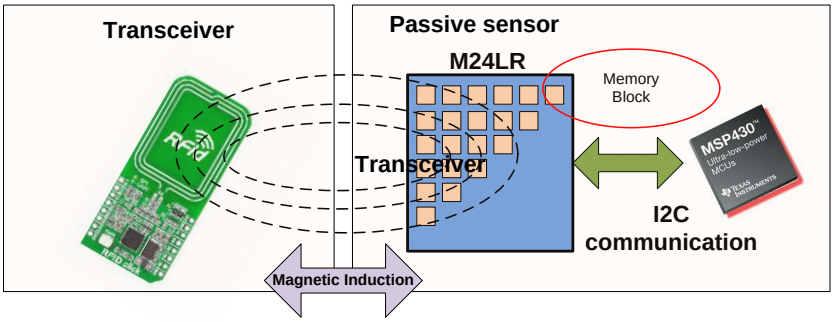

Figure 45: NFC dual-interface memory.

The second NFC interface implemented on the FracBot is the active tag (M24LR64) [77]. The NFC tag allows the transceiver to access the neighboring nodes and collect the stored data independent of their energy status because the NFC interface provides the required energy from the radiated power. One of the features of this NFC tag is to redirect the extra RF power to the EMU to be stored and used to operate the node later on in the case of the absence of RF power. Figure 46 shows the block diagram and the data flow between the *I2C* and NFC interfaces. The memory is segmented into two blocks, which provide separate independent memory regions for writing and reading the node parameters:

- Write MCU→Read Transceiver.
- Write Transceiver→Read MCU.

The data connection between the active tag and the transceiver is a half duplex controlled by the transceiver. The stored information in the node can be read/written by the transceiver of neighbor and then stored in its memory.

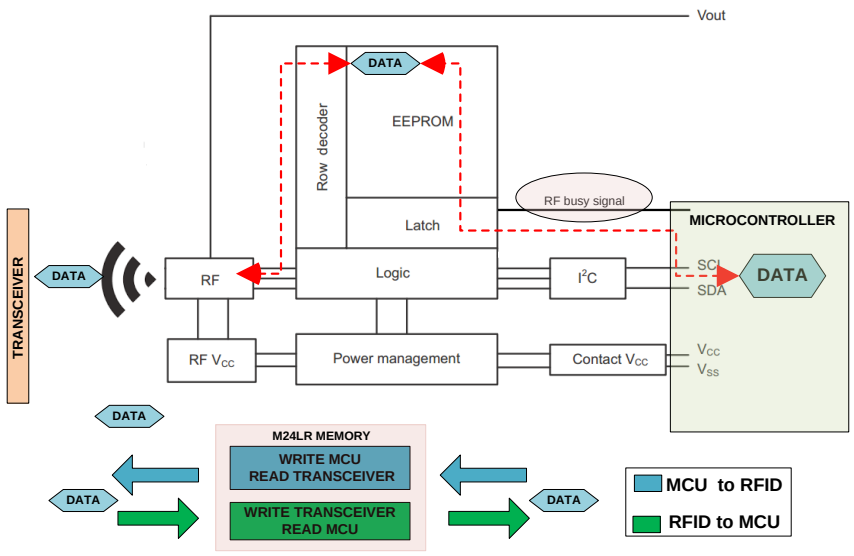

Figure 46: Active tag for microcontroller communication.

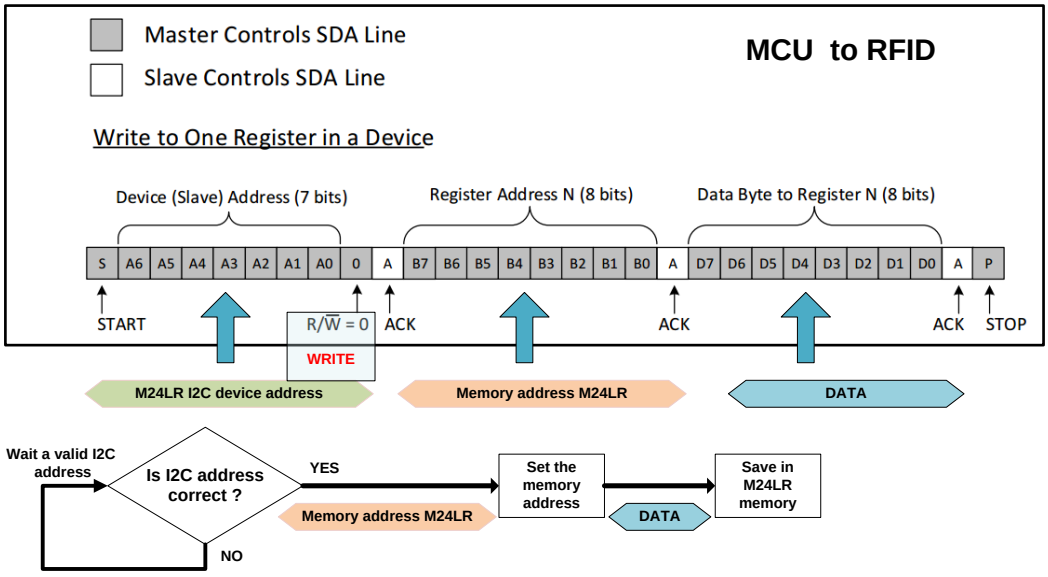

Figure 47: I2C data transfer process.

Figure 47 shows the write process, in which the MCU sends the *device*(*slave*) *address*. Once the device receives the correct address and answers with ACK(*acknowledge*), the MCU will send the address that will be used to store the data and wait for a new ACK to store the data. If the I2C address differs from slave address, the chip will

ignore all data flow in the I2C bus until a new *Start bit event*. With the data stored in the EEPROM memory of M24LR, the RF NFC logic can access this information according to the transceiver requirements [78, 79, 80, 81]. Figure 47 depicts the I2C communication protocol. The NFC circuit and I2C MCU cannot access the memory at the same time. Thus, to avoid simultaneous communication, chip M24LR provides a signal *RF busy* to indicate that RF is accessing the memory. The signal can be configured to start temperature acquisition or switch the the MCU to the active mode.

5.4.4 Energy-Harvesting Management Unit (EMU)

A fundamental feature of the FracBot design is the capacity to harvest energy in a severe environment. In FracBot applications, the design of the energy-harvesting process is based on the magnetic induction technique. Chip M24LR has an analog output pin that delivers the analog voltage $Vout$. When the magnetic field is sufficiently strong, the chip delivers the extra received RF power to the EMU. However, the limited power and unregulated voltage is not an ideal case for node operation. The microcontroller must work with stable voltage to avoid automatic reset at a low voltage level (*Brownout*). To stabilize the voltage, The node must have an energy-harvesting controller. The energy-harvesting process is based on two main components: an energy source (an M24LR-NFC transponder) and an EMU (chip of BQ25570: Nanopower Harvesting Energy Controller).

The BQ25570 is a chip that efficiently extracts microwatts (μW)/ miliwatts(mW). The chip can work with photovoltaic (solar) generator, thermal electric generators (TEG), or radio frequency (RF) or DC power supply with a voltage between 0.1 to 4.5V. The harvesting process starts when the voltage input is higher than 0.33V. After startup, the chip can harvest energy at a voltage higher than 0.1 V without collapsing the source [82].

In the node, the NFC tag chip *M24LR*, during communication with the EMU, transfers residual energy from the radiated power, which can be stored in a supercapacitor or lithium ion battery, the latter of which was used during the development stage to enable the development and testing of the hardware.

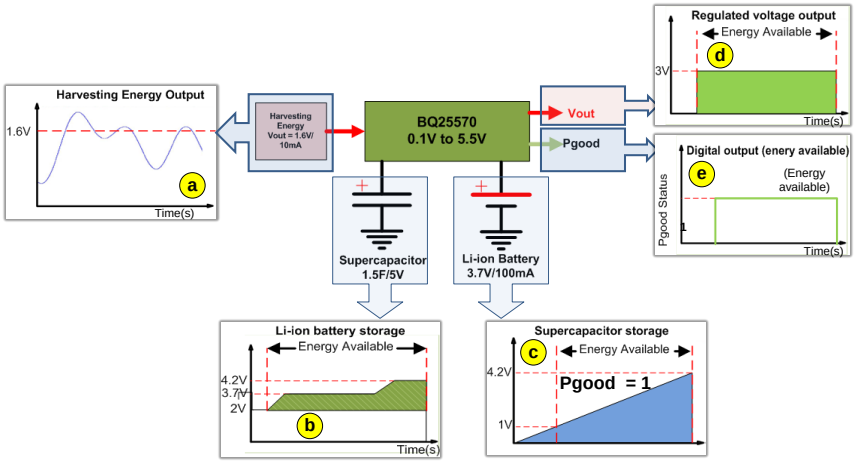

Figure 48: Flow process of energy-harvesting.

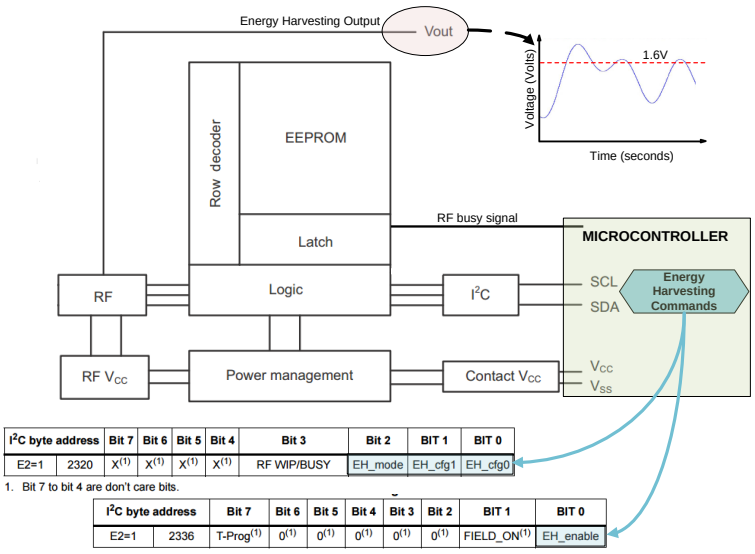

Figure 49: Setup of the energy-harvesting process.

Figure 48 describes all of the energy conversion stages [start from *a* to *e*]. In stage *a*, after the configuration process is executed by the MCU in NFC tag (M24LR), as

shown in Figure 49, and magnetic induction energy is available, the chip transfers the excess energy to the V_{out} pin. The voltage is unregulated, as shown in stage *a*. The harvested energy is controlled by an internal converter and transferred to a lithum ion battery or a supercapacitor based on the available configuration. While the available energy of a battery between 2.0 and 4.2V (a restriction based on the physical properties of a battery), that of a supercapacitor ranges between 1 and 5.0V [83]. The energy capacity of a battery is greater than that of a supercapacitor of a similar volume size. In addition, a battery can function in environments with a temperature range from -10 to 60°C (14 to 140°F) [84]. The energy capacity of batteries, however, is affected by temperature. Supercapacitors function in environments with a temperature range from -20 to 80°C (-4 to 176°F)[83]. Special supercapacitors can operate in higher temperature environments.

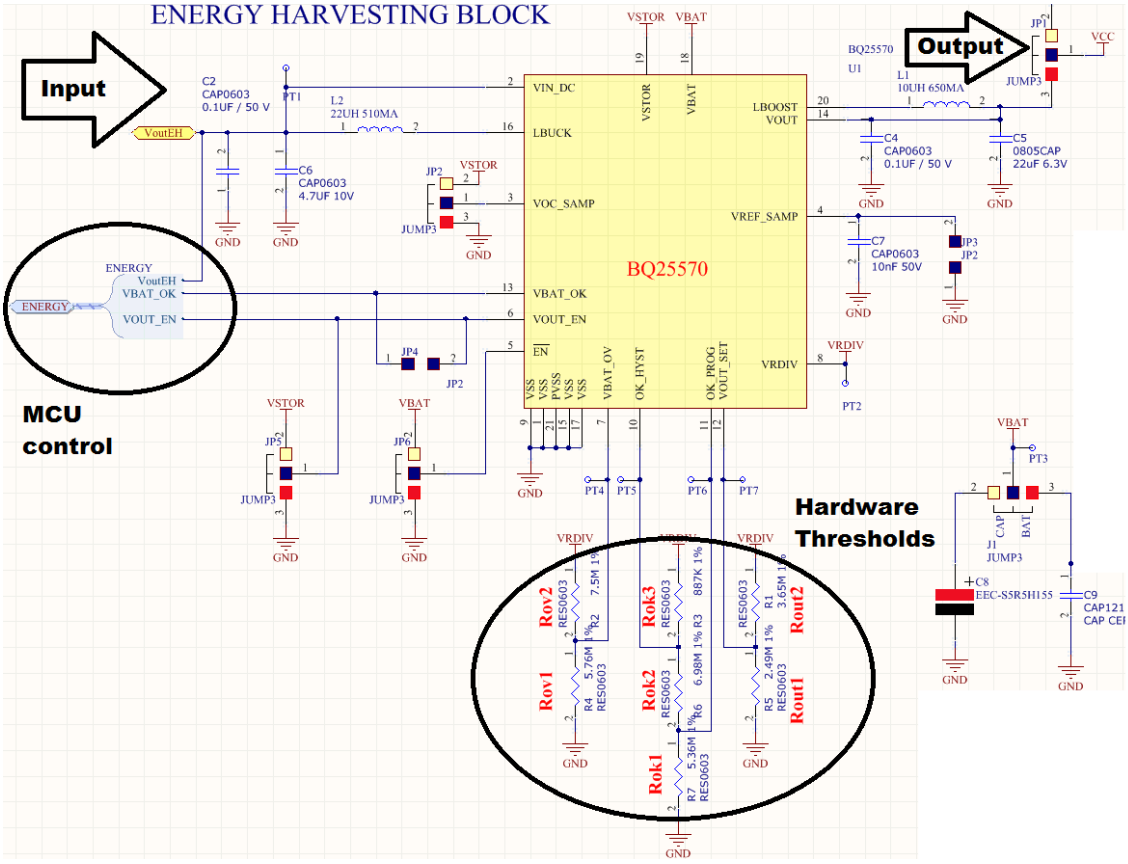

Figure 50: Schematic of an energy-harvesting circuit.

Figure 50 presents electronic schematic for the EMU. In this figure, we highlight MCU control and hardware thresholds. MCU control is responsible for generating the control signal of the MCU and indicating if energy is available. The hardware thresholds, such as the alert and output voltage threshold, are used to set up the electronic characteristics for the BQ25570. The output voltage is configured based on the individual voltage chip range, as shown in Figure 51. The minimum voltage to correct operation can be as high as 2.7V (minimum voltage of NFC transceiver) [76, 80, 85, 86].

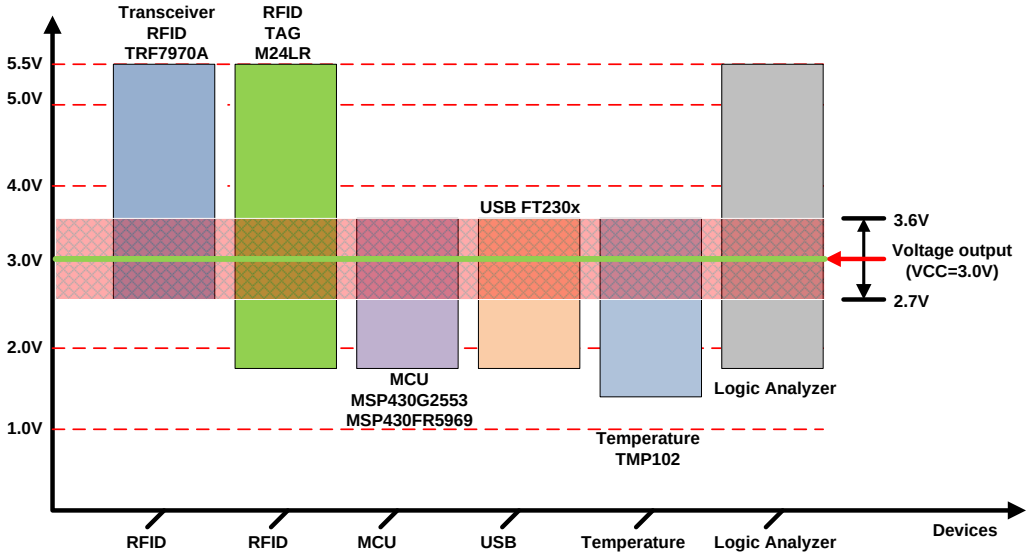

Figure 51: Integrated circuit voltage range.

Controller BQ25570 is configured to generate three volts, which guarantees the operation of all chips without exceeding the minimum and maximum voltage limits. Accordingly, all chips are able to operate within this voltage interval. Output voltage V_{cc} can be adjusted using resistors $Rout_1$ and $Rout_2$, shown in the following equation (54):

$$V_{cc} = [1.21 * (\frac{Rout_2 + Rout_1}{Rout_1})] \rightarrow Rout_1 + Rout_2 \leq 13Mohm \tag{54}$$

5.4.5 Temperature Sensor

The TMP102-Q1 chip is a highly accurate, high-resolution digital temperature sensor. The advanced features of this temperature transducer enable the sensor to alert the MCU if the temperature measurement exceeds predefined thresholds, as shown in Figures 52 and 53. The sensor, which can operate between -40 to $+125°C$ (-40 to $257°F$), can be configured to work in an autonomous mode with an alarm signal when the temperature reaches a predefined threshold. The thresholds can be remotely set up and updated according to design requirements. This characteristic allows us to implement an adaptive threshold that generates alarms only when the system detects a temperature change [85]. Also, it shows the autonomous operation of the temperature sensor. When the temperature crosses a predefined threshold for high or low temperature, the temperature sensor chip will automatically generates an alert signal that wakes up the MCU, which will access the TMP102 over an inter-integrated circuit ($I2C$) data bus, as shown in Figure 54.

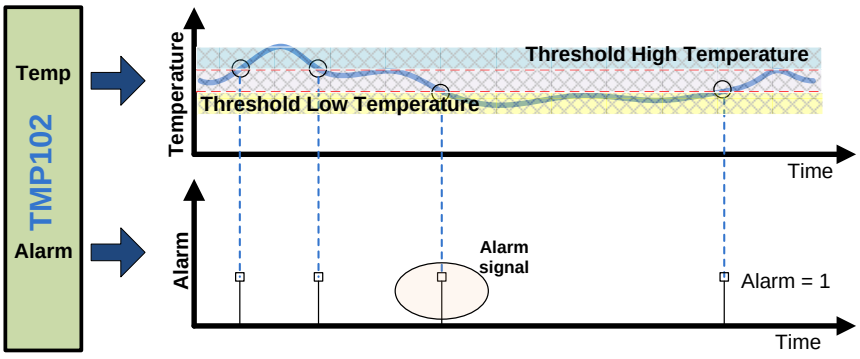

Figure 52: Automatic temperature sensor thresholds.

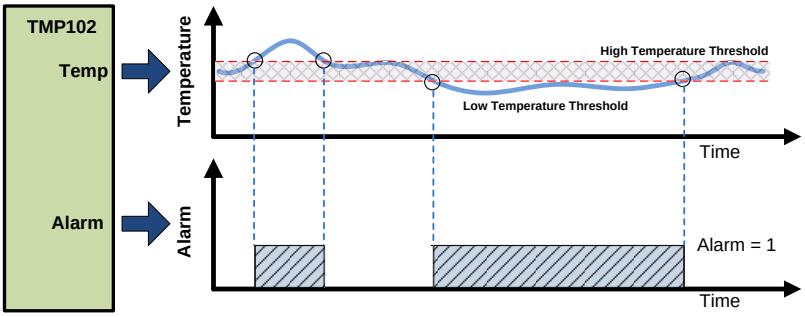

Figure 53: Fixed threshold temperature alarm.

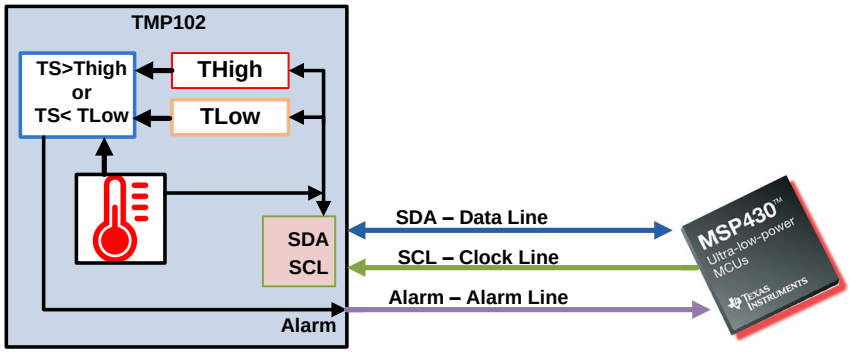

Figure 54: Temperature sensor TMP102.

The setup of the thresholds (high and low temperatures) requires conversion from a decimal format to a digital format and then transmission of data to the temperature sensor [85, 87]. Here, we show the conversion process:

- To convert positive temperatures to a digital data format: Divide the temperature by the resolution; the resolution of TMP102 is $0.0625°C$ ($0.1125°F$). Then, convert the result to binary code with a 12-bit, left-justified format, and MSB = 0 to denote a positive sign as in equations 55 to 61.

$$Temp_{binary} = \frac{Temp(°C)}{0.0625} \rightarrow Temp\ integer \tag{55}$$

Convert positive temperature example

$$Temp_{binary} = \frac{50°C}{0.0625} = 800_{decimal} = 320_{hexadecimal} = 001100100000_{binary} \tag{56}$$

- To convert the negative temperatures to a digital data format:

$$Temp = \frac{|NegTemp°C|}{0.0625} \tag{57}$$

$$Temp_N = Temp(TwosComplement) + 1 \tag{58}$$

For example,

$$Temp = \frac{|-25°C|}{0.0625} = 400_{decimal} = 190_{hexadecimal} = 000110010000_{binary} \tag{59}$$

Generate the two complements of the result by complementing the binary number and adding one. Denote a negative number by MSB = 1.

$$Temp_N = 111001101111 + 1 \tag{60}$$

$$Temp_N = 111001110000_{binary} \tag{61}$$

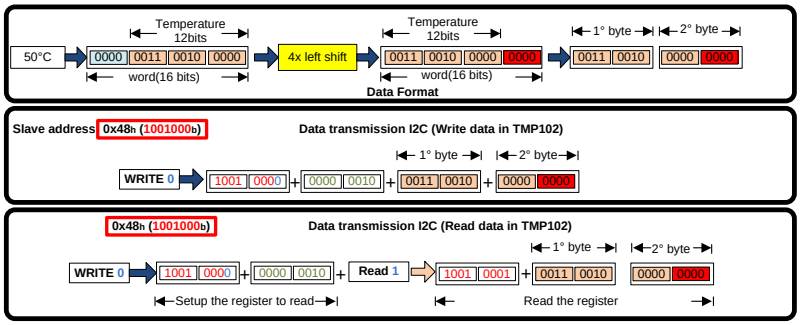

Figure 55: Data format and the I2C data frame.

Figure 55 shows that the temperature sensor and the NFC tag, which can be accessed individually when each device has a different hardware address, share the I2C bus. Figure 56 demonstrates an I2C waveform and hardware connection between the MCU and the temperature sensor. The waveform captured by a digital logic analyzer represents the temperature acquisition. The steps of the temperature read process are as follows:

- MCU send the slave address (write mode) and registers it.

  [Slave Address (write mode)][Temperature Register] = [0x90][0x00]

  This command will set up the sensor in the temperature mode.

- MCU sends the slave address (read mode) and receives 2 bytes.

  [Slave address (read mode)], [temperature byte 1], and [temperature byte 2].

  This command reads the temperature or control registers. The 16-bits data length must be interpreted according to the datasheet information.

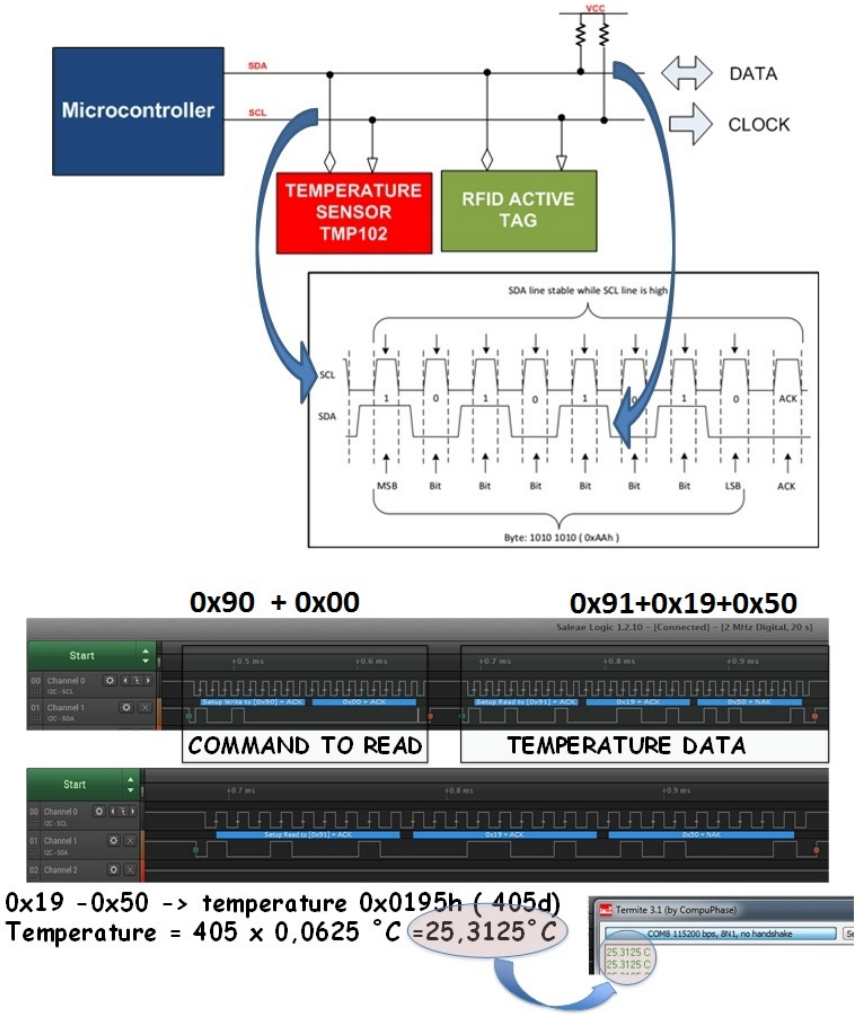

Figure 56: Multiple devices in the I2C bus.

5.5 NFC/MI Antenna Design used in FracBot

In this section, we describe the main characteristics of the NFC antenna, including the antenna design, the NFC antenna equivalent circuit, and resonance frequency of the transmitter and receiver antennas.

5.5.1 Planar PCB Antenna Design

For the optimal operation of NFC systems, the transceiver (reader) must radiate efficient energy to the tag (transponder). Thus, the antenna design of both the transceiver and the transponder needs to be tuned to the carrier frequency. Typically, the NFC antenna is designed in several geometric formats such as circlers, squares, hexagons or octagons in a spiral loop in order to build the coil antenna. The spiral square antennas of the NFC transmitter and the NFC receiver have to match chip requirements. Accordingly, we use a PCB planar square antenna to design the FracBot antennas, formulated in Eq. (62). The requirements of the NFC transceiver chip (TRF7970A) and the receiver chip (M24LR64) are to use antennas with an inductance of 1.5 μH and 4.95 μH, respectively.

$$L_{ant} = k_1 \times \mu_0 \times N^2 \times \frac{d}{1 + k_2 \times p} \tag{62}$$

$$d = \frac{(d_{outer} + d_{inner})}{2}, p = \frac{(d_{outer} + d_{inner})}{d_{outer} + d_{inner}}$$

where k_1 and k_2 are format constants depending on the PCB layout (for square, k_1=2.34 and k_2=2.75) [88], L is the inductance in Henry, d is the antenna diameter (mm), c is the thickness of the winding (μm), N is the number of turns, and $\mu_0 = 4\pi \times 10^{-7}\ H/m$.

5.5.2 NFC Antenna Equivalent Circuit

In the design of a transponder antenna, the antenna must be tuned to operate at long-, medium-, and short-range resonance frequencies. Originally, the NFC was designed to work in applications such as access control and electronic payments. However, the applicability of this technology has opened new frontiers in health monitoring as well as wireless communication in underground environments or applications in which EM cannot propagate. The resonance frequency of the LC circuit determines the distance range required by the applications. Figure 57 shows the electrical model used to represent the NFC receiver. Inductance L_x represents the PCB planar antenna, and C_x represents the capacitance. For the transceiver circuit, L_x and C_x are external components that, through adjustments, can improve the magnetic induction field. However, for the receiver part, the capacitor cannot be adjusted after the C_x is integrated in the M24LR64 chip.

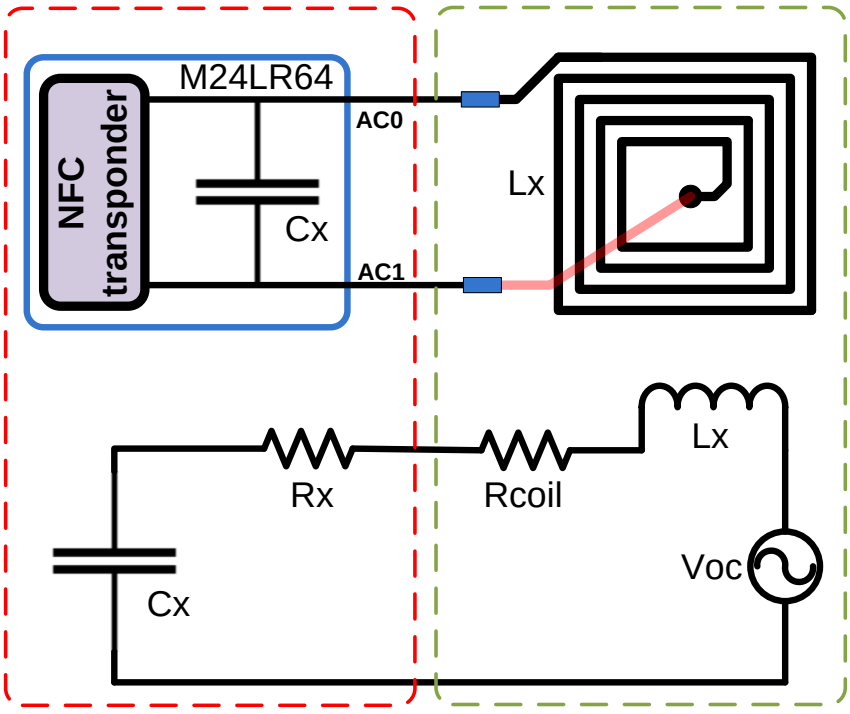

Figure 57: Electrical model of the NFC transponder.

Based on the electrical model shown in Figure 57, the resonance frequency is tuned to operate according to the distance that the FracBot needs to cover. The resonance frequency can be configured to work in different ranges to optimize distance requirements [88]:

- Long-range (LR) operation mode: Tuned between 13.6 MHz and 13.7 MHz.
- Standard short-range (SR) operation mode: Tuned between 13.6 MHz and 13.9 MHz.
- Short-range operation mode: Tuned between 14.5 MHz and 15 MHz.

5.5.3 Transceiver and Receiver Resonance Frequency

Table 1 shows the matching capacitance and resonance frequencies, the parameters that we used to design the antennas of the transceiver and the receiver. The antenna design for the TRF7970A and the M24LR64 chips requires antennas with calculated inductances of 1.5 μH and 4.95 μH, respectively. In our FracBot design, the antennas have actual inductances of 1.5 μH and 4.89 μH, respectively.

Table 1: Transceiver and transponder antenna parameters.

Parameter	Transceiver Antenna	Transponder Antenna
Antenna length (mm)	**41**	**30**
Antenna width (mm)	**65**	**40**
Inductance (Lx) (μH)	**1.5**	**4.89**
Coil turns	**4**	**11**
Capacitance (Cx) (pF)	**92.0**	**27.5**
Resonance frequency (MHz)	**13.5**	**13.7**
Resistance R_{coil} (Ohm)	**0.8**	**2**

Accordingly, we design seven PCB antenna models using a single planar PCB layer, as shown in Figure 58. In the fracBot design, the size and sensitivity of the antenna are primordial in the miniaturization process. The PCB planar antennas are

designed using software *STMicroelectronics* and the *eDesignSuite Antenna Design* [89]. The antennas are listed below:

1. Antenna with 5.29 μH, 12 turns, and a size of 30x40mm
2. Antenna with 0.958 μH, 8 turns and a size of 15x15mm
3. Antenna with 0.965 μH, 12 turns and a size of 10x10mm
4. Antenna with TRF 1.5 μH, 4 turns and a size of 41x65mm
5. Antenna with 0.940 μH, 2 turns and a size of 62x54mm
6. Antenna with 0.920 μH, 2 turns and a size of 72x54mm
7. Antenna (2D) with 1.5 μH, 4 turns, and a size of 41x31x31mm

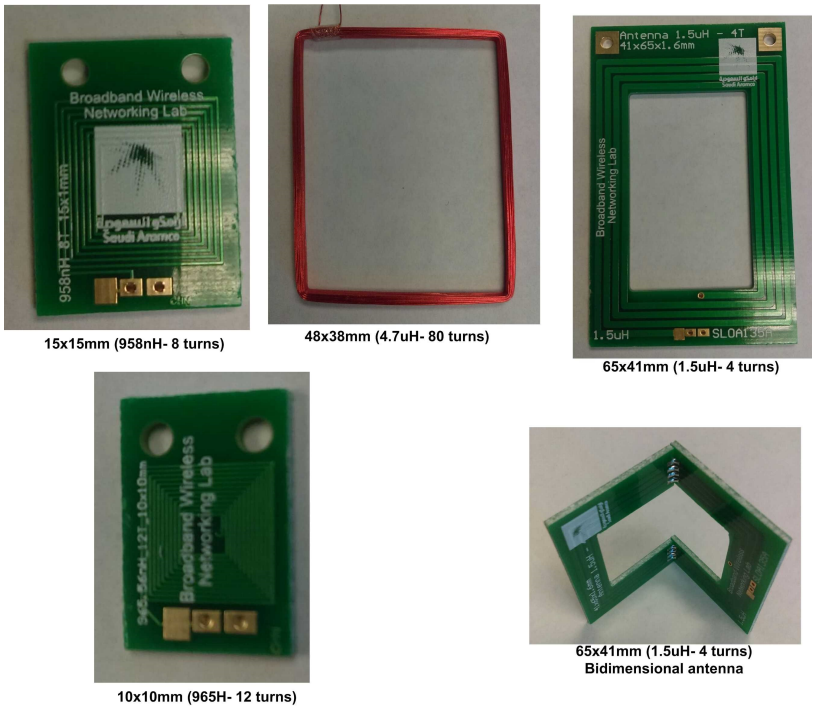

Figure 58: NFC antenna designs.

5.6 FracBot Prototypes

In this thesis, we design two type of FracBot nodes: a FracBot active node and a FracBot passive node.

5.6.1 FracBot Active Node

Using the FRAM technology, the FracBot active node has advanced functions and consumes minimal energy. The characteristics of the microcontroller used in the active node, MSP430FR5969 are very low energy, a high processing speed, and numerous interfaces. Since the microcontroller in active node controls the NFC transceiver (TRF7970A), its processing capacity is higher than that in the passive node [86] in three different operational modes:

- **NFC transceiver**

  In this operational mode, the TRF7910A is able to read other active sensors working in either the passive or active mode. The NFC transceiver can read data and measure the energy of the NFC signal to calculate the localization.

- **NFC tag/transponder**

  In this operational mode, the TRF7970A works in similar mode of M24LR(NFC passive node interface), but it is not able to read/write other transponders.

- **Peer to peer**

  In this operational mode, the TRF7970A works as an NFC relay mode and can establish a link between nodes.

Figure 59 (a) shows the PCB design of the board, Figure 59 (b) 3D visualization of the PCB design, Figure 59 (c) the top layer of the PCB board, and Figure 59 (d) the bottom layer of the PCB board.

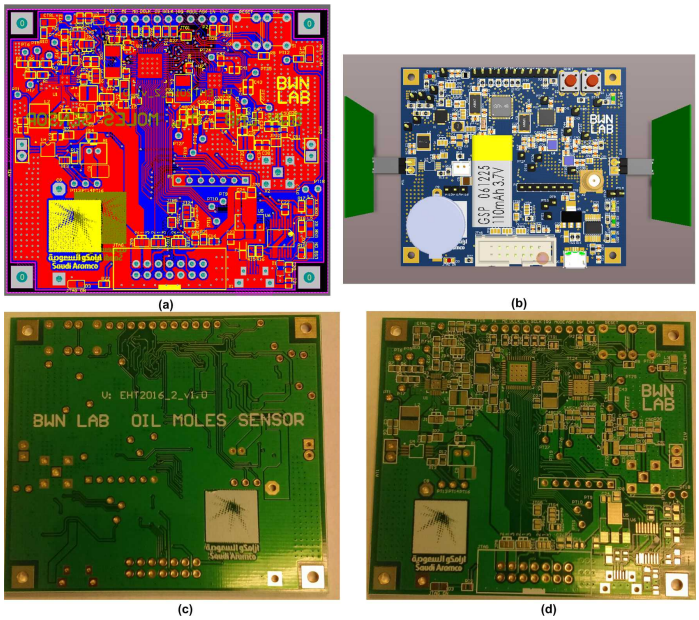

Figure 59: (a) Top layer of the PCB design, (b) the 3D PCB design, (c) the top layer board, and (d) the bottom layer board

Figure 60 presents a block diagram of the active node. The diagram shows the interconnection block of the node, which consists of the microcontroller, the JTAG interface, the energy harvesting circuit, USB communication, the temperature and the MI-transceiver, the latter of which connects the node in passive, active, or peer-to-peer mode. The JTAG interface allows us to program and access all variables of the code and stop the code from running at a pre-defined point (breakpoints).

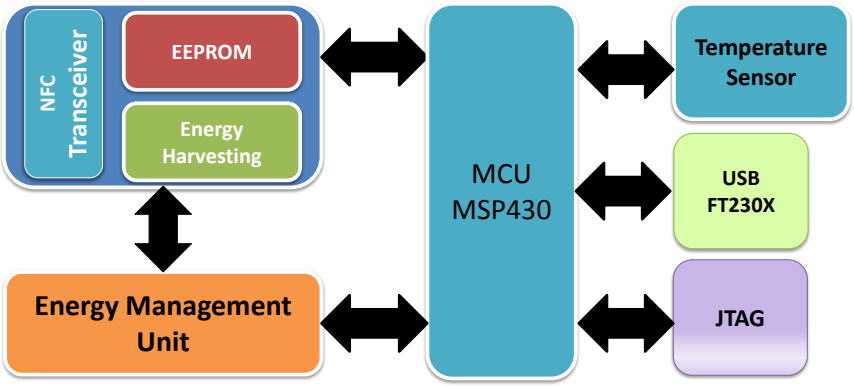

Figure 60: Block diagram of the FracBot active node.

Figure 61 shows the final design of the FracBot active node, which features the following characteristics: a 6-bit RISC CPU, an active mode of $100\mu A$/MHz, a standby mode of $0.4\mu A$, an off mode of $0.02\mu A$, low voltage from 1.8 to 3.6V, and communication interfaces I2C, UART, and SPI (dual interface).

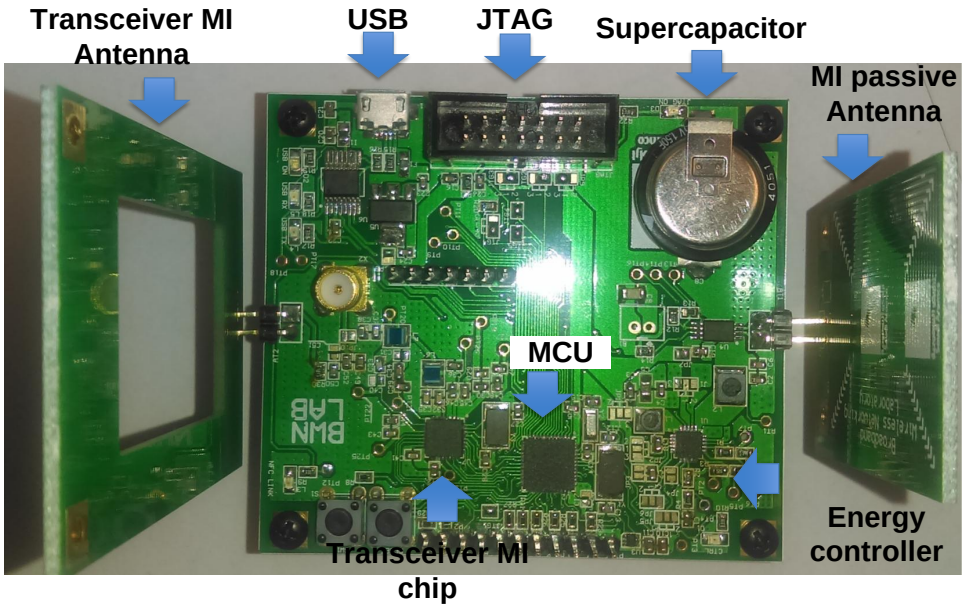

Figure 61: FracBot active node.

5.6.2 FracBot Passive Node

The FracBot passive node is a node that connects and transmits data to the transceiver, illustrated in its block diagram in Figure 62. The design of the node uses the M24LR chip. The NFC transceiver can access all of the NFC tag memory, change the configurations of the nodes and generate energy by harvesting energy output.

Figure 63 illustrates the passive node board in 2D and 3D. The 2D top vision of the board is displayed in Figure 63 (A). This side of the board has all of the traces and it is ready for soldering the electronic components. Every component has a designator identification mark. Figure 63 (B) shows the 2D bottom vision. Figures 63 (C) and (D) present the 3D vision of the board, which allows us to verify the spatial design, including the connector positions and component sizes.

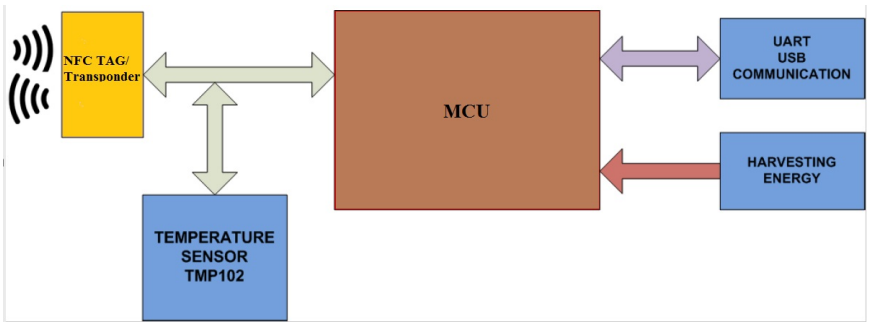

Figure 62: Block diagram of the FracBot passive node

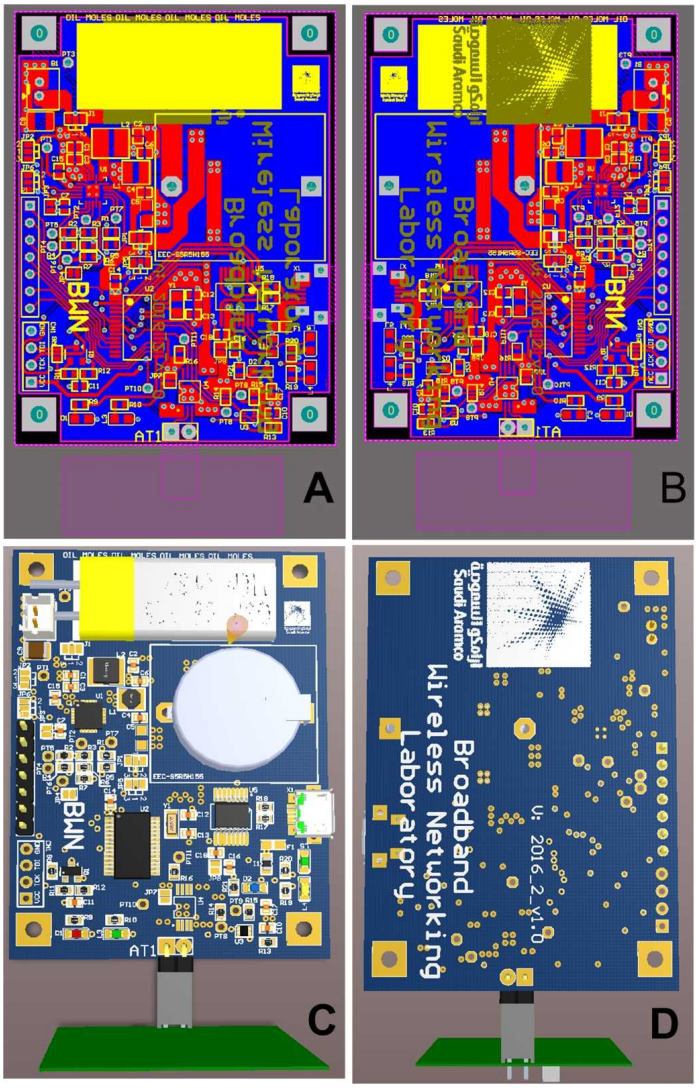

Figure 63: (A) Top layer of the PCB design, (B) the botton layer of the PCB design, (C) the 3D top layer, and (D) the 3D botton layer.

Figure 64 presents the prototype of the FracBot passive node, which shows all circuits and electronic components, which consist of the microcontroller (MSP430G2553), the temperature sensor (TMP102), the USB interface (FT230X), and the NFC active tag (M24LR64).

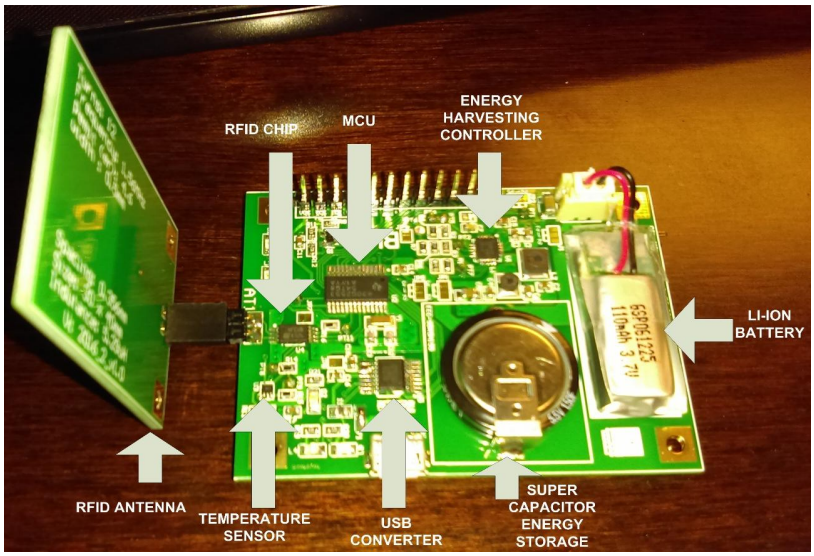

Figure 64: FracBot passive node.

5.7 Highlights

In this chapter, we proposed a novel prototypes of MI-based wireless FracBots for potential use as a platform for a new generation of WUSNs for monitoring hydraulic fractures and unconventional reservoirs, and measuring other wellbore parameters. We designed and developed the hardware of the MI-based wireless FracBots for short-range communication using near-field communication (NFC) as a physical layer combined with an energy-harvesting capability and ultra-low power requirements. We were able to realize these characteristics using cost-effective and commercial off-the-shelf components. We outlined the design requirements and implementation processes of the FracBot node platform and designed two types of FracBot nodes: a FracBot active node and a FracBot passive node. We designed seven types of antennas used

in the implementation and experimental processes and described the main characteristics of the FracBot antenna, including the NFC antenna equivalent circuit and the resonance frequency of the transmitter and receiver antennas. This design, which will operate in hydraulic fractures and oil reservoirs, is the first of its kind. Such nodes, however, are not yet commercially available, for they need to be designed to overcome limitations caused by the small size requirement and harsh underground environments. Accordingly, we designed the FracBot node as a platform for a new generation of WUSNs that can serve variety of purposes, provide flexibility, and allow for experimentation. This design is very specialized in terms of its communication layer, size, and energy source to overcome limitations caused by harsh environmental conditions and energy constraints. Under this conditions, the node is able to collect data from subsurface area, hydraulic fractures, and water/gas/oil reservoirs in real time. To realize this design, the steps of which are outlined in the fabrication process, we had to satisfy the restrictive design characteristics of the node: a long operation time, ultra-low power, an efficient communication layer, and an energy-harvesting capability.

CHAPTER VI

FRACBOT TESTBED: PERFORMANCE EVALUATION

While many intensive investigations have been theoretically conducted, little effort has been devoted to developing and evaluating a sensor node (FracBot) for underground environments that can confirm theoretical outcomes. In this chapter, we evaluate our FracBot nodes and network in a reservoir-like environment. We design the FracBot testbed, which consists of various media such as air, water, sand, and stone. One of the main results is that sand and stone media affect the performance of the FracBot which eventually degrade MI signal propagation and reduce the energy transfer. Thus, the evaluation of hardware enables us to understand the challenges, improve the electronic sensitivity, and optimize the minimum resources necessary to miniaturize the FracBot hardware.

An analysis of NFC/MI antennas provided in Section 6.1 and Section 6.2 presents an evaluation of FracBot propagation. Section 6.3 provides FracBot energy-harvesting performance. Section 6.4 presents the FracBot underground-like testbed and Section 6.5 summarizes the conclusions.

6.1 NFC/MI Antenna Evaluation

FracBot communication is based on NFC, and the antennas operate at 13.56 MHz. To implement the antennas design in this research, we use a planar PCB antenna, which allows node miniaturization. For the FracBot node, we use a single-layer planar PCB to design seven antennas, as detailed in Section 5.5.3. However, two designs- the transponder antenna (5.29 μH, 12 turns and size of 30X40mm) and the transceiver antenna (TRF 1.5 μH, 4 turns and size of 41x65mm)- provide the best match.

For the antenna tuning test, we evaluate the connection between the transceiver

board (NFC CR95HF) and the antennas, which are connected to a chip, M24LR64, on the transponder side. To test the matching between the antennas and the M24LR64, we establish a connection between the antennas with the transceiver board. When the antenna and chip match, the transceiver board blinks. The 15 x 15 mm and 10 x 10 mm antennas require a variable capacitor that adjusts the resonance frequency of the transponder (i.e., the antenna and M24LR64 chip).

Table 2 presents the characteristics of the antenna and the operational distances between the NFC transceiver and transponder. To ensure communication between the NFC transceiver board and the transponder, the NFC transceiver board transmits data to the transponder, and the data are written to the transponder memory by the control software of the NFC transceiver board with a data rate of 26 and 1.6 Kb/s.

Table 2: Antennas characteristics and distances between the NFC transceiver and the receiver.

Antenna Type	**Parameter)**	
	Inductance (μH)	**Distance (cm)**
Antenna 62x54mm	0.940	6.5
Antenna 72x54mm	0.920	7
Antenna 40x30mm	5.29	4.5
Antenna 15x15mm	0.958	2.2
Antenna 10x10mm	0.965	1.8
Antenna 2D 44x31x31mm	1.5uH	1 @ 45°

Figures 65 and 66 show the connection tests between the antennas and the NFC transceiver. it is evident that the bigger antenna is able to extent a longer distance-than the smaller one shown in Table 2. These tests, conducted in air, ensure the functionality of the antennas.

The desgin of all of the antennas satisfied the chip requirements descried in the datasheet. The antennas with dimensions greater than 50 x 50 mm exhibited the best performance. One of the designed antennas was a 2D antenna that does not provide good coupling. This antenna performs best when it is very close to the transceiver-

within 1 cm and at 45°.

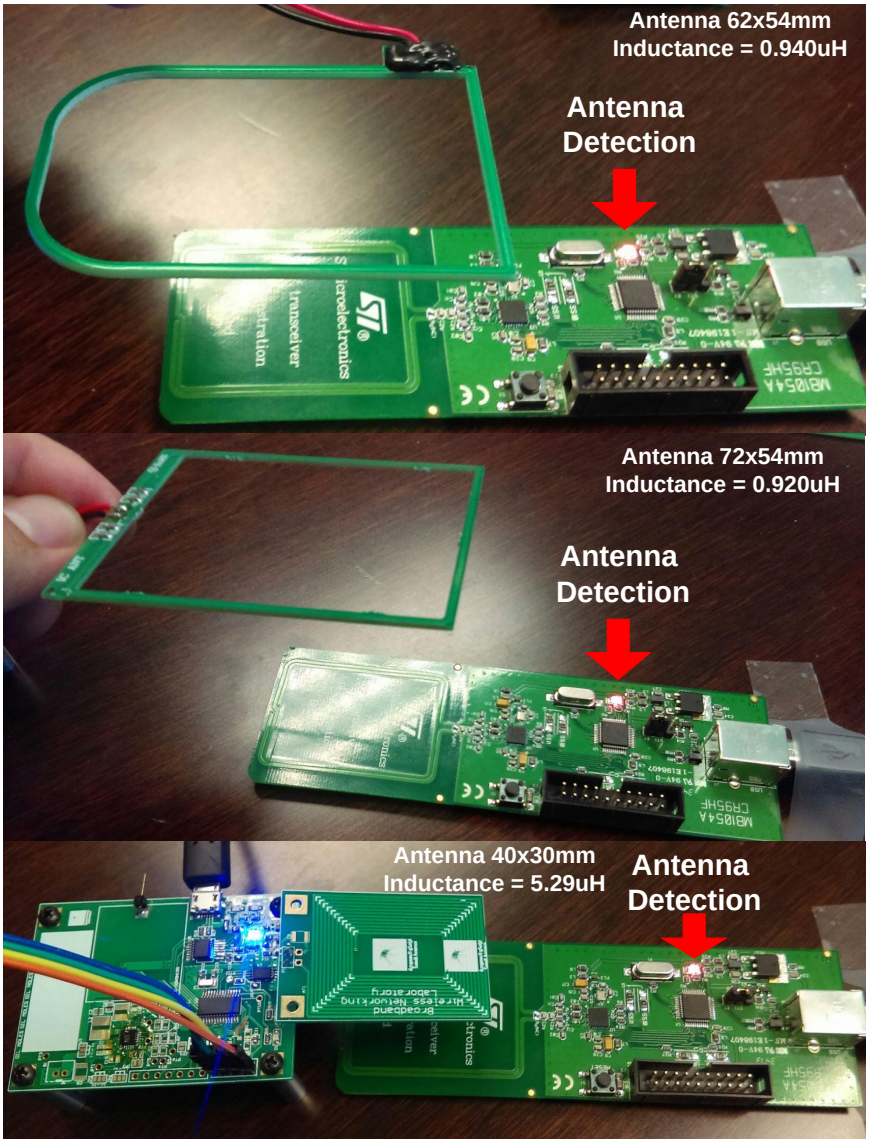

Figure 65: Antennas connection test 1.

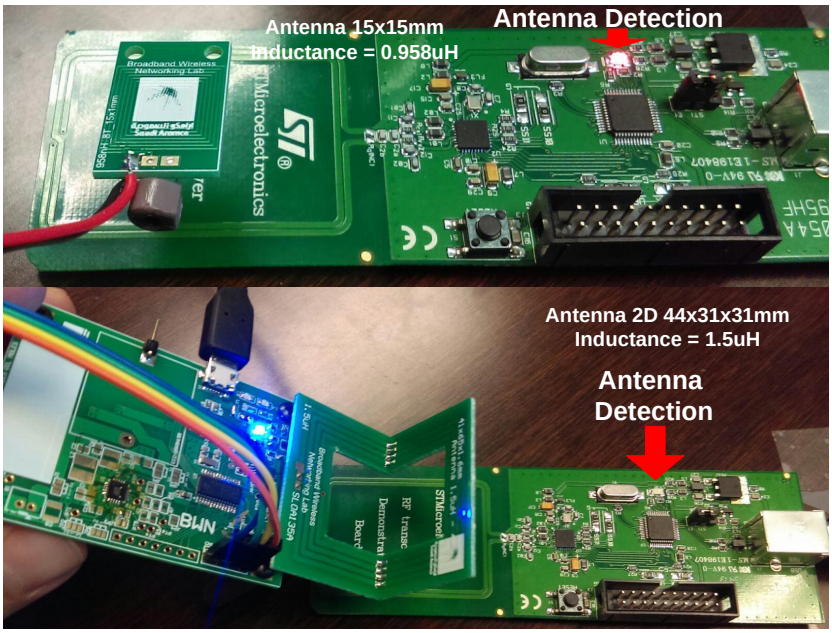

Figure 66: Antennas connection test 2.

6.2 FracBot Propagation Evaluation

In this section, we evaluate our FracBot MI propagation at 13.56 MHz. The analyses are based on received power measurements using the CXA Signal Analyzer N9000A (Agilent Technologies). In addition, we analyze the MI field generated by the transceiver with and without modulation (carrier only).

6.2.1 Experimental Setup

We measure and analyze MI signal propagation in the air and the influence of the antenna orientation on the received power. Figure 67 presents the schematic of the experimental setup and Figure 68 shows the actual setup in the lab. In this experimental case, we measure the MI interaction at distances between 0 and 25 cm and angles of 0, 30°, 60° and 90°, respectively.

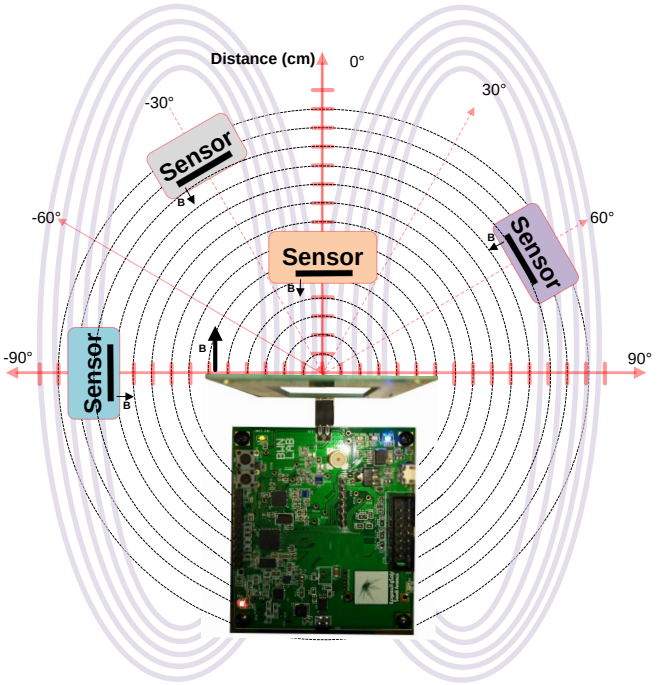

Figure 67: FracBot experimental setup.

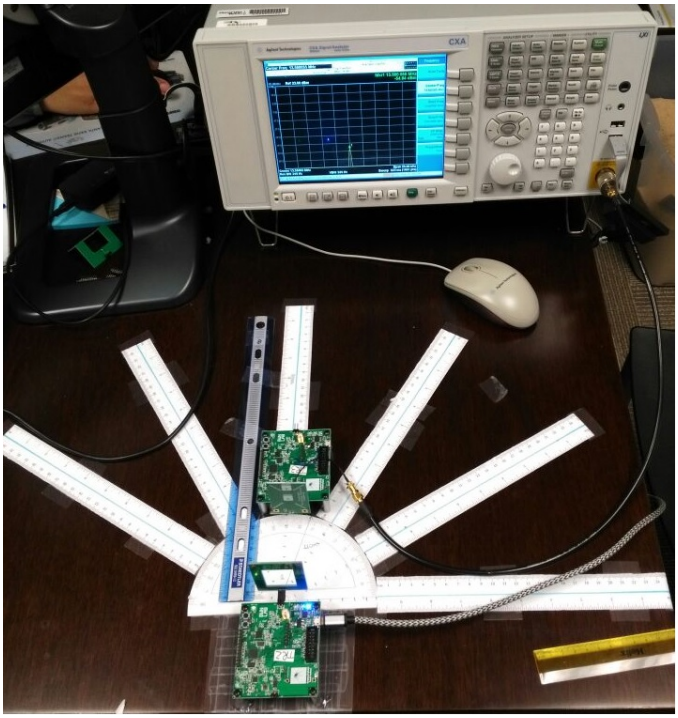

Figure 68: FracBot experimental setup in the lab.

Figure 69 illustrates the magnetic propagation and the antenna alignment. The theoretical sensor alignment occurs when the antenna alignment between the transceiver and the FracBot receiver is 0°. We perform the analyses in air, sand, and stone to compare MI signal propagation performance as a carrier only or a carrier with modulation.

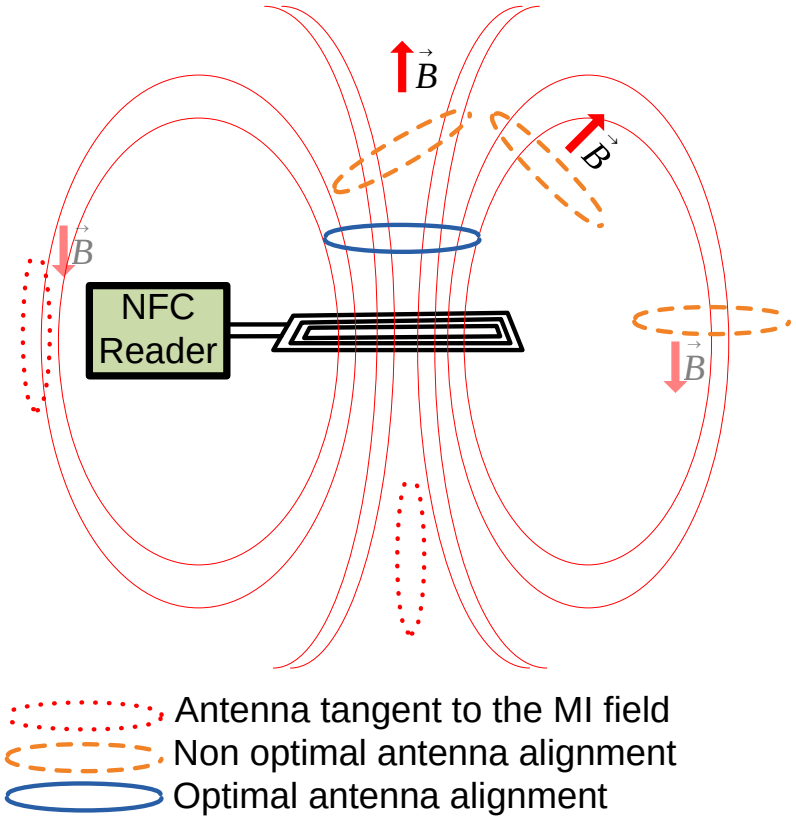

Figure 69: Power transfer and NFC transponder orientation.

6.2.2 Angular Analysis

One of the problems in MI-based communication is the orientation and the alignment between the transceiver and the receiver of the FracBots. In the angular analysis, we conduct measurements at 0, 30°, 60° and 90° angles. The results of distances between 6 and 25 cm, compared to those under 6 cm exhibit small variations. Figure 70-A shows the power analysis of the angular changes. For distances beyond 6 cm, the

angle between the transceiver and the receiver antenna does not affect the received power that much, only lower than - 2 dBm. Figure 70-B highlights the signal strength between -45 and -60 dBm, where concentrated power occurs beyond 6 cm in air. For the underground environment (in sand), the signal strength is between -50 and -75 dBm.

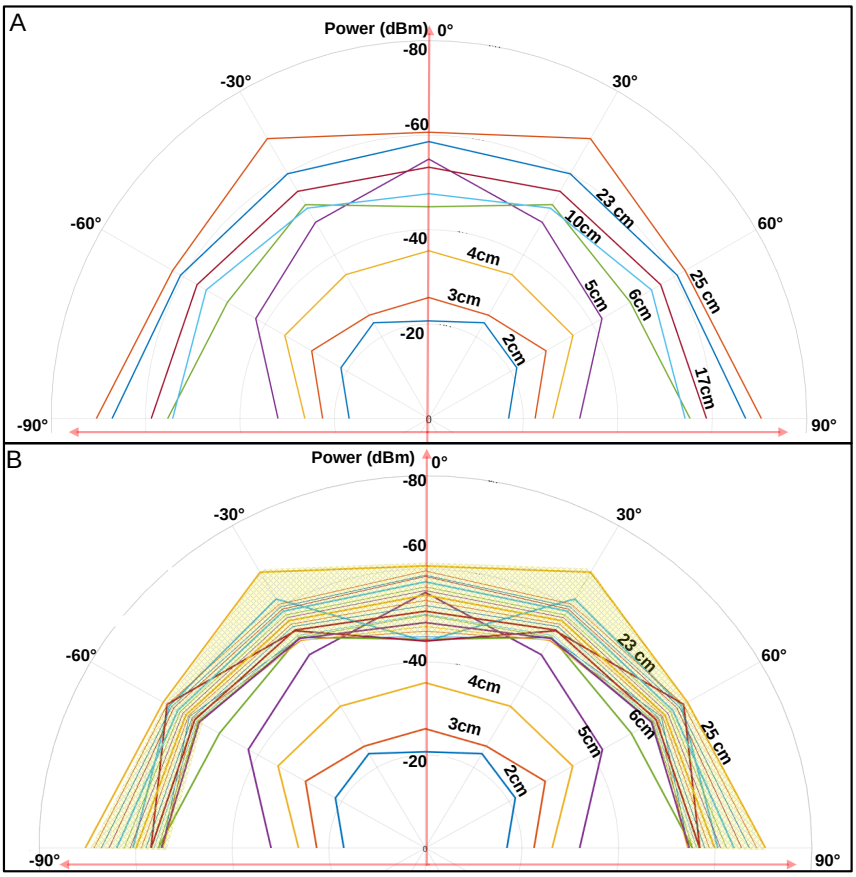

Figure 70: Angular plots of received power (air).

Figure 71 shows the angular analysis in an underground environment. The angular analysis demonstrates that the MI field radiated at 13.56 MHz can be detected omnidirectionally. When this characteristic is integrated with the RSSI measurement, it allows the FracBot Base station to estimate the position of each node and generate a 3D fracture map. Considering the energy required by the FracBot as described in Chapter 5, the FracBot MCU requires 50 ms to execute all reading tasks and store

them in the NFC tag. This task requires 33μW of the energy storage system. Considering the angular analysis, if the receiver is located at 23 cm or closer to the next FracBot hop, the node can operate continuously by harvesting energy of the MI field.

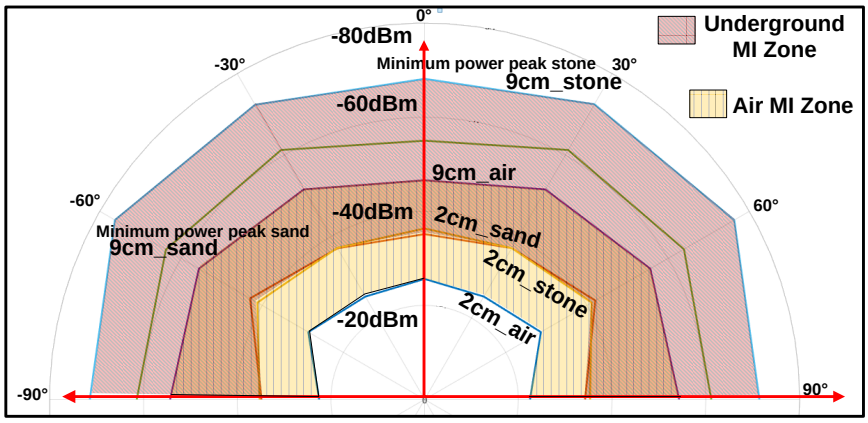

Figure 71: Angular plots of received power (air, sand/stone).

As a result, the received power in the region of 6-25 cm is around -50 dBm which provides sufficient energy to the FracBot every hour and enables it to send data within a time frame of 50 ms. However, beyond 25 cm, the received power will be less than -50 dBm, which is not sufficient to power the FracBot every hour. Therefore, the FracBot needs to harvest the required energy and send data within a time frame of 50 ms every 2 hours or more. With an MI signal strength lower than -50 dBm, the FracBot can work in an intermittent mode.

6.3 FracBot Energy-Harvesting Performance

The energy-harvesting capability of the FracBot ensures a balance between the harvested energy and the power requirements. The FracBot can generate 16 mW on average (1.6 V @ 10 mA) in the continuous mode. Although this energy will be used to operate the FracBot, the extra energy provided by the transceiver will be transferred to the EMU for later use as in the sensing task.

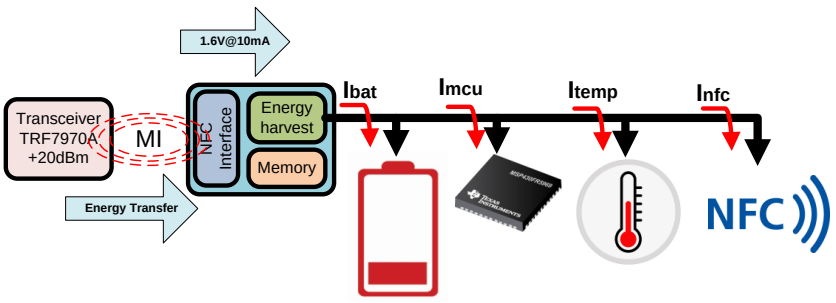

Figure 72: Block diagram of energy transfer.

The EMU controls the maximum current drained from the harvesting source through maximum power point tracking (MPPT) and avoids a collapes of the energy source. The high-efficiency energy conversion of EMU is up to 93%, which enables optimal energy extraction. Figure 72 illustrates the energy diagram of the sensor hardware. Compared to the MCU and temperature transducer, the NFC communication chip demands massive energy. During data transmission, the current required by the transceiver at half-power (100 mW) is 70 mA. Because of this power limitation of the energy-harvesting circuit, the transceiver (TRF7970A) in the FracBot node can work at only half-power (20 dBm). This current, however, is 20 times as high as that of the harvesting source. To satisfy this high demand for energy, the EMU switches automatically to a boost converter mode and harvests the required energy from the rechargeable battery or supercapacitor.

Table 3: Current requirements of FracBot electronics.

Circuit Status	**Current(mA)**			
	$I_{battery}$	I_{mcu}	I_{temp}	**NFC**
MCU(LPM)+Temp(active)	3.4	0.0004	1	0
MCU(LPM)+Temp(standby)	3.4	0.0004	0.1	0
MCU(active)+Temp(standby)	3.4	0.4	0.1	0
MCU(active)+NFC	-71.4	0.4	0.1	70

Table 3 shows the current required by the main components of the sensor. The

demanded energy during one hour for the complete node operation is 34.4 μW and the EMU is capable of harvesting 16 mW of continuous radiated power. Illustrating the operation of the sensor, Figure 73 shows the energy graph of the node operation, which the sensor acquires the temperature readings each minute and transmits the readings to a neighboring node every hour. The sensor node stays in LMP mode 99.9% of the time, and requires 4.2 μW of the energy in EMU. The MCU, however, must wake up every minute to check the energy status and acquire temperature readings. The MCU requires 50 ms to execute all reading tasks and to store them in the NFC tag, which requires 33 μW of the EMU. Because of the limited amount of radiated energy in real environments, the FracBot is designed to establish communication with the neighboring node every hour. Once the connection is established, the node transmits the readings and parameters. It takes the node 0.5 seconds to read/write the memory sector of the neighboring node, which requires 15 mW.

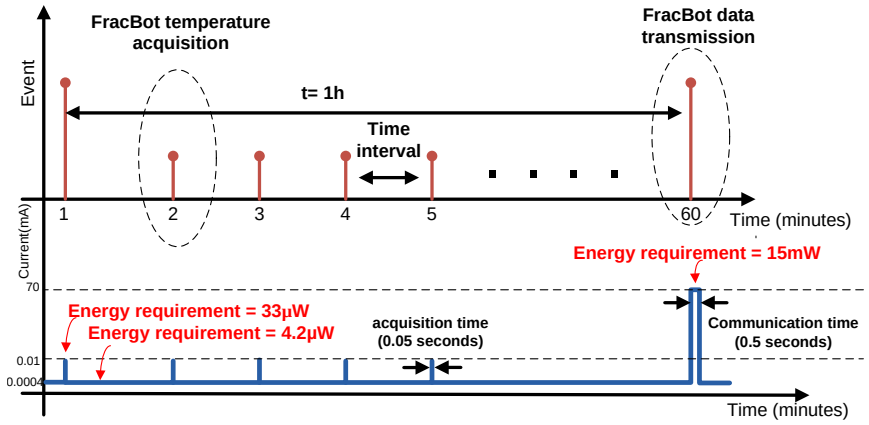

Figure 73: Block diagram of energy transfer.

6.4 FracBot Underground-like Testbed

To validate the performance of our FracBot nodes, we develop a physical underground-like testbed that consists of a plastic container holding water, sand, and stone, illustrated in Figure 74. The setup consists of various laboratory underground conditions,

including dry soil, wet soil, stone and dry soil with stone. The testbed environment allows the positioning of the FracBots to a depth of 14 cm with a variable distance between the nodes. This adjustment allows changes to the experimental conditions and evaluation of the FracBot nodes performance. Using the spectrum analyzer, illustrated in Figure 75, we measure all characteristics of the MI circuits, including MI propagation and antenna tuning.

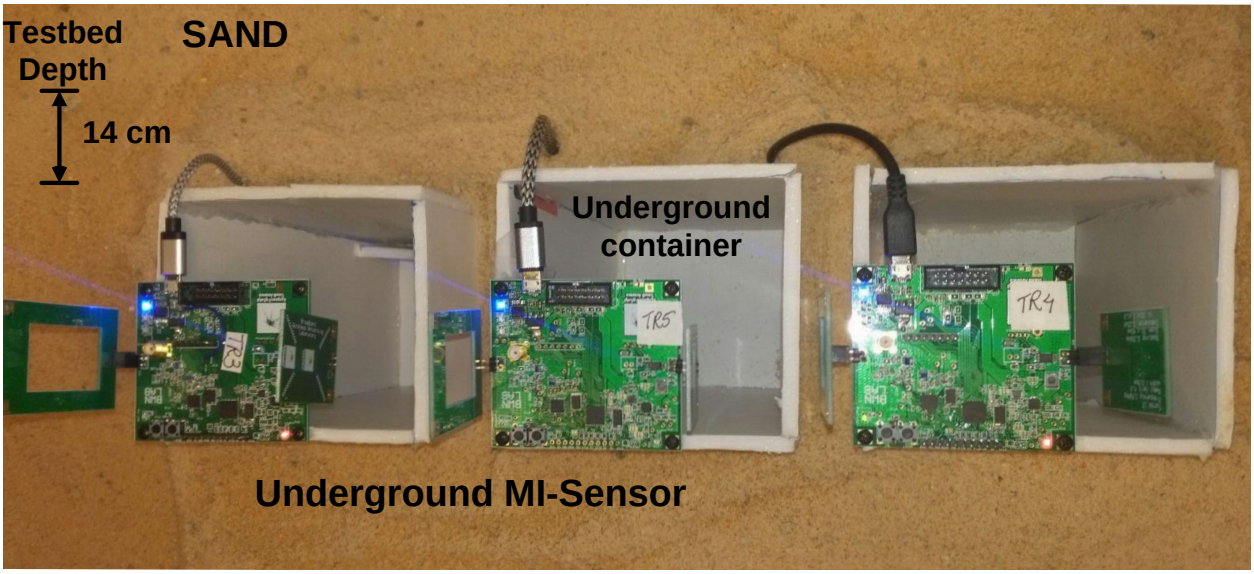

Figure 74: Underground testbed of the FracBot.

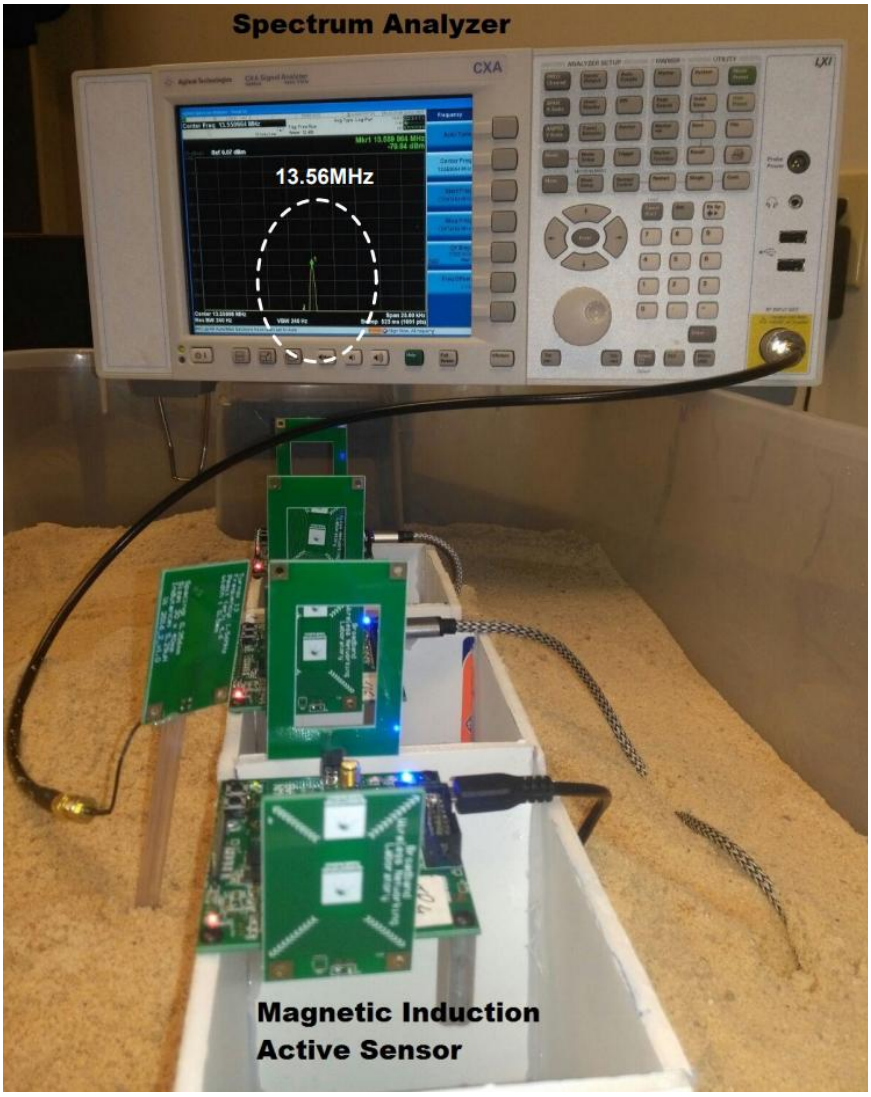

Figure 75: Underground testbed of the FracBot with the spectrum analyzer.

6.4.1 Modulation Effects

Standard NFC communication operates in a 13.56 MHz carrier with modulation of ASK 10% and ASK 100% (OOK), illustrated in Figure 76. In our testbed with underground environment properties, the data transmission error for ASK 10% is over 70% while that for the OOK is over 32%. We test the data transmission error by sending 1000 packets with length of 48 bits from the transmitter to the receiver. By counting the received packets at the receiver, we figure out the data transmission

error. Although this modulation affects power transfer, one feature of the FracBot is that it transmits pure energy only if no data are ready to be transmitted via hop-by-hop fashion through the MI field. The transceiver (TRF7970A chip) can enabl or disable the modulation control that switches the OOK on and off, illustrated in Figure 77. Figure 78 presents the signal strength for distances of 0-16 cm. In this analysis, we compare the energy strength between the transmitting carrier of the transceiver and a carrier with NFC modulation. When the FracBot operates in the energy transfer mode (i.e., an MI signal without modulation), energy transfer improves by 2 dBm in the air medium. Signal attenuation in sand and stone media, however, is 20 dB stronger than that in air medium for a distance lower than 8 cm. Interestingly, energy transfer of distances of more than 10 cm in the air and sand media has the same amount of power.

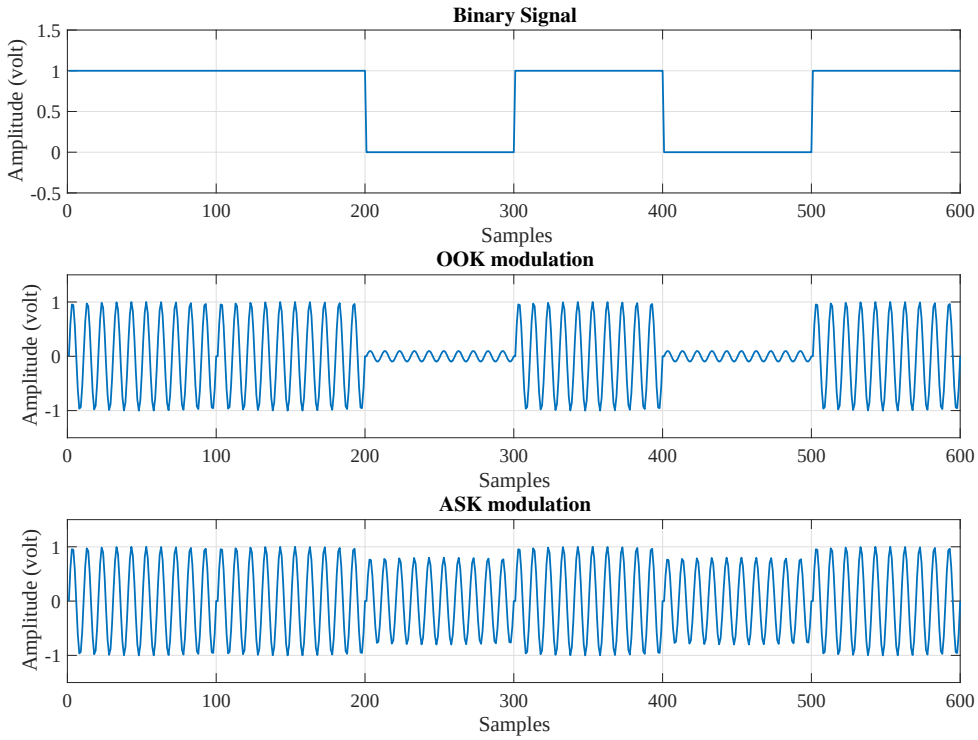

Figure 76: Input data and ASK 10% and 100% (OOK) modulations.

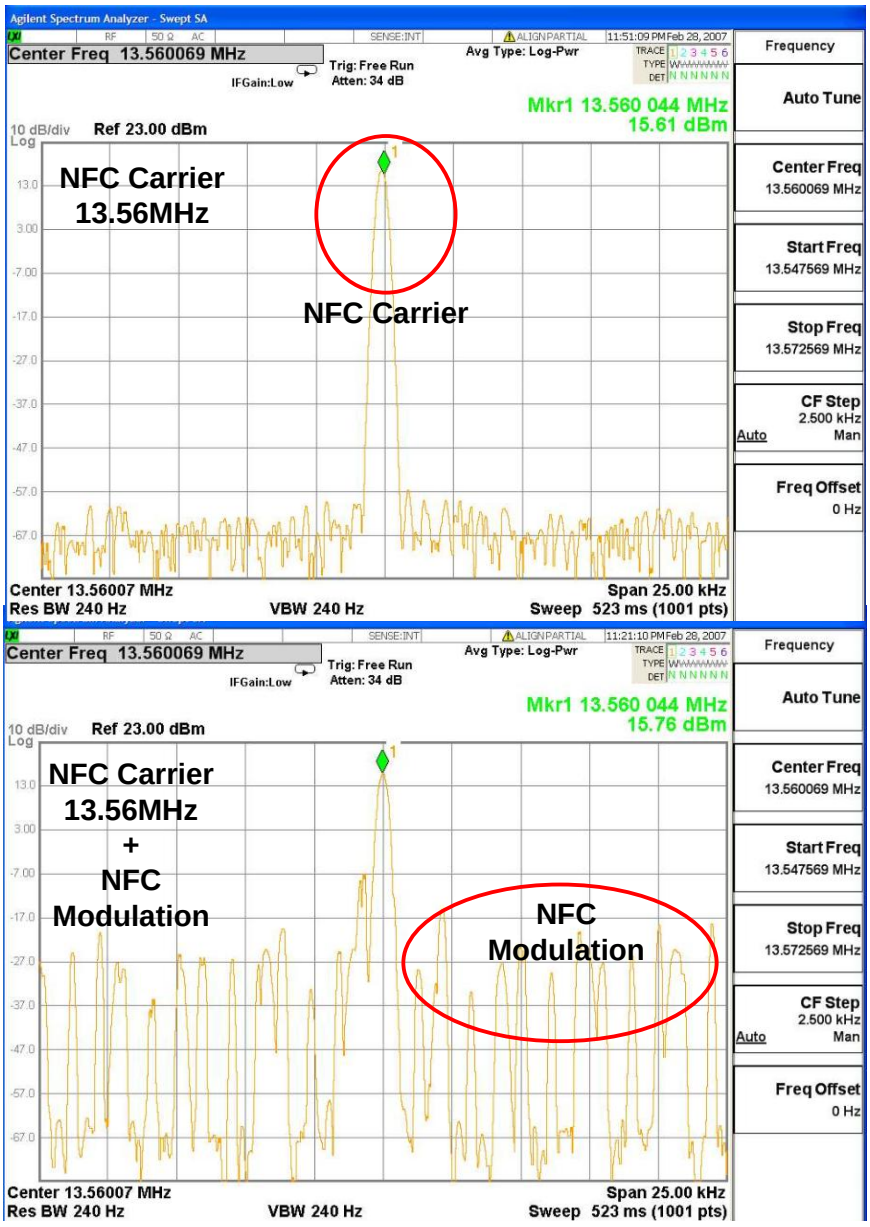

Figure 77: Measured received power.

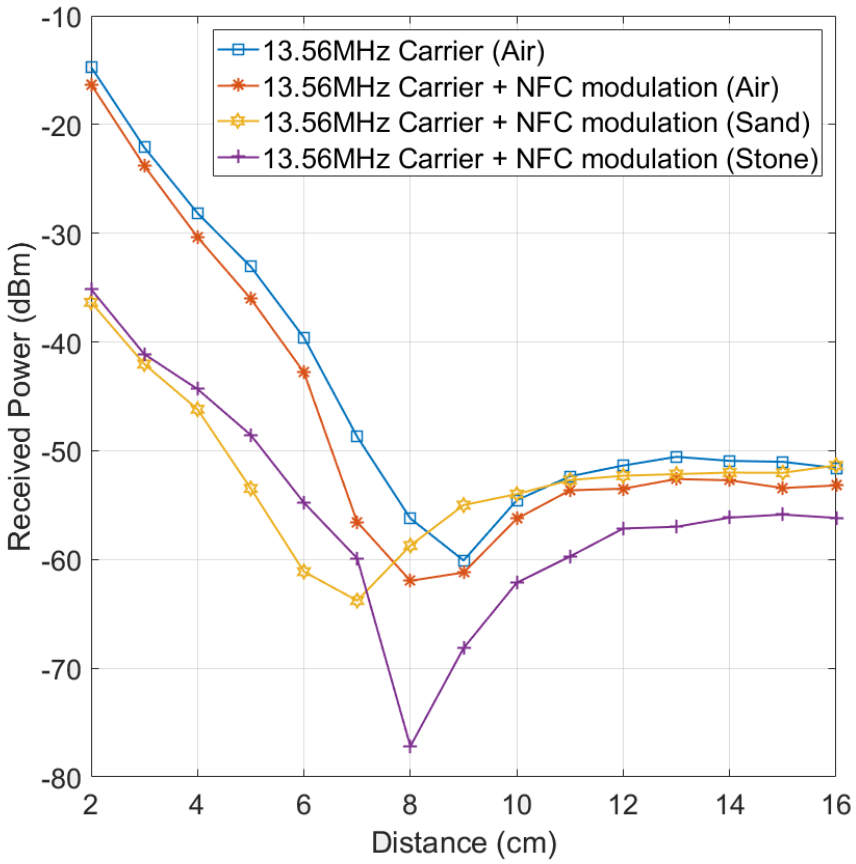

Figure 78: Received power analysis (air, sand and stone).

6.4.2 Transceiver and Transponder Matching

Using the parameters listed in Table 1 in Chapter 5, we simulate the frequency response of the transceiver and receiver antennas. Figure 79 depicts the antenna response with normalized gain. The transceiver is tuned at 13.56 MHz and the transponder at 13.7 MHz. In compliance with the range standards mentioned in Section 5.5.2, the FracBot is tuned to operate in the long-range mode with a maximum gain in the resonance frequency interval of 13.5 to 13.7 MHz. Operating in the long-range mode is highly desirable when the FracBot works underground since the underground environment properties will affect the matching circuit which will change the resonance frequency. Thus, a long range of resonance frequencies is required.

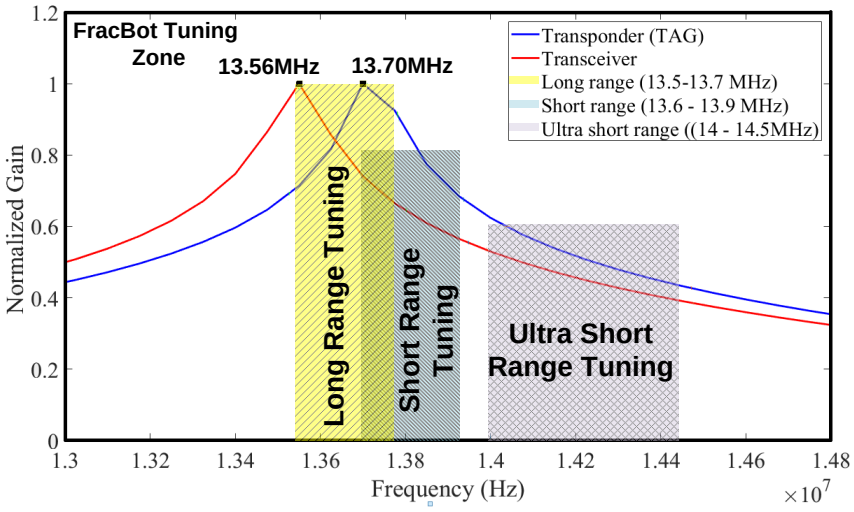

Figure 79: Frequencies responses.

6.4.3 Communication Link Evaluation

Figure 80 shows the setup used in the communication test. FracBot A connects the NFC tag to the transceiver of FracBot B. The FracBots execute one temperature acquisition each minute and one communication every three minutes in a laboratory. For test purposes, the adjustable interval time can simulate the data transmission of long periods in a short time. The FracBots employ NFC technology, but since they are designed to work in air, a reliable reference test and data performance analysis in air is necessary. The FracBot is tested to communicate in air and with a sand barrier.

Table 4 shows the experimental performance for ASK modulation in 10% and 100% (OOK) and data rates of 1.6 and 26 kbit/s. In an underground environment, the modulation OOK with 1/256 pulse position coding at a (data rate of 1.6kbit/s), compared with that at 26 kbit/s, reduces the transmission error. In stone, however, ASK modulation does not work for both rates because of high attention but OOK modulation works with a transmission error higher than that in sand for both rates. Previous research in underground communications shows 10 MHz as an optimal operating frequency with a data rate of 1 kbit/s. The low data rate is a consequence

of the high loss posed by the underground environment, volumetric water content, and depth [61]. To evaluate the communication link between FracBots, the nodes are positioned 5 cm apart from each other, illustrated in Figure 80 because the sensitivity of the transponder chip (M24LR64) is limited to -50 dBm for data communication. At 5 cm, the signal strength is -50 dBm, but beyond that, the signal will degrade, and communication will not be possible, shown in Figure 81.

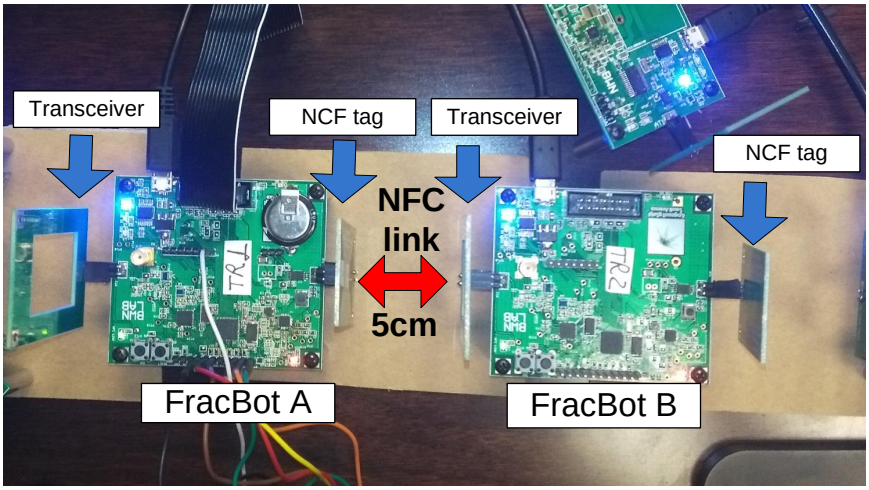

Figure 80: FracBot node communication.

Table 4: Experimental performance of the ASK and OOK modulation.

Environment	Modulation	Data rate (kbit/s)	Error (%)
Air	ASK	26	2
Air	OOK	26	1
Sand	ASK	26	70
Sand	OOK	26	78
Sand	ASK	1.6	40
Sand	OOK	1.6	32
Stone	OOK	26	87
Stone	OOK	1.6	58

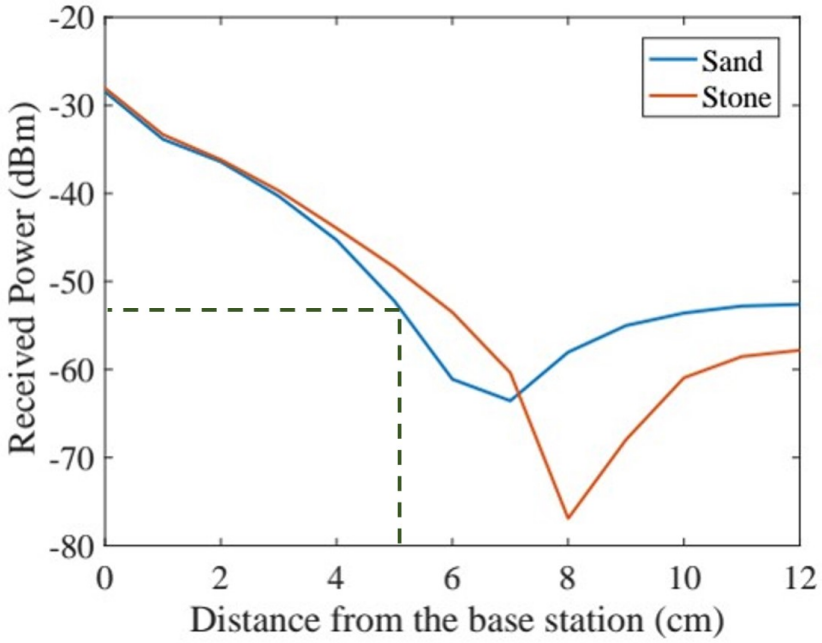

Figure 81: Underground signal strength between two FracBot nodes

6.5 Highlights

This chapter presented an evaluation of the FracBot node and the NFC/MI antenna in air, sand, and stone media. One of the main results is that the mismatch between TX and RX antennas increases as a result of the effects of sand or stone media. Thus, to overcome a mismatch resulting from an inhomogeneous environment, the adaptive-frequency feature or advance matching circuit design shall be incorporated into the optimized design of the FracBot. This feature will allow optimal energy transfer and a reliable communication link through sand and stone media. The FracBot features a very efficient energy-harvesting circuit that is capable of collecting 16 mW of energy under continuous radiated power while the actual energy consumption of the node is 34.4 μW and shows the FracBot can operate perpetually with minimal energy-radiated conditions. Also, the FracBot can establish at communication link and transmit data using modulation ASK with a data rate of 1.6 kbit/s. The minimum

receiver sensitivity of the current MI system must be -70 dBm, based on experimental measurements. Sand and stone media affect the performance of NFC antennas, which eventually degrade MI signal propagation and reduce energy transfer. Since the design of our FracBot entails the use of cost-effective and commercial off-the-shelf components, we experience a number of restrictions in the design and analysis. For example, the NFC chip does not allow the configuration of the data rate and sensitivities that prevent us from conducting extensive analysis on the communication functionality of the FracBot. Hardware development should lead to a better understanding of the environmental challenges, improve the electronic sensitivity and optimize the minimal resources necessary to miniaturize the FracBot hardware. These experiments and testbed analysis help us determine the requirements for design of an optimal MI system that operates in ultra-low energy requirements.

CHAPTER VII

CONCLUSIONS

In this thesis, we designed miniaturized wireless sensor systems for mapping hydraulic fractures, monitoring unconventional reservoirs and measuring other wellbore parameters. We call these devices FracBots (Fracture Robots), an extension of RFID (Radio Frequency IDentifcation) tags that realize WUSNs for mapping and characterization of hydraulic fractures in unconventional reservoirs. This miniaturized transponder system is fully integrated MI-based FracBots (WUSNs) that enable reliable and efficient wireless communications in underground oil reservoirs for performing the in-situ monitoring of oil reservoirs. This is very crucial for determining the sweet spot of oil and natural gas reserves. To this end, we have contributed in four areas as follows: first, we developed a novel cross-layer communication framework for MI-based FracBot networks in dynamically changing underground environments. The framework combines a joint selection of modulation, channel coding, power control and a geographic forwarding paradigm. Second, we developed a novel MI-based localization framework that exploits the unique properties of MI-field to determine the locations of the randomly deployed FracBot nodes in oil reservoirs. Third, we developed an accurate energy framework of a linear FracBot network topology that generates feasible nodes transmission rates and network topology while always guaranteeing sufficient energy. Then, we designed, developed, and fabricated MI-based FracBot nodes. Finally, to validate the performance of our solutions in our produced prototype of FracBot nodes, we developed a physical MI-based WUSN testbed.

The contributions in each chapter are summarized as follows:

7.1 MI-Based Environment-Aware Cross-layer Communication Protocol Design for WUSN in Hydraulic Fractures and Oil Reservoirs

In this chapter, we developed the distributed environment-aware protocol (DEAP), a fully distributed cross-layer protocol framework for MI-based WUSNs. Satisfying the QoS requirements of diverse applications it achieves optimal energy consumption and high throughput efficiency with low computational complexity. We address the interaction of key underground communication functionalities and a distributed cross-layer design and ensure that DEAP efficiently utilizes the bandwidth-limited MI channels in WUSNs. Its designated distributed power control enables the DS-CDMA mechanism via chaotic codes for reliable link transmissions with limited available network information. In addition, it guarantees statistical delay constraints and achieves optimal link throughput by solving the framework with respect to the given code length. Building on these results, we employ a two-phase decision strategy to sequentially tackle two sub-problems for optimal feasible energy savings and throughput gain with low computation complexity for great practicability. A performance evaluation confirms that the DEAP provides high system throughput and very low energy consumption within a guaranteed delay. Simulation results also confirm its remarkable energy savings and high throughput gain in a distributed manner, favored by practical implementation in WUSNs, and that it outperforms layered protocol solutions by 50% in energy savings and 6 dB in throughput gain.

These outstanding energy and spectral efficiencies accompanied with low computational complexity confirm that the proposed DEAP strongly suits underground environments. Therefore, we introduce a new paradigm for reliable and efficient MI communication and offer a novel avenue towards distributed cross-layer design in WUSNs.

7.2 MI-Based Localization for WUSN in Hydraulic Fractures and Oil Reservoirs

In this chapter, we developed a novel MI-based localization algorithm that takes advantage of the promising features of the MI channel. Our solution jointly applies WMLE (weighted maximum likelihood estimation), SDP (semi-definite programming) relaxation, ADM (alternating direction augmented Lagrangian method), and CGA (conjugate gradient algorithm) with regards to the MI-based communication channel to achieve high positioning accuracy of wireless sensor devices (FracBots) in oil reservoirs while maintaining high computational efficiency. The fundamental challenge for localization in randomly-deployed WUSNs is addressed by exploiting RMFS measurements from MI-based communication and fast, accurate successive positioning algorithms. Leveraging the multi-path and fading free nature of MI-based communication, RMFS from AWGN channel modeling serves as location-dependent information for the localization algorithm designs. Moreover, the fast ADM provides useful initial positioning within a few iterations, and the powerful CGA refines the initial results into highly accurate sensor positions. A performance evaluation confirmed that the proposed localization algorithm by guaranteeing considerable positioning accuracy with great time-efficiency in underground environments, represents a novel paradigm for sensor localization in randomly-deployed WUSNs.

7.3 Optimal Energy Planning for Self-Contained WUSN in Hydraulic Fractures and Oil Reservoirs

In this chapter, we proposed an optimal energy planning approach of a linear oil sensor network topology that ensures an accurate energy model that provides optimal sensor transmission rates and optimal sensor network planning. We show how the inhomogeneous environment strongly affects the downlink and uplink channels inside oil reservoirs. Since magnetic induction communication channels are employed, we

examine the non-flat fading nature of MI communications to obtain accurate received signal quality for reliable MI communications inside oil reservoirs. Then, we design MI-based modulation and error control coding schemes and evaluate the energy consumption for MI transmissions to determine an optimal sensor transmission rate and number of sensors while satisfying the sensor PER and energy constraints. We also evaluate modulation and error control coding for transmitting data between nodes. We obtain the optimal total transmissions rate of the entire network and number of sensors while satisfing the PER and energy constraints of sensors. We confirm the accuracy of our model via theoretical and simulation evaluations.

7.4 MI-based FracBot Node Design for Monitoring Hydraulic Fractures and Oil Reservoirs

In this chapter, we proposed a novel prototypes of MI-based wireless FracBots for potential use as a platform for a new generation of WUSNs for monitoring hydraulic fractures and unconventional reservoirs, and measuring other wellbore parameters. We designed and developed the hardware of the MI-based wireless FracBots for short-range communication using near-field communication (NFC) as a physical layer combined with an energy-harvesting capability and ultra-low power requirements. We were able to realize these characteristics using cost-effective and commercial off-the-shelf components. We outlined the design requirements and implementation processes of the FracBot node platform and designed two types of FracBot nodes: a FracBot active node and a FracBot passive node. We designed seven types of antennas used in the implementation and experimental processes and described the main characteristics of the FracBot antenna, including the NFC antenna equivalent circuit and the resonance frequency of the transmitter and receiver antennas. This design, which will operate in hydraulic fractures and oil reservoirs, is the first of its kind. Such nodes, however, are not yet commercially available, for they need to be designed to overcome limitations caused by the small size requirement and harsh underground

environments. Accordingly, we designed the FracBot node as a platform for a new generation of WUSNs that can serve variety of purposes, provide flexibility, and allow for experimentation. This design is very specialized in terms of its communication layer, size, and energy source to overcome limitations caused by harsh environmental conditions and energy constraints. Under this conditions, the node is able to collect data from subsurface area, hydraulic fractures, and water/gas/oil reservoirs in real time. To realize this design, the steps of which are outlined in the fabrication process, we had to satisfy the restrictive design characteristics of the node: a long operation time, ultra-low power, an efficient communication layer, and an energy-harvesting capability.

7.5 FracBot Testbed: Performance Evaluation

In this chapter,we presented an evaluation of the FracBot node and the NFC/MI antenna in air, sand, and stone media. One of the main results is that the mismatch between TX and RX antennas increases as a result of the effects of sand or stone media. Thus, to overcome a mismatch resulting from an inhomogeneous environment, the adaptive-frequency feature or advance matching circuit design shall be incorporated into the optimized design of the FracBot. This feature will allow optimal energy transfer and a reliable communication link through sand and stone media. The FracBot features a very efficient energy-harvesting circuit that is capable of collecting 16 mW of energy under continuous radiated power while the actual energy consumption of the node is 34.4 μW and shows the FracBot can operate perpetually with minimal energy-radiated conditions. Also, the FracBot can establish at communication link and transmit data using modulation ASK with a data rate of 1.6 kbit/s. The minimum receiver sensitivity of the current MI system must be -70 dBm, based on experimental measurements. Sand and stone media affect the performance of NFC antennas, which eventually degrade MI signal propagation and reduce

energy transfer. Since the design of our FracBot entails the use of cost-effective and commercial off-the-shelf components, we experience a number of restrictions in the design and analysis. For example, the NFC chip does not allow the configuration of the data rate and sensitivities that prevent us from conducting extensive analysis on the communication functionality of the FracBot. Hardware development should lead to a better understanding of the environmental challenges, improve the electronic sensitivity and optimize the minimal resources necessary to miniaturize the FracBot hardware. These experiments and testbed analysis help us determine the requirements for design of an optimal MI system that operates in ultra-low energy requirements.

REFERENCES

[1] S. W. Tinker, "The Role of Unconventional Gas in the Global Energy Future," Global Climate and Energy Project (GCEP) Seminar, Nov. 19, 2009, Stanford University.

[2] D. Chapman and W. Trybula, "Meeting the challenges of oilfield exploration using intelligent micro and nano-scale sensors," in Proc. 2012 IEEE International Conference on Nanotechnology.

[3] W. C. Lyons and G. J. Plisga, "Standard Handbook of Petroleum and Natural Gas Engineering." Gulf Professional Pub., 2005.

[4] D. L. Gysling and F. X. T. Bostick, "Changing paradigms in oil and gas reservoir monitoring: the introduction and commercialization of in-well optical sensing systems," in Proc. 2002 Optical Fiber Sensors Conference Technical Digest, vol. 1, pp. 43-46.

[5] O. Duru and R. N. Horne, "Modeling reservoir temperature transients, and matching to permanent downhole gauge (PDG) data for reservoir parameter estimation," in Proc. 2008 SPE Annual Technical Conference and Exhibition.

[6] S. S. Mani, B. G. van Bloemen Waanders, S. P. Cooper, B. E. Jakaboski, R. A. Normann, J. Jennings, B. Gilbert, L. W. Lake, C. J. Weiss, J. C. Lorenz et al., "Analysis of real-time reservoir monitoring: reservoirs, strategies and modeling." Sandia National Laboratories, Tech. Rep., 2006.

[7] PTRC-INCAS^3 Innovation Centre "Micro sensor motes successfully travel through a canadian heavy oil reservoir." Available: http://www.incas3.eu/news

[8] Z. Sun and I. F. Akyildiz, "Magnetic induction communications for wireless underground sensor networks," IEEE Trans. Antennas Propag., vol. 58, no. 7, pp. 2426-2435, July 2010.

[9] A. K. RamRakhyani, S. Mirabbasi, and M. Chiao, "Design and optimization of resonance-based efficient wireless power delivery systems for biomedical implants," IEEE Trans. Biomed. Circuits Syst., vol. 5, no. 1, pp. 48-63, Feb. 2011.

[10] A. A. Alshehri, I. F. Akyildiz and J. M. Servin, H. K. Schmidt, "FracBot Technology for Mapping Hydraulic Fractures," ATCE 2017 (the Annual Technical Conference and Exhibition), San Antonio, Texas, USA, October 2017.

[11] [6] N. R. Warpinski, "Hydraulic Fracture Diagnostics," J. Pet. Tech., Oct. 1996, p 907.

[12] [7] R. D. Barree, M. K. Fisher and R. A. Woodroof, "A Practical Guide to Hydrualic Fracture Diagnostic Technologies," SPE Annual Technical Conference and Exhibition, 29 Sep. 2002, SPE 77442.

[13] Akyildiz, Ian F., and Mehmet Can Vuran. Wireless sensor networks. Vol. 4. John Wiley and Sons, 2010.

[14] S. Kisseleff, I. F. Akyildiz, and W. Gerstacker, "Throughput of the magnetic induction based wireless underground sensor networks: Key optimization techniques," IEEE Trans. Commun., vol. 62, no. 12, pp. 4426-4439, Dec 2014.

[15] J. I. Agbinya, "Investigation of near field inductive communication system models, channels and experiments," Progress In Electromagnetics Research B, vol. 49, pp. 129-153, 2013.

[16] Z. Sun and I. F. Akyildiz, "Optimal deployment for magnetic induction based wireless networks in challenged environments," IEEE Trans. Wireless Commun., vol. 12, no. 3, pp. 996-1005, Mar. 2013.

[17] J. I. Agbinya, "A magneto-inductive link budget for wireless power transfer and inductive communication systems," Progress In Electromagnetics Research C, vol. 37, pp. 15-28, 2013.

[18] A. Karalis, J. D. Joannopoulos, and M. Soljacic, "Efficient wireless nonradiative mid-range energy transfer," Annals of Physics (Elsevier), vol. 323, no. 1, pp. 34-48, Jan. 2008.

[19] A A. Alshehri, I. F. Akyildiz, S.-C. Lin. and H. K Schmidt, "Environment-Aware Cross-layer Communication Protocol Design in Underground Oil Reservoirs," under review by USPTO, December 2016.

[20] X. Lin, N. B. Shroff, and R. Srikant, "A tutorial on cross-layer optimization in wireless networks," IEEE J. Sel. Areas Commun., vol. 24, no. 8, pp. 1452-1463, Aug. 2006.

[21] S. De, C. Qiao, D. A. Pados, M. Chatterjee, and S. J. Philip, "An integrated cross-layer study of wireless CDMA sensor networks," IEEE J. Sel. Areas Commun., vol. 22, no. 7, pp. 1271-1285, 2004.

[22] S. Cui, R. Madan, A. J. Goldsmith, and S. Lall, "Cross-layer energy and delay optimization in small-scale sensor networks," IEEE Trans. Wireless Commun., vol. 6, no. 10, pp. 3688-3699, Oct. 2007.

[23] M. C. Vuran and I. F. Akyildiz, "XLP: A cross-layer protocol for efficient communication in wireless sensor networks," IEEE Trans. Mobile Comput., vol. 9, no. 11, pp. 1578-1591, Nov. 2010.

[24] D. Pompili and I. F. Akyildiz, "A multimedia cross-layer protocol for underwater acoustic sensor networks," IEEE Trans. Wireless Commun., vol. 9, no. 9, pp. 2924-2933, 2010.

[25] Sun, Zhi, and Ian F. Akyildiz. "Magnetic induction communications for wireless underground sensor networks." IEEE Transactions on Antennas and Propagation 58.7 (2010): 2426-2435.

[26] Gulbahar, Burhan, and Ozgur B. Akan. "A communication theoretical modeling and analysis of underwater magneto-inductive wireless channels." IEEE Transactions on Wireless Communications 11.9 (2012): 3326-3334.

[27] Masihpour, Mehrnoush, M. Abolhasan, and D. R. Franklin. "Multihop relay techniques for communication range extension in near-field magnetic induction communication systems." Journal of Networks (2013).

[28] Vuran, M. Can, and Agnelo R. Silva. "Communication through soil in wireless underground sensor networks: theory and practice." In Sensor Networks, pp. 309-347. Springer Berlin Heidelberg, 2010.

[29] Li et al. "Self-adaptive modulation method and system for wireless underground sensor network (WUSN)," Publication number CN103701567 A, April 2014.

[30] S.-C. Lin, I. F. Akyildiz, P. Wang, and Z. Sun, "Distributed crosslayer protocol design for magnetic induction communication in wireless underground sensor networks," IEEE Trans. Wireless Commun., vol. 14, no. 7, pp. 4006-4019, Jul. 2015.

[31] D. R. Frank, Electromagnetic Theory. Englewood Cliffs, NJ, USA: Prentice-Hall, 1986.

[32] S. Kisseleff,W. Gerstacker, R. Schober, Z. Sun, and I. F. Akyildiz, "Channel capacity of magnetic induction based wireless underground sensor networks under practical constraints," in Proc. IEEE WCNC, Apr. 2013, pp. 2603-2608.

[33] Y. Sankarasubramaniam, I. F. Akyildiz, and S. W. McLaughlin, "Energy efficiency based packet size optimization in wireless sensor networks," in Proc. IEEE SNPA, Apr. 2003, pp. 1-8.

[34] Campbell Scientific, Logan, UT, USA, Soil temperature sensors. [Online]. Available: http://www.campbellsci.com

[35] G. Mazzini, G. Setti, and R. Rovatti, "Chaotic complex spreading sequences for asynchronous DS-CDMA. i. system modeling and results," IEEE Trans. Circuits Syst. I, Fundam. Theory Appl., vol. 44, no. 10, pp. 937-947, Oct. 1997.

[36] C. S. Chang and K. C. Chen, "Medium access protocol design for delay-guaranteed multicode CDMA multimedia networks," IEEE Trans. Wireless Commun., vol. 2, no. 6, pp. 1159-1167, Nov. 2003.

[37] D. Pompili, T. Melodia, and I. F. Akyildiz, "Routing algorithms for delay-insensitive and delay-sensitive applications in underwater sensor networks," in Proc. ACM Conf. MobiCom Netw., 2006, pp. 298-309.

[38] H. Zhang and H. Shen, "Energy-efficient beaconless geographic routing in wireless sensor networks," IEEE Trans. Parallel Distrib. Syst., vol. 21, no. 6, pp. 881-896, Jun. 2010.

[39] A. Magnani and K. K. Leung, "Self-organized, scalable GPS-free localization of wireless sensors," in Proc. IEEE WCNC, Mar. 2007, pp. 3798-3803.

[40] D. Bertsekas and R. Gallager, Data Networks. Englewood Cliffs, NJ, USA: Prentice-Hall, 1987.

[41] Chong, Edwin KP, and Stanislaw H. Zak. "An introduction to optimization." Vol. 76. John Wiley and Sons, 2013.

[42] A A. Alshehri, I. F. Akyildiz, S.-C. Lin. and H. K Schmidt, "Magnetic Induction (MI)-Based Localization for Wireless Sensor Networks in Underground Oil Reservoirs," under review by USPTO, March 2017.

[43] Lin, Shih-Chun, Abdallah Awadh Alshehri, Pu Wang, and Ian F. Akyildiz. "Magnetic Induction-Based Localization in Randomly Deployed Wireless Underground Sensor Networks." IEEE Internet of Things Journal 4, no. 5 (2017): 1454-1465.

[44] Niewiadomska-Szynkiewicz, Ewa. "Localization in wireless sensor networks: Classification and evaluation of techniques." International Journal of Applied Mathematics and Computer Science 22.2 (2012): 281-297.

[45] Costa, Jose A., Neal Patwari, and Alfred O. Hero III. "Distributed weighted-multidimensional scaling for node localization in sensor networks." ACM Transactions on Sensor Networks (TOSN) 2.1 (2006): 39-64.

[46] Li, Xinrong. "Collaborative localization with received-signal strength in wireless sensor networks." IEEE Transactions on Vehicular Technology 56.6 (2007): 3807-3817.

[47] Kannan, Anushiya A., Baris Fidan, and Guoqiang Mao. "Analysis of flip ambiguities for robust sensor network localization." IEEE transactions on vehicular technology 59.4 (2010): 2057-2070.

[48] Soares, Cludia, Joo Xavier, and Joo Gomes. "Simple and fast convex relaxation method for cooperative localization in sensor networks using range measurements." IEEE Transactions on Signal Processing 63.17 (2015): 4532-4543.

[49] P. Biswas, T. Liang, K. Toh, T. Wang, and Y. Ye, "Semidefinite programming approaches for sensor network localization with noisy distance measurements," IEEE Trans. on Automation Science and Engineering, 2006.

[50] Nie, Jiawang. "Sum of squares method for sensor network localization." Computational Optimization and Applications 43.2 (2009): 151-179.

[51] Ji, Senshan, et al. "Beyond convex relaxation: A polynomial-time non-convex optimization approach to network localization." INFOCOM, 2013 Proceedings IEEE. IEEE, 2013.

[52] Simonetto, Andrea, and Geert Leus. "Distributed Maximum Likelihood Sensor Network Localization." IEEE Trans. Signal Processing 62.6 (2014): 1424-1437.

[53] S. Boyd and L. Vandenberghe, Convex Optimization. Cambridge Univ. Press, 2004.

[54] Z. Wen, D. Goldfarb, and W. Yin, "Alternating direction augmented lagrangian methods for semidefinite programming," Mathematical Programming Computation, vol. 2, no. 3-4, pp. 203-230, 2010.

[55] S. Boyd, N. Parikh, E. Chu, B. Peleato, and J. Eckstein, "Distributed optimization and statistical learning via the alternating direction method of multipliers," Found. Trends Mach. Learn., vol. 3, no. 1, pp. 1-122, 2011.

[56] J. Nocedal and S. J. Wright, Numerical Optimization. Springer Series in Operations Research. New York: Springer-Verlag, 1999.

[57] Alshehri, A. A., Lin, S.-C., and Akyildiz, I. F., "Optimal Energy Planning for Wireless Self-Contained Sensor Networks in Oil Reservoirs," to be appeared in Proc. IEEE ICC 2017, Paris, France, May 2017.

[58] Varshney, Lav R. "Transporting information and energy simultaneously." Information Theory, 2008. ISIT 2008. IEEE International Symposium on. IEEE, 2008.

[59] Grover, Pulkit, and Anant Sahai. "Shannon meets Tesla: Wireless information and power transfer." Information Theory Proceedings (ISIT), 2010 IEEE International Symposium on. IEEE, 2010.

[60] De, Swades, and Riya Singhal. "Toward uninterrupted operation of wireless sensor networks." Computer 45.9 (2012): 24-30.

[61] H. Guo and Z. Sun, "Channel and energy modeling for self-contained wireless sensor networks in oil reservoirs," IEEE Transactions on Wireless Communications, vol. 13, no. 4, pp. 2258-2269, 2014.

[62] Martins, C. H. N., Alshehri, A. A., and Akyildiz, I. F.,"Novel MI-based (FracBot) Sensor Hardware Design for Monitoring Hydraulic Fractures and Oil Reservoirs," 2017 IEEE 8th Annual Ubiquitous Computing, Electronics and Mobile Communication Conference, Oct. 2017.

[63] N. R. Warpinski et al., "Hydraulic fracture diagnostics," Journal of Petroleum Technology, vol. 48, no. 10, pp. 907-910, 1996.

[64] R. Barree, M. Fisher, and R. Woodroof, "A practical guide to hydraulic fracture diagnostic technologies: Paper spe 77442," in SPE Annual Technical Conference and Exhibition held in San Antonio, Texas, vol. 29, 2002.

[65] M. A. Akkas, I. F. Akyildiz, and R. Sokullu, "Terahertz channel modeling of underground sensor networks in oil reservoirs," in Global Communications Conference (GLOBECOM), 2012 IEEE. IEEE, 2012, pp. 543-548.

[66] Coskun, Vedat, Busra Ozdenizci, and Kerem Ok. "A survey on near field communication (NFC) technology." Wireless personal communications 71, no. 3 (2013): 2259-2294.

[67] Jing, Hengzhen Crystal, and Yuanxun Ethan Wang. "Capacity performance of an inductively coupled near field communication system." In Antennas and Propagation Society International Symposium, 2008. AP-S 2008. IEEE, pp. 1-4. IEEE, 2008.

[68] Strommer, Esko, Jouni Kaartinen, Juha Parkka, Arto Ylisaukko-oja, and Ilkka Korhonen. "Application of near field communication for health monitoring in daily life." In Engineering in Medicine and Biology Society, 2006. EMBS'06. 28th Annual International Conference of the IEEE, pp. 3246-3249. IEEE, 2006.

[69] Bieler, Thierry, Marc Perrottet, Valrie Nguyen, and Yves Perriard. "Contactless power and information transmission." IEEE Transactions on Industry Applications 38, no. 5 (2002): 1266-1272.

[70] Domingo, Mari Carmen. "Magnetic induction for underwater wireless communication networks." IEEE Transactions on Antennas and Propagation 60, no. 6 (2012): 2929-2939.

[71] Schantz, Hans Gregory. "Near field propagation law a novel fundamental limit to antenna gain versus size." In Antennas and Propagation Society International Symposium, 2005 IEEE, vol. 3, pp. 237-240. IEEE, 2005.

[72] Agbinya, Johnson Ihyeh. "A magneto-inductive link budget for wireless power transfer and inductive communication systems." Progress In Electromagnetics Research 37 (2013): 15-28.

[73] Azad, Umar, Hengzhen Crystal Jing, and Yuanxun Ethan Wang. "Link budget and capacity performance of inductively coupled resonant loops." IEEE transactions on antennas and propagation 60, no. 5 (2012): 2453-2461.

[74] M. F. U. Guide, "Mixed signal microcontroller," 2012.

[75] (2016) Ultra-low power with msp430. [Online]. Available: http://embeddedcomputing.weebly. com/ultra-low-power-with-msp430.html

[76] (2016) Ft230x usb to basicc uart ic (ft 00566). [Online]. Available: http://www.ftdichip.com/ Support/Documents/DataSheets/ICs/DS FT230X.pdf

[77] S. Electronics. (2016) Dynamic nfc/rfid tag ic with 64-kbit eeprom, energy harvesting, ic bus and iso 15693 rf interface. [Online]. Available: http://www.st.com/content/ccc/resource/technical/document/datasheet/ 45/6b/a2/02/63/ad/45/43/DM00047008.pdf/files/DM00047008.pdf/jcr: content/translations/en.DM00047008.pdf

[78] (2015) Understanding the i2c bus (slva704). [Online]. Available: http://www.ti.com/lit/an/ slva704/slva704.pdf

[79] (2013) Using the msp430 launchpad as a standalone i2c host for audio products (slaa605a). [Online]. Available: http://www.ti.com/lit/an/slaa605a/slaa605a.pdf

[80] (2016) Dynamic nfc/rfid tag ic with 64-kbit eeprom, energy harvesting, ic bus and iso 15693 rf interface (dm00047008). [Online]. Available: http://www.st.com/content/ccc/resource/technical/document/ datasheet/45/6b/a2/02/63/ad/45/43/DM00047008.pdf/

les/DM00047008.pdf/jcr:content/translations/en.DM00047008.pdf

[81] (2015) Um1589 m24lr-discovery kit user guide (dm00068980). [Online]. Available: http://www.st.com/content/ccc/resource/technical/document/user manual/f8/f5/c2/20/b5/ 55/42/26/DM00068980.pdf/

les/DM00068980.pdf/jcr:content/translations/en.DM00068980.pdf

[82] (2015) bq25570 nano power boost charger and buck converter for energy harvester powered applications (slusbh2e). [Online]. Available: http://www.ti.com/lit/ds/symlink/bq25570.pdf

[83] (2016) Supercapacitor eecs5r5h155: Sg. [Online]. Available: http:industrial.panasonic.com/ww/products/capacitors/edlc/edlc-coin-type/sg/EECS5R5H155

[84] (2015) Polymer li-ion rechargeable battery 3.7v 110ma. [Online]. Available: http: //cdn.sparkfun.com/datasheets/Prototyping/spe-00-DTP401525-110mah-en-1.0ver.pdf

[85] (2015) Tmp102 low-power digital temperature sensor with smbus and two-wire serial interface in sot563 (sbos397f). [Online]. Available: http://www.ti.com/lit/ds/symlink/tmp102.pdf

[86] (2014) Trf7970a multiprotocol fully integrated 13.56-mhz and near

field communication (nfc) transceiver ic (slos743k). [Online]. Available: http:www.ti.com/lit/ds/symlink/trf7970a.pdf

[87] (2011) Tmp102evm evaluation board and software tutorial (sbou114). [Online]. Available: http://www.ti.com/lit/ug/sbou114/sbou114.pdf

[88] A 13.56 MHz customized antenna for ST25 NFC / RFID Tags. [online] application note an2866.

[89] (2003) Antenna circuit design for rd applications (ds00710c). [Online]. Available: http://ww1.microchip.com/downloads/en/AppNotes/00710c.pdf

VITA

Abdallah Awadh Alshehri received the B.S. degree in electrical engineering from King Fahd University of Petroleum and Minerals (KFUPM), Saudi Arabia in 2002 and the M.S. degree in communication engineering from Concordia University, Canada in 2008. He received the Ph.D. degree from the School of Electrical and Computer Engineering of Georgia Institute of Technology, Atlanta, GA, USA in May 2018. He was a research assistant in the Broadband and Wireless Networking Laboratory (BWN-LAB) from January 2014 to May 2018, under the supervision of Professor Ian F. Akyildiz. He joined Saudi Aramco Oil Company in 2002 and is holding a research engineer position at it until now. He received the Best-in-Class Young Researcher award from Saudi Aramco Oil Company in 2017. He received the best paper award at the IEEE UEMCON 2017. He is a member of the IEEE and SPE. His research interests include wireless underground sensor networks, in-suite sensing methodologies and applications for monitoring oil and gas reservoir.